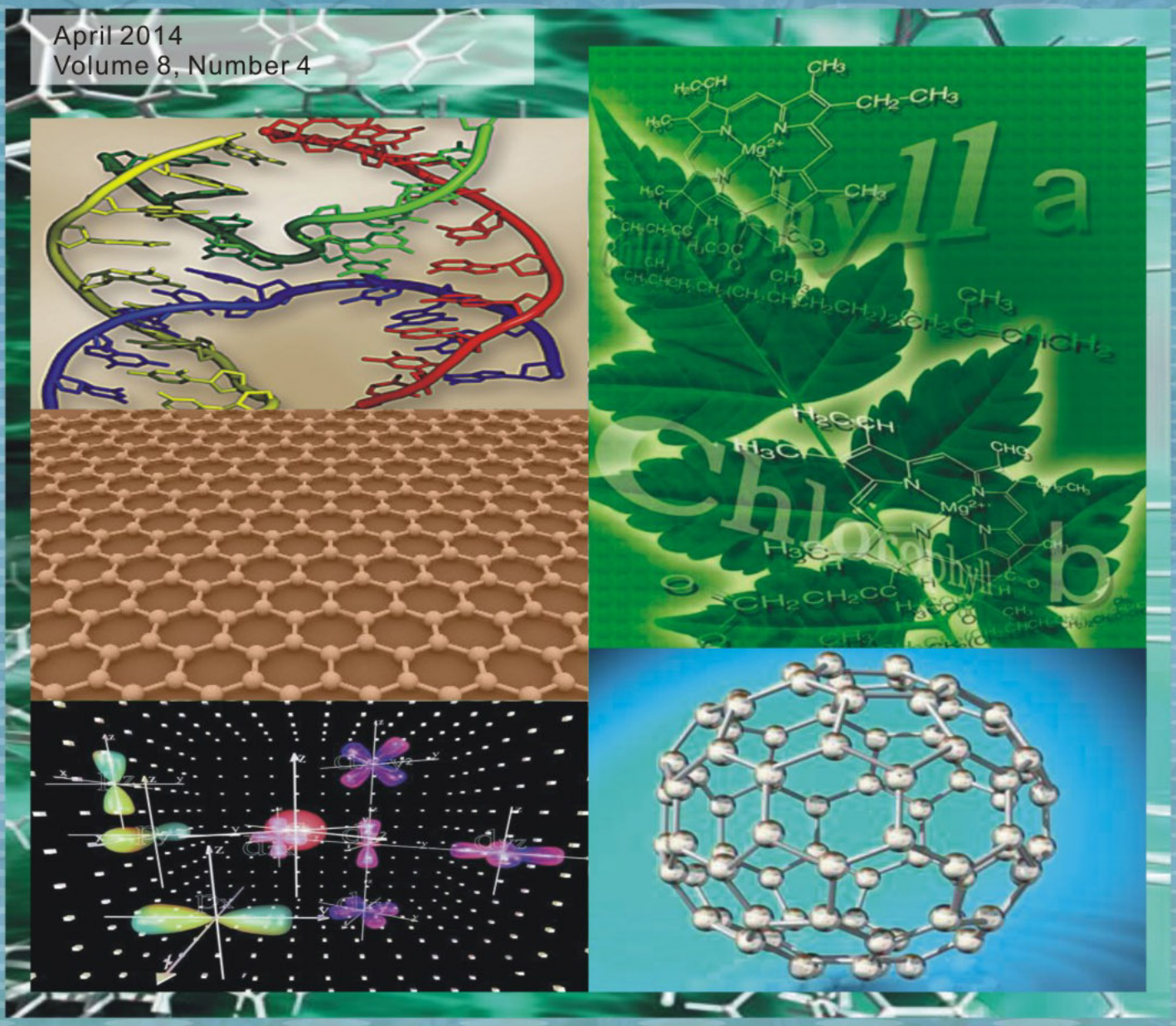
From Knowledge to Wisdom

JCCE

ISSN 1934-7375 (Print)
ISSN 1934-7383 (Online)

Journal of Chemistry and Chemical Engineering

April 2014
Volume 8, Number 4



David Publishing Company
www.davidpublishing.com

Journal of Chemistry and Chemical Engineering

Volume 8, Number 4, April 2014 (Serial Number 77)

David Publishing Company
www.davidpublishing.com

Publication Information:
Journal of Chemistry and Chemical Engineering is published monthly in hard copy (ISSN 1934-7375) and online (ISSN 1934-7383) by David Publishing Company located at 240 Nagle Avenue #15C, New York, NY 10034, USA.

Aims and Scope:
Journal of Chemistry and Chemical Engineering, a monthly professional academic journal, particularly emphasizes new research results in realm of chemistry and chemical engineering. Articles interpreting practical application of up-to-date science and technology are also welcome.

Editorial Board Members:

Professor, Ali Asghar Hosseini, University of Mazandaran, Iran;
Professor, Teodoro Saul Kaufman, Instituto de Química Rosario, Argentina;
Professor, P. Selvarajan, Aditanar College of Arts and Science, India;
Professor, Michael Kaplan, Simmons College (Boston), USA.

Manuscripts and correspondence are invited for publication. You can submit your papers via web submission, or E-mail to chemistry@davidpublishing.com or chemistry@davidpublishing.org. Submission guidelines and web submission system are available at http://www.davidpublishing.com, http://www.davidpublishing.org.

Editorial Office:
240 Nagle Avenue #15C, New York, NY 10034, USA
Tel: 1-323-984-7526, 323-410-1082
Fax: 1-323-984-7374, 323-908-0457
E-mail: chemistry@davidpublishing.com; chemistry@davidpublishing.org

Copyright©2014 by David Publishing Company and individual contributors. All rights reserved. David Publishing Company holds the exclusive copyright of all the contents of this journal. In accordance with the international convention, no part of this journal may be reproduced or transmitted by any media or publishing organs (including various websites) without the written permission of the copyright holder. Otherwise, any conduct would be considered as the violation of the copyright. The contents of this journal are available for any citation. However, all the citations should be clearly indicated with the title of this journal, serial number and the name of the author.

Subscription Information:
Price ($/year):
Print $480, Online $320, Print and Online $600

David Publishing Company
240 Nagle Avenue #15C, New York, NY 10034, USA
Tel: 1-323-984-7526, 323-410-1082; Fax: 1-323-984-7374, 323-908-0457
E-mail: order@davidpublishing.com
Digital Cooperative Company: www.bookan.com.cn



David Publishing Company
www.davidpublishing.com

Journal of Chemistry and Chemical Engineering

Volume 8, Number 4, April 2014 (Serial Number 77)

Contents

Analytical Chemistry

331 **Periodic Precipitation of Liesegang System under Microwave Radiation**

Yushin Kanazawa and Yusuke Asakuma

335 **Calf Thymus DNA Intercalation by Anionic Ru(III) Complexes Containing Tridentate Schiff Bases Derived from 5-X-Substituted Salicyladehyde and 2-Aminophenol**

Emira Kahrovic, Adnan Zahirovic and Emir Turkusic

344 **The Determination of Average Stability Constant of Nickel-Fulvic Acids Complex at pH = 8.0 by the Solubility Method**

Giorgi Makharadze, Nazi Goliadze, Tamar Makharadze and Guram Supatashvili

Materials Chemistry

349 **Microwave Preparation of SiO_2-B_2O_3-Na_2O-K_2O-CaO-Fe_2O_3-TiO_2 Glass System**

Ashis Kumar Mandal, Prasanta Kumar Sinha, Santanu Sen, Sitendu Mondal, Chandan Guha and Ranjan Sen

358 **Electrochemical Behavior of Electrodeposited Sn Films: Possible Negative Electrode for Na^+ Rechargeable Batteries**

Reza Fathi, Riccardo Ruffo and Claudio Maria Mari

364 **LA-ICP MS Characteristic of Geochemical Composition of Veins Rocks from the Central Part of the Khibina Massive in Kola Peninsula, Northern Russia**

Miłosz Huber

371 **Obtaining Porosity of Concrete Using X-ray Microtomography or Digital Scanner**

Jose Renato de Castro Pessoa, Joel Sanchez Dominguez, Gil de Carvalho and Joaquim Teixeira de Assis

378 **Nano Fibrous Cerium(IV) Hydrogen Phosphate Membrane Self Supported Indole Polymerization Agent**

Sadek Khalifa Shakshooki

385 **Synthesis and Study of Heteronuclear Citrates**

Nani Bidzina Zhorzholiani, Iamze Alim Beshkenadze, Maia Avtandil Gogaladze and Givi Tengiz Begheluri

Biological Chemistry

390 **Influence of Technological Operations in the Dissolved Oxygen Content of Wines**

Ana Catarino1, Sandra Alves and Helena Mira

395 **Purification of Bromelain Enzyme from Curauá (*Ananaserectifolius LB Smith*) White Variety, by Aqueous Two-Phase System PEG 4000/Potassium Phosphate**

Juliana Ferrari Ferreira, Dalva Sbruzzi, Kleber Vânio Gomes Barros, Daniela Diniz Ehrhardt and Elias Basile Tambourgi

Environmental Chemistry

400 **Microbiological Treatment of Effluent for Zinc Hydrometallurgical Plant**

Ashish Kumar, Krishna Deo Sharma and Sunil Duggal

Chemical Engineering

408 **Influence of Pressure and Temperature on the Velocity of a Turbulent Jet Flow 3D**

Flávia Aparecida Reitz Cardoso, Regiani Aparecida de Almeida, Ricardo Vicente de Paula Rezende, Lúcio Cardozo-Filho, Dirceu Noriler, Henry França Meier and Vladimir Ferreira Cabral

Physical Chemistry

417 **Polymer-Based Micro Flow Sensor with Alternative Electronic Signal Interfaces for Low and High Flow Rates**

Thomas Schönstein

421 **The Sensitivity of TE Filed Propagating in LHM-Antiferromagnetic Sensor**

Zeyad I. Al-Sahhar, Hala J. El-Khozondar and Mohamad M. Shabat

428 **Search for New Three-, Four-Component Petasis, Passerini, Hantzsch, Kabachnic-Fields, Ugi Reactions with Organic Compounds of Phosphorus, Arsenic, Antimony and Bismuth**

Aibassov Erkin Zhakenovich, Yemelyanova Valentina Stepanovna, Shakieva Tatyana Vladimirovna, Tussupbaev Nessipbay Kuandykovich and Blagikh Evgeniy Vladimirovich

J. Chem. Chem. Eng. 8 (2014) 331-334

Periodic Precipitation of Liesegang System under Microwave Radiation

Yushin Kanazawa and Yusuke Asakuma*

Department of Mechanical and System Engineering, University of Hyogo, Himeji 671-2280, Japan

Received: February 27, 2014 / Accepted: March 15, 2014 / Published: April 25, 2014.

Abstract: We studied precipitation patterns in a Liesegang system under MW (microwave) irradiation in order to investigate metal salt diffusion in an electrolyte gel. The gel and salt concentrations were varied. MW irradiation induced periodic patterns of precipitation because polar molecules vibrate and rotate in an electromagnetic field. For example, the number of patterns increased by the irradiation. Accordingly, microwave irradiation nonlinearly accelerated the diffusion of ionic molecules.

Key words: MW, Liesegang, diffusion, precipitation.

1. Introduction

Liesegang phenomena, a function of diffusion and reaction conditions, form attractive and unique periodic stripe patterns. Such pattern formation frequently inspires microstructural design in materials science. Moreover, morphological pattern transitions between periodic precipitation and tree-like crystal aggregates are scientifically interesting [1, 2]. Liesegang phenomena usually manifest themselves when a concentrated salt solution diffuses through a gel that contains another electrolyte at a lower concentration. Diffusion and chemical reactions cause little precipitation of otherwise soluble salts in a periodic manner. The precipitation and redissolution reactions for a generic metal ion M^{2+} are as follows:

$$M^{2+}\,(aq) + 2NH_4OH\,(aq) \rightarrow 2NH_4^{+}\,(aq) + M(OH)_2(s) \quad (1)$$

$$M(OH)_2\,(s) + 6NH_4^{+}\,(aq) \rightarrow M(NH_3)_6^{2+}\,(aq) + 2H_2O\,(l) + 4H^{+}\,(aq) \quad (2)$$

When NH_4OH diffusion causes metal ions to precipitate in the form of $M(OH)_2$, redissolution at the top of the pattern induces a Liesegang band.

Recent research indicates that spontaneous diffusion-related self-organization dynamics and irreversible reactions or precipitation systems based on Ostwald supersaturation theory explain Liesegang pattern formation [3]. However, nonlinearity hinders elaboration of the exact mechanism.

MW (microwave) radiation may be helpful in this context. MW radiation has recently been a very active area of research due to the many advantages of nonthermal effects such as reaction promotion, nucleation induction, and diffusion facilitated by the molecular vibration of polar molecules [4, 5]. We hypothesized that the reaction and diffusion characteristics of a Liesegang system could be modulated or explained via various MW properties. In addition, Liesegang phenomena may suggest a new application of MW radiation and suitable operating conditions for highly functional inorganic nanomaterials. Salt and gel concentration are essential for solving the diffusion challenge of Liesegang phenomena. In this study, we varied gel and salt concentrations to understand the MW effect. We used a MW reactor equipped with an in situ observation system to analyze the dynamic growth behavior of the periodic pattern.

*Corresponding author: Yusuke Asakuma, Associate Professor, research fields: heat and mass transfer, microwave. E-mail: asakuma@eng.u-hyogo.ac.jp.

2. Experiments

To form a Liesegang pattern, we used a gel because it can prevent precipitate sedimentation and hydrodynamic turbulence. A salt was added to a prepared gelatin-based gel [6, 7]. In this study, gelatin and salt concentrations, C_g, C_c were varied, and we used $Co(NO_3)_2$ (Table 1). We first heated a solution (i.e., gel and salt) to 90 °C. We then poured the solution into a glass test tube (Φ: 13 mm; height: 100 mm; volume: 5 mL) and gradually cooled it to room temperature to impart a homogeneous gelatin network structure. Temperature is the most important factor for pattern formation; we used two different methods, MW irradiation and conventional heating (OB, oil bath) for maintaining solution temperature. After we poured 2 mL of a 28% ammonium solution at the gel surface, we covered it with a silicon rubber lid. Ammonium salt precipitates via ammonium ion diffusion into the gel, and Liesegang stripe-pattern formation starts from the top surface to the bottom of the tube. We measured the stripe number and length for the two heating methods.

2.1 MW Heating

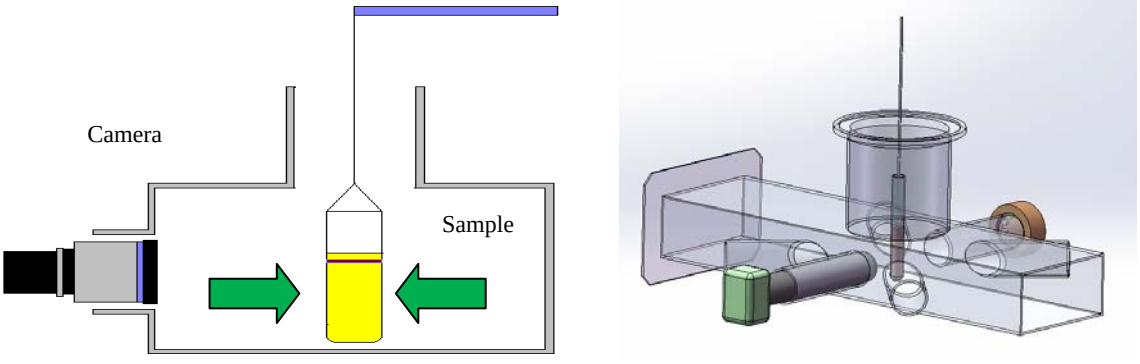
Fig. 1 shows a tube-guide MW reactor (Shikoku Instrumentation), which is specially designed for preventing MW leakage and equipped with a microscope camera (Sigma Koki, model SK-TC202USB-AT) for in situ observation. We hung a test tube containing the solution by a thread at the center of the reactor. Immediately after pouring the ammonium solution onto the gel surface, we initiated MW irradiation for 30 min. Because the stripe pattern grows from the surface to the bottom, we gradually lifted up the test tube at a controlled speed to acquire photographs around the vertical stripe center, through the side of the reactor, with the fixed microscope. We measured the Liesegang pattern length via the pixel number between the top and bottom of the precipitation region, and we counted the stripes through the photographs every 5 min. This approach enables dynamic evaluation of Liesegang pattern propagation with respect to MW radiation. After 30 min, we measured the final temperature with an optical fiber (Anritsu Meter) because the solution temperature increases under irradiation.

2.2 Conventional Heating

We used an OB to maintain the solution temperature. The bath temperature was increased over the course of 30 min to the final temperature observed in the MW experiment. We poured ammonium solution into the test tube immersed in the OB, and photographed the stripe pattern after 30 min with the microscope camera.

Table 1 Experimental conditions.

	Gel concentrate C_g (wt%)	Salt concentrate C_c (mol/L)	MW output (W) or temperature (^oC)
MW	0.5, 1, 2	0.3, 0.6, 0.9	25 (W)
OB	0.5, 1, 2	0.3, 0.6, 0.9	40 (^oC)



(a) Side view (b) 3D view

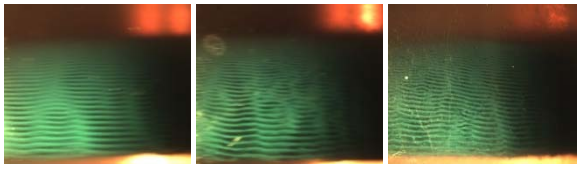
Fig. 1 MW reactor.

3. Results and Discussion

Figs. 2 and 3 show photographs of the stripe pattern near the gel surface for each gel concentration under MW or OB conditions after 30 min. The experiment involves precipitation after the salt concentration in the gel exceeds the critical values (i.e., the solubility due to ammonium ion diffusion). Although a stripe pattern was observed, an expected pattern transition (e.g., a tree-like pattern [1]) was not observed in this experiment. On the other hand, the parallel stripe pattern remained even under MW irradiation.

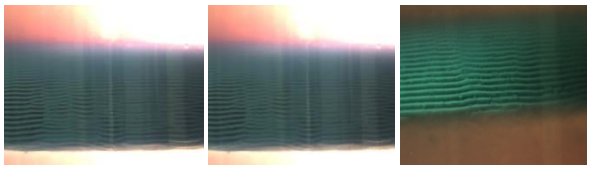
To aid in understanding the mechanism of stripe-pattern formation, Figs. 4 and 5 plot the stripe number and length, respectively, in relation to reaction time. Filled and open symbols indicate MW and OB conditions, respectively. Although precipitation starts just after contact with the ammonium solution, either the stripes do not immediately form or the camera resolution limit precludes sufficiently fast and precise image acquisition; accordingly, we assigned the initial number of stripes as 0. We counted the number of stripes after approximately 15-25 min. The stripe length linearly increased with reaction time (Fig. 5). After 30 min of reaction time, nonthermal effects induced by MW irradiation caused the stripe number and length to increase more rapidly for MW relative to OB. This is attributable to enhanced molecular diffusion and facilitated supersaturation. Molecular vibration induced by MW irradiation accelerates ionic diffusion. Moreover, such vibration readily induces supersaturation of the precipitate. Consequently, cyclic periods of supersaturation, nucleation, and depletion become faster. However, temperature must be carefully controlled to modulate such cycling.

Figs. 6 and 7 show an almost linear relation of stripe number and length, after 30 min of irradiation, with respect to $Co(NO_3)_2$ concentration. MW imparted a greater effect than OB in case of the lower salt concentration. Consequently, MW irradiation more effectively induced precipitation via supersaturation.



(a) C_g = 0.5 wt% (b) C_g = 1.0 wt% (c) C_g = 2.0 wt%

Fig. 2 Stripe pattern under MW at C_c = 0.3 mol/L.



(a) C_g = 0.5 wt% (b) C_g = 1.0 wt% (c) C_g = 2.0 wt%

Fig. 3 Stripe pattern in OB at C_c = 0.3 mol/L.

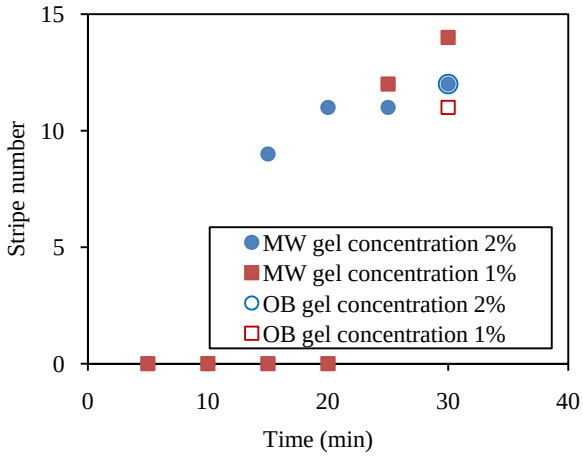


Fig. 4 Stripe number for the time at C_c = 0.9 mol/L.

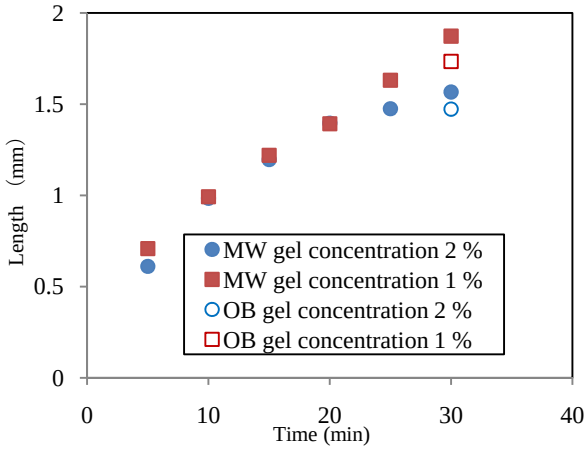


Fig. 5 Pattern length for the time at C_c = 0.9 mol/L.

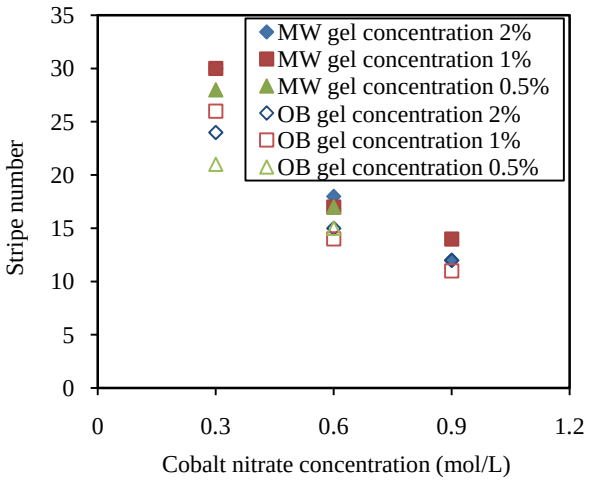


Fig. 6 Stripe number for the cobalt concentration after 30 min.

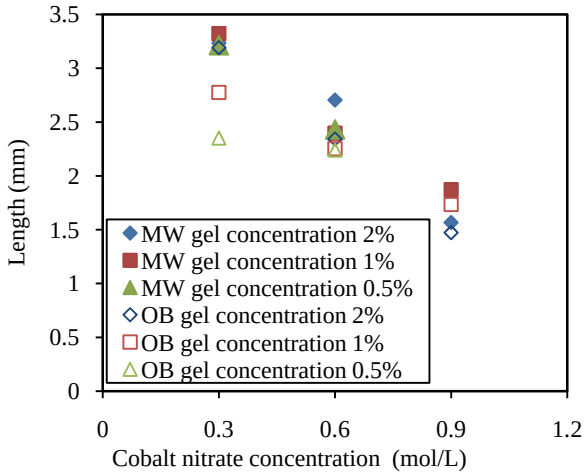


Fig. 7 Pattern length for cobalt concentration after 30 min.

4. Conclusions

To understand the mechanisms of precipitation and diffusion in Liesegang patterns, experiments varying the salt and gel concentrations were conducted in an oil bath and MW reactor equipped with in situ observation system. Stripe length and number increased more quickly with respect to time under MW irradiation than oil bath heating, and also decreased with respect to salt concentration. In particular, stronger MW effect was confirmed at lower salt condition. We explained these findings in the context of nonthermal effects (i.e., higher molecular diffusion and facilitated supersaturation) that are accelerated by radiation-induced molecular vibration. MW irradiation can modulate the diffusion and manifestation of Liesegang patterns, and may be a useful tool in other fine-scale, nonequilibrium self-organization processes that involve precipitation and nonlinearity.

References

[1] Lagzi, I.; Ueyama, D. Pattern Transition between Periodic Liesegang Pattern and Crystal Growth Regime in Reaction-Diffusion Systems. *Chemical Physics Letters* **2009,** *468,* 188-192.

[2] Toramaru, A.; Harada, T.; Okamura, T. Experimental Pattern Transitions in a Liesegang System. *Physica D* **2003,** *183,* 133-140.

[3] Sultan, R.; Ortoleva, P.; DePasquale, F.; Tartaglia, P. Bifurcation of the Ostwald-Liesegang Supersaturation-Nucleation-Depletion Cycle. *Earth-Science Reviews* **1990,** *29,* 163-173.

[4] Menke, Y.; Chiaretta, D.; Milanese, D.; Ferraris, M. MW Assisted Diffusion of Au-Nanoclusters in Vitreous Silica. *Journal of Non-crystalline Solids* **2006,** *352,* 2526-2531.

[5] Clemente, R. R.; Morales, J. G. MW Precipitation of $CaCO_3$ from Homogeneous Solutions. *Journal of Crystal Growth* **1996,** *169,* 339-346.

[6] Das, I.; Singh, P.; Agrawal, N. R.; Rastogi, R. P. Liesegang Ring Type Structures and Bifurcation in Solid-Vapor and Liquid Phase Reactions between Cobalt Nitrate and Ammonium Hydroxide. *Journal of Colloid and Interface Science* **1997,** *192,* 420-431.

[7] Msharrafieh, M.; Sultan, R. Dynamics of a Complex Diffusion-Precipitation-Re-Dissolution Liesegang Pattern. *Chemical Physics Letters* **2006,** *421,* 221-226.

J. Chem. Chem. Eng. 8 (2014) 335-343

Calf Thymus DNA Intercalation by Anionic Ru(III) Complexes Containing Tridentate Schiff Bases Derived from 5-X-Substituted Salicyladehyde and 2-Aminophenol

Emira Kahrovic*, Adnan Zahirovic and Emir Turkusic

Department of Chemistry, Faculty of Science, University of Sarajevo, Sarajevo 71000, Bosnia and Herzegovina

Received: February 24, 2014 / Accepted: March 15, 2014 / Published: April 25, 2014.

Abstract: Sodium bis[N-2-oxyphenyl-5-substituted-salicylideneiminato-ONO]ruthenate(III) hemitriethylamine compounds of general formula $Na[Ru(N\text{-}R\text{-}5\text{-}X\text{-}salim)_2]\cdot 0.5Et_3N$, where, R = C_6H_4O, X = Cl, Br, NO_2, salim = salicylideneiminato, Et_3N triethylamine, were synthesized and characterized on the basis of elemental analysis, MALDI-TOF (matrix-assisted laser desorption/ionization/time-of-flight) mass spectra, ^1H NMR (nuclear magnetic resonance), electronic spectra and cyclic voltammograms. Ru(III) is chelated with two O_2N anionic tridentate Schiff bases derived from 5-X-salicyladehyde and 2-aminophenol. Spectroscopic titrations of the Ru(III) compounds with CT DNA (calf thymus DNA) in the LMCT (ligand metal charge transfer) region have shown moderate intercalation properties of compounds with binding constants $K_b = 2.06\text{-}3.85 \times 10^4\ M^{-1}$. Electrochemical evidence of intercalative mode of binding is based on the decrease of current and shift of anodic and cathodic peaks towards higher values of potential with μL-increment of CT DNA in Ru(III) compound solution.

Key words: Ruthenium, Schiff bases, salicylideneimine, CT DNA, intercalation.

1. Introduction

Ruthenium complexes are the subject of increasing interest in chemistry and interdisciplinary fields of science due to many significant properties, especially anticancer and antimetastatic properties [1-8] and the ability to catalyze a number of organic reactions [9-12] and the aging.

A number of ruthenium complexes showed electron transfer capability as a key feature in the development of new sensors [13-14], and appropriate thermal and electrical properties essential for applications in solar cells [15]. In the development of new compounds, as potential antitumor agents, DNA is still considered as the primary target. Metal compounds are known to bind DNA by covalent or non-covalent mode. For covalent, either inter- or intra-strand mode of binding, easily leaving groups, e.g., chlorides, are generally required. Non-covalent binding mainly assumes groove binding or intercalation which means insertion of fused and planar aromatic moiety between base pairs of DNA. Many metal complex species, in particular neutral or positively charged, with some typical intercalating organic molecules containing extended π-electronic system, e.g., 2,2-bipyridine (bipy) or 1,10-phenanthroline (phen) have shown ability to intercalate DNA [16-21]. Some Ru(III) complexes with such ligands have also shown the property to bind DNA by intercalation [22-24].

Schiff bases derived from salicyladehyde, either as neutral or anionic species, are considered to be very functional ligands, therefore many metal complexes

*Corresponding author: Emira Kahrovic, Professor/Ph.D., research field: inorganic chemistry. E-mail: emira_kahrovic@yahoo.com.

with this type of ligands were reasonably synthesized for different purposes. Some of ruthenium complexes which contain ON (oxygen, nitrogen) or ONO (oxygen, nitrogen, oxygen) anionic salicylidenimine as ligands showed antifungal and antibacterial activity [25-27]. Recently, we reported the DNA binding properties of two anionic Ru(III) compounds containing anionic bidentate salicylidenimine ligands and two chlorides [28].

In continuation of our study on synthesis and characterization of Ru(III) compounds with Schiff bases and interaction with DNA, we report herein on Ru(III) compounds containing two anionic O_2N Schiff bases derived from 5-substituted-salicylaldehyde and 2-aminophenol and study of interaction with CT DNA (calf thymus DNA).

2. Experiments

All chemicals of analytical grade were purchased from Sigma Aldrich and Merck and were used without further purification. Calf thymus DNA type I-fibrous (A_{260}/A_{280} = 1.3) was purified with phenol-chloroform-isoamyl alcohol procedure until ratio A_{260}/A_{280} = 1.8 was obtained and then DNA was precipitated as sodium salt by adding 0.1 M acetate buffer (pH 4.60) and ethanol. The precipitate was dried at 50 °C and kept at 4 ºC for further use. Solid nucleic acid of sufficient purity was suspended in 0.1 M Tris-HCl buffer, pH 7.40, and left one day for hydration at 4 ºC. The stock solution of CT DNA was prepared in Tris-HCl buffer at pH 7.40 and stored at 4 ºC for a maximum of 1-4 days. The concentration of CT DNA solution was calculated on the basis of DNA extinction coefficient ε = 6,600 $M^{-1}\cdot cm^{-1}$.

2.1 Synthesis

2.1.1 General Procedure for Synthesis of Na[Ru(N-R-5-X-salim)$_2$]·0.5 Et_3N

The solution of 0.76 mmol of appropriate N-2-hydroxyphenyl-5-X-salicylideneimine (X = Cl, Br, NO_2) in 50 mL absolute ethanol was mixed with 0.76 mmol triethylamine, afterwards 0.38 mmol $RuCl_3\cdot 3H_2O$ in 5 mL absolute ethanol was added. The solution was heated in a rotary evaporator at 60-70 °C during 4 h and then was cooled to room temperature. Small volume of water solution (0.5 mL) containig 0.38 mmol NaCl was added and resulting solution was left over night at ambient temperature. The precipitate was filtered off, washed with cold water, ethanol and petrol ether. Recrystallization was performed from absolute ethanol/dichlormetan (1/1, v/v). The compounds were dried at 80 °C. Yield: 60%-71%.

2.1.2 Na[Ru(N-R-5-Cl-salim)$_2$]·0.5Et_3N

Anal. Calc. for $NaRuC_{26}H_{16}Cl_2N_2O_4\cdot 0.5C_6H_{15}N$ (%): C 52.30, H 3.56, N 5.26. Found (%): C 52.32, H 4.15, N 5.55. MALDI-TOF/TOF MS *m*/*z*: 591.9534 ($[C_{26}H_{16}N_2O_4Cl_2Ru]^-$, 100%). IR (KBr) ν_{max}/cm^{-1}: 1,598 vs (C=N), 1,287 m (C-O_{phen}), 1,033 w (C_2N). IR (CsI) ν_{max}/cm^{-1}: 460 w (Ru-N), 387 w (Ru-O). UV/Vis [CH_2Cl_2, λ_{max}/nm]: 344, 395, 580 ($\varepsilon/M^{-1}\cdot cm^{-1}$): 12,394, 14,457, 5,320. ^{1}H NMR (nuclear magnetic resonance) Na [Ru(*N*-R-5-Cl-salim)$_2$]·0.5 $C_6H_{15}N$ (600 MHz, acetone-d6) δ 10.23 s (4 H_d), 7.94 dd (4 H_c, *J* = 8.0 Hz, 0.5 Hz), 7.82 td (4 H_g, *J* = 6.9 Hz, 1.3 Hz), 7.54 dd (4 H_e, *J* = 8.8 Hz, 2.8 Hz), 7.34 dd (4 H_a, *J* = 7.9 Hz, 0.8 Hz), 7.12 dd (4 H_h, *J* = 9.0 Hz, 2.7 Hz), 6.88 td (4 H_f, *J* = 7.5 Hz, 4.1 Hz), 3.10 q (6 H_j, *J* = 4.7 Hz), 1.18 t (9 H_i, *J* = 7.3 Hz).

2.1.3 Na[Ru(N-R-5-Br-salim)$_2$]·0.5Et_3N

Anal. Calc. for $NaRuC_{26}H_{16}Br_2N_2O_4\cdot 0.5\ C_6H_{15}N$ (%): C 46.14, H 3.14, N 4.64. Found (%): C 47.46, H 3.84, N 5.04. MALDI-TOF/TOF MS *m*/*z*: 681.8532 ($[C_{26}H_{16}N_2O_4\ Br_2Ru]^-$, (100%). IR (KBr) ν_{max}/cm^{-1}: 1,598 vs. (C=N), 1,286 m (C-O_{phen}), 1,032 w (C_2N). IR (CsI) ν_{max}/cm^{-1}: 469 w (Ru-N), 393 w (Ru-O). UV/Vis [CH_2Cl_2, λ_{max}/nm]: 345, 391, 588 ($\varepsilon/M^{-1}\ cm^{-1}$): 13,060, 14,461, 5,150. ^{1}H NMR Na[Ru(*N*-R-5-Br-salim)$_2$]·0.5 $C_6H_{15}N$ (600 MHz, acetone-d6) δ 10.21 s (4 H_d), 7.93 dd (4 H_c, *J* = 8.0 Hz, 0.6 Hz), 7.82 td (4 H_g, *J* = 8.2 Hz, 1.1 Hz), 7.77 dd (4 H_a, *J* = 2.5 Hz, 0.8 Hz), 7.65 dd (4 H_e, *J* = 8.8 Hz, 2.6 Hz), 7.21 dd (4 H_h, *J* = 9.0 Hz, 2.5 Hz), 7.03 td (4 H_f,

J = 7.9 Hz, 0.9 Hz), 3.09 q (6H_j, *J* = 4.4 Hz), 1.18 t (9 H_i, *J* = 7.3 Hz).

2.1.4 Na[Ru(N-R-5-NO_2-salim)$_2$]·0.5Et_3N

Anal. Calc. for $NaRuC_{26}H_{16}N_4O_8$·0.5 $C_6H_{15}N$ (%): C 50.69, H 3.45, N 9.17. Found (%): C 49.58, H 4.05, N 8.63. MALDI-TOF/TOF MS *m*/*z*: 614.0018 ($[C_{26}H_{16}N_4O_8Ru]^-$, 100%). IR (KBr) ν_{max}/cm^{-1}: 1,595 vs. (C=N), 1,300 m (C-O $_{phen}$), 1,033 w (C_2N). IR (CsI) ν_{max}/cm^{-1}: 471 w (Ru-N), 384 w (Ru-O). UV/Vis [CH_2Cl_2, λ_{max}/nm]: 335, 371, 589 ($\varepsilon/M^{-1}\,cm^{-1}$): 17,273, 18,941, 5,137. ^{1}H NMR Na[Ru(*N*-R-5-NO_2-salim)$_2$]·0.5 $C_6H_{15}N$ (600 MHz, acetone-d6) δ 10.28 s (4 H_d), 9.68 dd (4 H_c, *J* = 7.7 Hz, 0.24 Hz), 8.16 dd (4 H_a, *J* = 2.3 Hz, 0.5 Hz), 8.33 dd (4 Hb, *J* = 9.1 Hz, 2.8 Hz), 8.03 dd (4 H_e, *J* = 8.3 Hz, 0.84 Hz), 7.92 td (4 H_g, *J* = 9.3 Hz, 2.7 Hz),7.38 dd (4 H_h, *J* = 8.52 Hz, 0.82 Hz), 7.06 td (4 H_f, *J* = 8.4 Hz, 1.3 Hz), 3.10 q (6H_j, *J* = 7.2 Hz), 1.18 t (9 H_i, *J* = 7.3 Hz).

2.2 Physical Measurements

Mass spectra were recorded on a complex matrix-assisted laser desorption/ionization-time-of-flight MALDI-TOF/TOF mass spectrometer (4800 Plus MALDI TOF/TOF Analyzer, Applied Biosystems Inc., Foster City, CA, USA) equipped with Nd: YAG laser, wavelength of 355 nm. The sample was resuspended in 10 μL THAP/DAC MALDI matrix (1.9 mg 2,4,6-Trihydroxyacetophenone and 2.3 mg ammonium hydrogen citrate in 1 mL mixed solvent acetonitrile/H_2O, 1/1, v/v) and 1 μL was set on the MALDI plate. Mass spectra were recorded at 200 Hz in a negative mode, in the range *m*/*z* values 10-1,000 Da with focus on the mass 500 Da. As an internal standard in the negative mode, riboflavin and 3-aminosalicylic acid were used.

^{1}H NMR spectra were recorded on 600 MHz Bruker BioSpin GmbH instrument in acetone-d6 using TMS (tetramethylsilane) as internal standard.

Infrared spectra were collected on Perkin Elmer BX FT-IR (fourier transform infrared) spectrophotometer as KBr pallets in the region 4,000-400 cm^{-1} and for detection Ru-N and Ru-O absorptions CsJ pallets were used in the region 600-380 cm^{-1}.

Electronic spectra were recorded on Perkin Elemer UV/visible lambda 35 spectrophotometer in CH_2Cl_2 solution over the range 200-700 nm.

Cyclic voltammograms of Na[Ru(N-R-5-X-salim)$_2$]·0.5Et_3N were recorded on an electrochemical workstation Autolab potentiostat/galvanostat (PGSTAT 12) using three electrode system: glassy carbon electrode as working, Ag/AgCl as reference electrode and Pt wire. We used acetonitrile as solvent and tetraethylammonium perchlorate as supporting electrolyte. Electrochemical titrations of Na[Ru(N-R-5-X-salim)$_2$]·0.5Et_3N with CT DNA were performed on the same instrument with the same three-electrode system in Tris-HCl buffered water solutions in potential range -1.0 V to -0.1 V. The compounds were initially dissolved in DMSO (dimethyl sulfoxide), afterwards diluted with Tris-HCl buffer, pH = 7.40, in the presence of 150 mM NaCl, up to a total volume of 2 mL. DNA is added in 25 μL portions and cyclic voltammograms were recorded after each addition of DNA.

Spectroscopic titration of Ru(III) compounds with CT DNA was performed by the successive addition of DNA (six portions of 10 μL) in 2 mL of the compound solutions at pH 7.40 in the presence of 150 mM NaCl. Spectra were recorded 2 min after addition of the DNA in the range 200-700 nm. Each addition of DNA was compensated in the blank.

3. Results and Discussion

3.1 Synthesis

N-2-hydroxyphenyl-5-substituted-salicylideneimines, N-RH-5-X-salimH, were prepared from absolute ethanol solutions containing equimolar quantities of 2-aminophenol and 5-X-salicyladehyde where X = Cl, Br, NO_2. Reactions were performed at 50 °C during 20 min. The orange solids were purified by recrystallization from warm absolute ethanol with good yields of 80%-90%.

Sodium bis[N-2-oxyphenyl-5-substituted-salicylideneiminato-ONO]ruthenate(III), $Na[Ru(N\text{-}R\text{-}5\text{-}X\text{-}salim)_2]\cdot 0.5Et_3N$, where, X = Cl, Br, have been synthesized according to published procedure for complex anions [29], but for the purpose of interaction with DNA, the complex anions were precipitated as sodium salts. The compound containing NO_2 substituted salicylidenimine was prepared as an analogue. The starting compounds $RuCl_3\cdot 3H_2O$ and N-RH-5-X-salimH were used in molar ratio 1:2. Deprotonation of phenolic oxygen atoms from ligands was performed by adding triethylamine in molar ratio 1:2, respectively. Reactions were performed at 60-70 ºC for 4 h in rotary evaporator. The precipitation was performed with stoichiometric amounts of NaCl in water solution. The scheme of synthesis is shown in Fig. 1. The solids are stable in air, insoluble in water, soluble in acetonitrile, N,N-DMF (dimethylformamide), acetone, ethyl alcohol, DMSO, dichlormethane.

On the basis on CHN (carbon nitrogen hydrogen) elemental analysis, mass spectra, ^{1}H NMR, infrared and UV/visible spectroscopic measurements the compounds were formulated as $Na[Ru(N\text{-}R\text{-}5\text{-}X\text{-}salim)_2]\cdot 0.5Et_3N$. Mass spectra showed molecular ions (M^-) at *m/z* (100%) at 591.9534, 681.8532, 614.0018 for $[RuC_{26}H_{16}Cl_2N_2O_4]^-$, $[RuC_{26}H_{16}Br_2N_2O_4]^-$ and $[RuC_{26}H_{16}N_4O_8]^-$, respectively.

Ru(III) in octahedral coordination is chelated with two O_2N tridentate Schiff bases trough azomethine nitrogen and deprotonated phenolic oxygen atoms. Elemental analysis, IR and ^{1}H NMR spectra are in accordance with presence of one solvate molecule of triethylamine per two complex anions.

3.2 Spectroscopic Measurements

3.2.1 ^{1}H NMR Spectra

^{1}H NMR spectra of $Na[Ru(N\text{-}R\text{-}5\text{-}X\text{-}salim)_2]\cdot 0.5Et_3N$ showed absence of singlet in region 10 ppm to 12 ppm

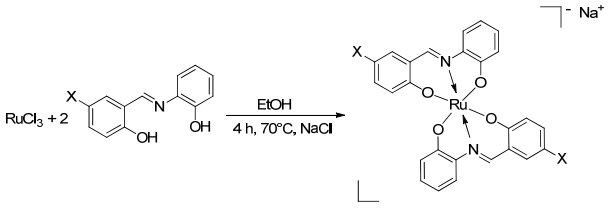


Fig. 1 Synthesis of $Na[Ru(N\text{-}R\text{-}5\text{-}X\text{-}salim)_2]$, (X = Cl, Br, NO_2).

corresponding to phenolic hydrogen, consequently confirming that N-2-oxyphenyl-5-X-salicylideneimines bind Ru(III) via deprotonated phenolic oxygen atoms. Singlets, positioned in this region (10.21 ppm to 10.28 ppm), with small variations in the chemical shift (0.09 ppm), correspond to azomethine hydrogen which is slightly sensitive to 5-X substituent on salicylaldehyde. The positions of azomethine singlet correspond to hydrogen bonding of azomethine group with triethylamine. Four doublets of doublets and two triplets of doublets in region 7 ppm to 9 ppm correspond to six aromatic hydrogen atoms with ortho-coupling constants J_{HH} between 7.9 Hz and 9.3 Hz and metha-coupling constants J_{HH} 0.8 Hz to 2.6 Hz. Quartet at 3.1 ppm and triplet at 1.18 ppm confirm methylene and methyl hydrogen respectively in ratio 1:1.5. ^{1}H NMR data strongly support proposed structures of complexes. Different hydrogen atoms in the structure of $[Ru(N\text{-}R\text{-}5\text{-}X\text{-}salim)_2]^-\cdot 0.5Et_3N$ are shown in Fig. 2.

3.2.2 Infrared Spectra

Infrared spectra of free Schiff bases and $Na[Ru(N\text{-}R\text{-}5\text{-}X\text{-}salim)_2]\cdot 0.5Et_3N$ are in accordance with coordination trough azomethine nitrogen and

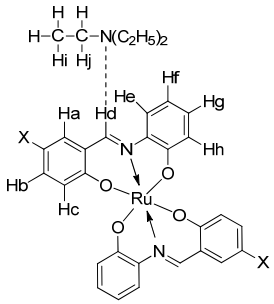


Fig. 2 The structure of $[Ru(N\text{-}R\text{-}5\text{-}X\text{-}salim)_2]^-\cdot 0.5Et_3N$ with different hydrogen atoms which correspond to ^{1}H NMR spectra.

both phenolic oxygen atoms in Schiff base. The characteristic frequencies of compounds and free ligands are given in Table 1. Azomethine group appears in spectra of free N-RH-5-X-salimH at 1,630-1,629 cm^{-1} while after coordination the frequency of azomethine is significantly shifted toward lower values for 32-29 cm^{-1} and appears in corresponding $Na[Ru(N\text{-}R\text{-}5\text{-}X\text{-}salim)_2]\cdot 0.5Et_3N$ compounds at 1,598-1,595 cm^{-1}. Coordination through deprotoned phenolic oxygen caused the shift of C-O absorption towards higher values of wave numbers for 15-19 cm^{-1} as a result of the formation of C-O(Ru) instead of C-O(H) group. Phenolic C-O(H) frequencies appear at 1,272-1,281 cm^{-1} in free ligands, while in $Na[Ru(N\text{-}R\text{-}5\text{-}X\text{-}salim)_2]\cdot 0.5Et_3N$ were found at 1,287-1,300 cm^{-1}. The presence of solvate triethylamine molecule is in accordance with weak frequencies corresponding to C_2N asymmetric stretching at 1,033-1,032 cm^{-1} and also with broad absorptions centred on 3,430 cm^{-1} which can be attributed to $Et_3N\cdots H$ (azomethine) secondary interaction. Weak Ru-N and Ru-O frequencies in $Na[Ru(N\text{-}R\text{-}5\text{-}X\text{-}salim)_2]\cdot 0.5Et_3N$ were found at 460-471 cm^{-1} and 387-384 cm^{-1}, respectively.

3.2.3 Electronic Spectra

Electronic spectra of free N-RH-5-X-salimH and $Na[Ru(N\text{-}R\text{-}5\text{-}X\text{-}salim)_2]\cdot 0.5Et_3N$, recorded in dichloromethane, are in good agreement with the mode of coordination of the ligands. Electronic spectra of free Schiff bases have three or four in the case of X = NO_2 compound, well-defined absorption bands (Table 2). Coordination of Schiff bases significantly changes the position of the n(O)→π* and n(N)→π* bands by moving them toward higher and lower wavelength respectively due to bonding trough deprotonated phenolic oxygen and lone pair on azomethine nitrogen. Two new bands were found in the spectra of complex compounds, LMCT bands in the region 371-395 nm and very weak, broad and poorly defined absorptions in the region 580-589 nm corresponding to $t_{2g}^5 \rightarrow t_{2g}^4 e_g^1$ spin-allowed electron transition of low-spin Ru(III).

3.3 Cyclic Voltammetry

Cyclic voltammograms of $Na[Ru(N\text{-}R\text{-}5\text{-}X\text{-}salim)_2]\cdot 0.5Et_3N$ were recorded in acetonitrile in the presence of tetraethylammonium perchlorate as supporting electrolyte using glassy carbon working electrode (Fig. 3).

The ratio i_k/i_a and E_k-E_a separations in cyclic voltammograms indicate quasi-reversible one-electron processes. Cathodic peaks appear in the potential range -883 mV to -915 mV, anodic peaks at -712 mV to -742 mV with peaks separations 141-183 mV. Formal potentials $E_{1/2}$, assigned to Ru(III)/Ru(II) couple, are quite negative varying from -804 mV to -824 mV. The characteristic potentials are given in Table 3. The values are consistent with increased stabilization of Ru(III) through $[RuO_4N_2]$ skeleton compared to $[RuO_2N_2]$ in the compounds with similar type of ligand [28].

3.4 *Calf Thymus DNA Binding*

3.4.1 Spectroscopic Evidence for Intercalation

Study of the interaction of metal compounds with DNA is an important step in the evaluation of the biological properties of the compounds. Many metal complexes with fused and planar aromatic ligands, or aromatic heterocyclic rings, are described as DNA intercalators. In addition, external minor or major groove binding or external binding to the phosphate backbone is possible. Spectrophotometric titration of

Table 1 IR frequencies for $Na[Ru(N\text{-}R\text{-}5\text{-}X\text{-}salim)_2]\cdot 0.5Et_3N$ and N-RH-5-X-salimH.

X	ν(CH=N) (cm^{-1})	ν(C-O) (cm^{-1})	ν(Ru-N) (cm^{-1})	ν(Ru-O) (cm^{-1})
Cl	1,598 (1,630)	1,287 (1,272)	460 (-)	387 (-)
Br	1,598 (1,629)	1,286 (1,270)	469 (-)	387 (-)
NO_2	1,595 (1,629)	1,300 (1,281)	471 (-)	384 (-)

Values in parentheses refer to the free ligand N-RH-5-X-salimH.

Table 2 Electronic spectra of Na[Ru(N-R-5-X-salim)$_2$]·0.5Et$_3$N and N-RH-5-X-salimH.

X	$\lambda[\pi\rightarrow\pi^*]$ (nm)	λ[n(O)$\rightarrow\pi^*$] (nm)	λ[n(N)$\rightarrow\pi^*$] (nm)	λ[LMCT] (nm)
Cl	230 (230)	296 (269)	344 (366)	395 (-)
Br	230 (230)	297 (269)	345 (366)	391 (-)
NO_2	233 (229)	295 (266)	335 (347)	371 (-)

Values in parentheses refer to the free ligand N-RH-5-X-salimH.

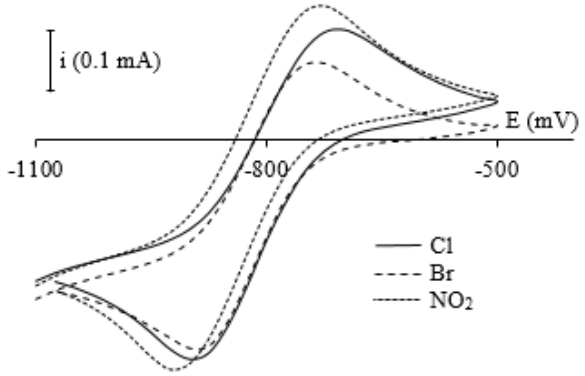


Fig. 3 Cyclic voltammograms of Na[Ru(N-R-5-X-salim)$_2$]·0.5Et$_3$N (X = Cl, Br, NO$_2$) in acetonitrile/tetraethyammonium perchlorate; working electrode GCE vs. Ag/AgCl; scan rate 300 mV·s^{-1}.

Table 3 The potentials of Na[Ru(N-R-5-X-salim)$_2$]·0.5Et$_3$N.

X	E_k (mV)	E_a (mV)	$E_{1/2}$ (mV)	ΔE_p (mV)
Cl	-895	-712	-804	183
Br	-883	-742	-812	141
NO_2	-915	-734	-824	181

metal complex with DNA is a useful method to estimate binding mode and calculate binding constant K_b. In this work, spectroscopic study of interaction of Na[Ru(N-R-5-X-salim)$_2$]·0.5Et$_3$N with CT DNA was carried out by titrating a fixed amount of the complex with increasing amount of calf thymus CT DNA. The [DNA]/[complex] ratio was between 0-2.28 for chloro, 0-1.54 for bromo- and 0-2.30 for NO_2 derivative. The binding constants K_b were calculated on the basis of Eq. (1) [30]:

$$\frac{[\mathrm{DNA}]}{(\varepsilon_a-\varepsilon_f)}=\frac{[\mathrm{DNA}]}{(\varepsilon_b-\varepsilon_f)}+\frac{1}{K_b(\varepsilon_a-\varepsilon_f)} \quad (1)$$

where, ε_a, ε_f and ε_b represent extinction coefficients for particular measurements (A_{obs}/[DNA]), free complex and completely bound form, respectively. The binding constant K_b is obtained as the ratio of the slope and Spectroscopic titration and graphical calculation of intercept in graph [DNA]/($\varepsilon_a - \varepsilon_f$) vs. [DNA]. binding constant are shown in Figs. 4 and 5. Apparent hypochromism in the region of LMCT absorptions and values of K_b (2.06-3.85 × 10^4 M^{-1}) designate Na[Ru(N-R-5-X-salim)$_2$]·0.5Et$_3$N as moderate DNA-intercalators. The binding constants are given in Table 4. The impact of 5-X-substituent on intercalative

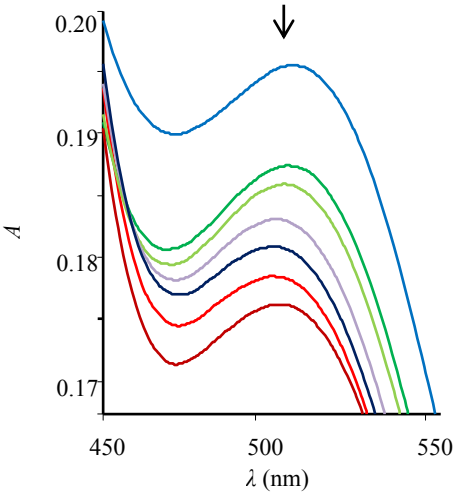


Fig. 4 The spectroscopic titration of 31.5 μM Na[Ru(N-R-5-Br-salim)$_2$]·0.5Et$_3$N with increasing concentration of CT DNA (0-49 μM) in Tris-HCl buffer, pH 7.40 and 150 mM NaCl.

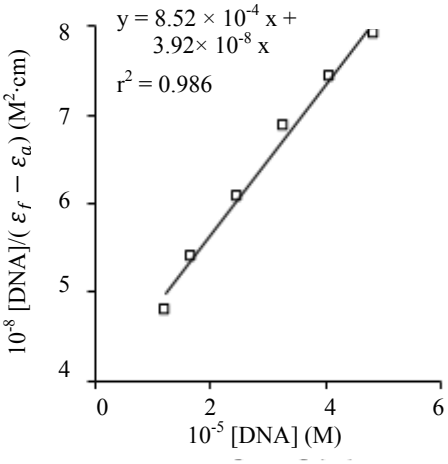


Fig. 5 Plot of ($\varepsilon_f - \varepsilon_a$) vs. [DNA]/[DNA].

Table 4 The binding constants of $Na[Ru(N\text{-}R\text{-}5\text{-}X\text{-}salim)_2]\cdot 0.5Et_3N$ to CT DNA.

X	$10^4 K_b$ (M^{-1})
Cl	2.06
Br	2.18
NO_2	3.85

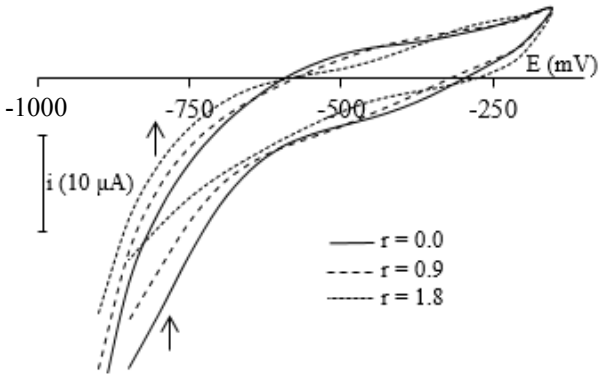


Fig. 6 Electrochemical evidence for intercalation 29 μM $Na[Ru(N\text{-}R\text{-}5\text{-}Cl\text{-}salim)_2]\cdot 0.5Et_3N$ in the presence of increasing concentration of CT DNA (0-50 μM) under phisiological condition: Tris-HCl, pH 7.40, 150 mM NaCl; working electrode GCE vs. Ag/AgCl; scan rate 800 mV·s^{-1}; step potential 50 mV.

activities of the compounds correlates with electron withdrawing properties and ability of substituent to decrease electron density from π-system making it less nucleophilic.

3.4.2 Electrochemical Evidence for Intercalation

Cyclic voltammetry is also a useful technique available for studying the interaction of metal complexes with DNA. Procedure is carried out by successive adding of μL-volumes of DNA to the solution containing fixed amount of $Na[Ru(N\text{-}R\text{-}5\text{-}X\text{-}salim)_2]\cdot 0.5Et_3N$. Intercalation is followed by the current decrease and shift of cathodic and anodic peaks towards more positive values of potentials, though the peaks are poorly visible in aqueous solution due to insolubility of compounds in water (Fig. 6). The molar ratio *r* [DNA]/[complex] was within the range 0-1.8 for X = Cl, and 0-1.5 for X= Br, NO_2.

4. Conclusions

We reported here on synthesis of Ru(III) compounds with 5-X substituted salicylideneimine ligands derived from salicylaldehyde and 2-aminophenol. The compounds of the general formula $Na[Ru(N\text{-}R\text{-}5\text{-}X\text{-}salim)_2]\cdot 0.5Et_3N$ were synthesized and characterized by elemental analysis, different spectroscopic techniques and cyclic voltammetry. Ruthenium is chelated by two tridentate Schiff base in RuO_4N_2 octahedral skeleton. The interaction with CT DNA was studied by spectrophotometric titration and cyclic voltammetry indicating capability of compounds to intercalate CT DNA. The quantification of affinity of each compound toward DNA was done by binding constants, K_b = 2.06-3.85 × 10^4 M^{-1} which correspond to intercalative mode of binding. The absorption spectral bands at LMCT region showed hypochromism in the presence of increasing amount of DNA. The lack of measurable evidence for redshift is in accordance with values of binding constants and moderate intercalating properties of the compounds. Substituent X in $Na[Ru(N\text{-}R\text{-}5\text{-}X\text{-}salim)_2]\cdot 0.5Et_3N$ affects an increase of binding constants with increasing electron withdrawing properties of substituent in order Cl ~ Br < NO_2.

Acknowledgments

This work was supported by Federal Ministry of Education and Science, Bosnia and Herzegovina, Project No. 05-39-4390-1/13.

References

[1] Hartmann, M.; Keppler, B. K. Inorganic Anticancer Agents: Their Chemistry and Antitumor Properties. *Comments Inorg. Chem.* **1995,** *16(6),* 339-372.

[2] Keppler, B. K. Metal Complexes as Anticancer Agents—The Future Role of Inorganic Chemistry in Cancer Therapy. *New J. Chem.* **1990,** *14(6-7),* 389-403.

[3] Keppler, B. K.; Berger, M. R.; Klenner, T.; Heim, M. E. Metal Complexes as Antitumor Agents. *Adv. Drug Res.* **1990,** *19*, 243-310.

[4] Alessio, E.; Mestroni, G.; Bergamo, A.; Sava, G. Ruthenium Anticancer Drugs. *Met. Ions Biol. Syst.* **2004,** *42,* 323-352.

[5] Sava, G.; Pacor, S.; Mestroni, G.; Alessio, E. Na[trans-$RuCl_4$(DMSO)Im], a Metal Complex of

Ruthenium with Antimetastatic Properties. *Clin. Exp. Metastasis* **1992,** *10(4),* 273-280.

[6] Alessio, E.; Mestroni, G.; Bergamo, A.; Sava, G. Ruthenium Antimetastatic Agents. *Curr. Top. Med. Chem.* **2004,** *4(15),* 1525-1535.

[7] Van, R. S. H.; Sadler, P. J. Current Applications and Future Potential for Bioinorganic Chemistry in the Development of Anticancer Drugs. *Drug Discovery Today.* **2009,** *14(23),* 1089-1097.

[8] Bratsos, I.; Jedner, S.; Gianferrara, T.; Alessio, E. Ruthenium Anticancer Compounds: Challenges and Expectations. *Chimia Int. J. Chem.* **2007,** *61(11),* 692-697.

[9] Tominaga, K. I.; Sasaki, Y. Ruthenium Complex-Catalyzed Hydroformylation of Alkenes with Carbon Dioxide. *Catal. Commun.* **2000,** *1(1),* 1-3.

[10] Karvembu, R.; Hemalatha, S.; Prabhakaran, R.; Natarajan, K. Synthesis, Characterization and Catalytic Activities of Ruthenium Complexes Containing Triphenylphosphine/Triphenylarsine and Tetradentate Schiff Bases. *Inorg. Chem. Commun.* **2003,** *6(5),* 486-490.

[11] Cozzi, P. G. Metal-Salen Schiff Base Complexes in Catalysis: Practical Aspects. *Chem. Soc. Rev.* **2004,** *33(7),* 410-421.

[12] Cheung, K. C.; Wong, W. L.; Ma, D. L.; Lai, T. S.; Wong, K. Y. Transition Metal Complexes as Electrocatalysts—Development and Applications in Electro-Oxidation Reactions. *Coord. Chem. Rev.* **2007,** *251(17),* 2367-2385.

[13] Turkušić, E.; Kahrović, E. Development of New Low Potential Amperometric Sensor for L-cysteine Based on Carbon Ink Modification by Tetraethylamonium Dichloro-bis[N-phenyl-5-bromosalicylideniminato-N,O]r Uthenate(III). *TTEM* **2012,** *7(3),* 1300-1303.

[14] Kahrović, E.; Turkušić, E. New Ruthenium Complexes with Schiff Bases as Mediators for the Low Potential Amperometric Determination of Ascorbic Acid, Part II: Voltametric and Amperometric Evidence of Mediation with Bromo-derivative of Tetraethylamonium Dichloro-bis[N-phenyl-5-halogeno-salicylideniminato-N,O] Ruthenate(III). *HealthMED* **2012,** *6(3),* 1046-1049.

[15] Guimaraes, R. R.; Parussulo, A. L.; Toma, H. E.; Araki, K. New Tunable Ruthenium Complex Dyes for TiO_2 Solar Cells. *Inorg. Chim. Acta* **2013,** *404,* 23-28.

[16] Messori, L.; Marcon, G.; Innocenti, A.; Gallori, E.; Franchi, M.; Orioli, P. Molecular Recognition of Metal Complexes by DNA: A Comparative Study of the Interactions of the Parent Complexes [PtCl(TERPY)]Cl and [AuCl(TERPY)]Cl_2 with Double Stranded DNA. *Bioinorg. Chem. Appl.* **2005,** *3(3-4),* 239-253.

[17] Patel, K. K.; Plummer, E. A.; Darwish, M.; Rodger, A.; Hannon, M. J. Aryl Substituted Ruthenium Bis-terpyridine Complexes: Intercalation and Groove Binding with DNA. *J. Inorg. Biochem.* **2002,** *91(1),* 220-229.

[18] Önfelt, B.; Lincoln, P.; Nordén, B. Enantioselective DNA Threading Dynamics by Phenazine-Linked $[Ru(phen)2dppz]^{2+}$ Dimers. *J. Am. Chem. Soc.* **2001,** *123(16),* 3630-3637.

[19] Wang, X. L.; Chao, H.; Li, H.; Hong, X. L.; Liu, Y. J.; Tan, L. F.; et al. DNA Interactions of Cobalt(III) Mixed-Polypyridyl Complexes Containing Asymmetric Ligands. *J. Inorg. Biochem.* **2004,** *98(6),* 1143-1150.

[20] Mahadevan, S.; Palaniandavar, M. Spectral and Electrochemical Behavior of Copper(II)-Phenanthrolines Bound to Calf Thymus DNA. $[(5,6\text{-dimethyl-OP})2Cu]^{2+}$ (5,6-dimethyl-OP = 5,6-dimethyl-1,10-phenanthroline) Induces a Conformational Transition from B to Z DNA. *Inorg. Chem.* **1998,** *37(16),* 3927-3934.

[21] Maheswari, P. U.; Palaniandavar, M. DNA Binding and Cleavage Activity of $[Ru(NH_3)_4(diimine)]Cl_2$ Complexes. *Inorg. Chimi. Acta* **2004,** *357(4),* 901-912.

[22] Barton, J. K.; Danishefsky, A.; Goldberg, J. Tris (phenanthroline) Ruthenium(II): Stereoselectivity in Binding to DNA. *J. Am. Chem. Soc.* **1984,** *106(7),* 2172-2176.

[23] Satyanarayana, S.; Dabrowiak, J. C.; Chaires, J. B. Tris (phenanthroline) Ruthenium(II) Enantiomer Interactions with DNA: Mode and Specificity of Binding. *Biochem* **1993,** *32(10),* 2573-2584.

[24] Morgan, R. J.; Chatterjee, S.; Baker, A. D.; Strekas, T. C. Effects of Ligand Planarity and Peripheral Charge on Intercalative Binding of Ru(2,2'-bipyridine)$_2L_2^+$ to Calf Thymus DNA. *Inorg. Chem.* **1991,** *30(12),* 2687-2692.

[25] Dharmaraj, N.; Viswanathamurthi, P.; Natarajan, K. Ruthenium(II) Complexes Containing Bidentate Schiff Bases and Their Antifungal Activity. *Trans. Metal Chem.* **2001,** *26(1-2),* 105-109.

[26] Ramesh, R.; Maheswaran, S. Synthesis, Spectra, Dioxygen Affinity and Antifungal Activity of Ru(III) Schiff Base Complexes. *J. Inorg. Biochem.* **2003,** *96(4),* 457-462.

[27] Jayabalakrishnan, C.; Natarajan, K. Ruthenium(II) Carbonyl Complexes with Tridentate Schiff Bases and Their Antibacterial Activity. *Trans. Metal Chem.* **2002,** *27(1),* 75-79.

[28] Ljubijankić, N.; Zahirović, A.; Turkušić, E.; Kahrović, E. DNA Binding Properties of Two Ruthenium(III) Complexes Containing Schiff Bases Derived from Salicylaldehyde: Spectroscopic and Electrochemical Evidence of CT DNA Intercalation. *Croat. Chem. Acta* **2013,** *86(2),* 215-222.

[29] Kahrović, E.; Dehari, S.; Dehari, D.; Reçi, H.; Begić, S.;

Ljubijankić, N. Synthesis and Characterization of New Ru(III) Complexes with Monobasic (NO) and Dibasic (ONO) Schiff Bases Derived from Salicylaldehydes. *TTEM* **2010,** *5(4),* 799-803.

[30] Pyle, A. M.; Rehmann, J. P.; Meshoyrer, R.; Kumar, C. V.; Turro, N. J.; Barton, J. K. Mixed-ligand Complexes of Ruthenium(II): Factors Governing Binding to DNA. *J. Am. Chem. Soc.* **1989,** *111(8),* 3051-3058.

J. Chem. Chem. Eng. 8 (2014) 344-348

The Determination of Average Stability Constant of Nickel-FA Complex at pH = 8.0 by the Solubility Method

Giorgi Makharadze[1*], Nazi Goliadze[2], Tamar Makharadze[1] and Guram Supatashvili[1]

1. Department of Chemistry, Ivane Javakhishvili Tbilisi State University, Tbilisi 0128,Georgia

2. Department of Hydro Engineering, Georgian Technical University, Tbilisi 0175, Georgia

Received: February 20, 2014 / Accepted: February 28, 2014 / Published: April 25, 2014.

Abstract: At pH = 8, the complex formation process of Ni(II) ions with FA was studied by the solubility method. FA were separated from the river Mtkvari by the adsorption-chromotographic method. The charcoal (BAU, Russia) was used as a sorbent. The old suspension of Ni(II) hydroxide was used as the solid phase, on which was added the increasing quantity of standard solution of FA. In diluted solutions, at pH = 8.0 the dominant form of Ni(II) is nickel dihydroxocomplex $Ni(OH)_2^0$. It was established that in the $Ni(OH)_2$(solid)-$Ni(OH)_2^0$(solution)-FA^{2-}-H_2O system dominates nickel dyhydroxofulvate complex with the structure 1:1, $[Ni(OH)_2FA]^{2-}$. The average stability constant of nickel dyhydroxofulvate complex was calculated based on experimental data $\beta_{Ni(OH)_2FA^{2-}} = 5.3 \times 10^5$.

Key words: Nickel, FA, average stability constant, nickel fulvate, water.

1. Introduction

FA (fulvic acids) have the functional groups, so they take an active part in complexing and sorption processes, proceeding in natural waters, suspended substances, bottom sediment and soils. They form stable complexes with heavy metals and radionuclides and stipulate migration forms thereof in natural waters and soils [1-12].

The carboxylic and phenolic groups take part in fulvate complex formation processes [12-16]. $pK_{H,COOH}$ changes from 4.1 to 4.8, and $pK_{H,Ph-OH}$ changes from 9.3 to 10.5 [12, 17, 18].

In spite of researches, experimental data on stability constants of complex compounds of FA are heterogeneous. One of the reasons to this is application of various average molecular weights of FA associates. In its turn, this puts the correctness of calculation of stability constants of fulvic complexes under question.

Therefore, it is difficult to investigate complexing and sorption processes taking place in natural waters and soils, identify migration forms of heavy metals and radio nuclides, evaluate and assess chemical-ecological condition of natural waters and soils.

The authors' objective was to obtain pure samples of FA, to study complex formation processes between heavy metals and FA, to determine the structure and average stability constants of fulvic complexes.

In this paper, the authors discuss the complex formation process of nickel fulvate. According to the data, found in the literature, stability constants (β) of nickel fulvic complexes differ in several lines from each other. Value of lg β changes from 3.3 to 7.1 [19-22].

The complex formation process was studied at pH = 8.0 by the solubility method. The suspension of old nickel hydroxide was used as the solid phase.

2. Experiment Methodology

To obtain pure samples of FA, the authors

*Corresponding author: Giorgi Makharadze, Professor/Dr., research fields: analytical chemistry and environmental chemistry. E-mail: giorgi.makharadze@yahoo.com.

concentrated the water of the river Mtkvari by the frozen method. Filtered water samples were acidified to pH 2 and were put for 2 h on water bath at 60 °C, for coagulation of humin acids. Then, the solution was centrifuged for 10 min at 8,000 rpm. To isolate FA from centrifugate, the adsorption-chromotographic method was used. The charcoal (BAU, Russia) was used as a sorbent. Desorption of amino acids and carbohydrates were performed by means of 0.1 N HCl. For the desorption of polyphenols, the 90% acetone water solution was used. The elution of FA fraction was performed with 0.1 N NaOH solution [23, 24]. The obtained alkalic solution of FA for the purification was passed through a cation-exchanger (KU-2, Russia) and dried under the vacuum until the constant mass was obtained. Then, model solutions of FA was prepared. The required pH was adjusted by the addition of hydrochloric acid or sodium hydroxide.

0.1 mL old suspension of nickel hydroxide and increasing quantity of standard solution of FA were placed in 15 mL capacity fluroplastic cylinders. pH = 8.0, μ = 0.01 (KNO_3), V = 10 mL. Solution containing the sediment was placed in thermostat at 25 °C. Then, it was stirred in a mechanical mixer for 60 h (until the balance was achieved) and then suspension was filtered through the membrane filters (Sinpor N6, diameter of phores 400 nm). In filtrates, nickel was measured by atomic absorption spectrophotometer (Perkin almer 200).

3. Results and Discussion

The data (Table 1) show that in line with the increase of concentration of FA in the solution, the concentration of nickel increases for several times as well due to formation of fulvic complex.

During the calculation of molar concentrations of FA, the fact, that FA form associates in water solutions, which value of average molecular mass (M_W) depends on pH: M_W = 1,350pH-4,540 (pH ≥ 4) [24] was taken into consideration.

In the diluted water solutions the forms, of nickel in % were calculated through Eqs. (1)-(3).

$$Ni^{2+}\% = 100/(1+\beta_{NiOH}[OH^-]+\beta_{Ni(OH)_2^0}[OH^-]^2) \quad (1)$$

$$NiOH^+\% = \beta_{NiOH}[OH^-]100/(1+\beta_{NiOH}[OH^-]+\beta_{Ni(OH)_2^0}[OH^-]^2) \quad (2)$$

$$Ni(OH)_2^0\% = \beta_{Ni(OH)_2^0}[OH^-]^2100/(1+\beta_{NiOH}[OH^-]+\beta_{Ni(OH)_2^0}[OH^-]^2) \quad (3)$$

$\beta_{NiOH} = 5.5 \times 10^4$ $\beta_{Ni(OH)_2^0} = 5.5 \times 10^{14}$ [25]

As the calculations show ((Fig. 1), in balanced solutions at pH = 8, practically the whole Ni(II) is in the form of nickel dihydroxocomplex $Ni(OH)_2^0$.

So the complex formation reaction (pH = 8.0) may be written in Eq. (4).

$$Ni(OH)_2^0 + mFA^{2-} \leftrightarrows Ni(OH)_2FA^{2m-} \quad (4)$$

In Ref. [26], the method of calculation of the stability constant of fulvic complexes was described in detail, so in this paper the item will be discussed briefly. The numeral meaning (m) of the stechiometral coefficient or the ligands number in the inner coordination

Table 1 The data (mol/L) required for calculating stability constants of nickel fulvic complex (pH = 8.0; μ = 0.01 (KNO_3), t = 25 °C, M_w (FA) = 6,260, C'_{Ni} = 7.9 × 10^{-6}).

C_{FA}	C_{Ni}-C'_{Ni}	$[FA^{2-}]$	$\beta = [C_{Ni}-C'_{Ni}]/\{[C'_{Ni}][FA^{2-}]\}$
6.2 × 10^{-5}	5.0 × 10^{-5}	1.2 × 10^{-5}	5.3 × 10^5
7.2 × 10^{-5}	5.9 × 10^{-5}	1.3 × 10^{-5}	5.8 × 10^5
9.3 × 10^{-5}	7.4 × 10^{-5}	1.9 × 10^{-5}	4.9 × 10^5
1.1 × 10^{-4}	8.9 × 10^{-5}	2.1 × 10^{-5}	5.4 × 10^5
1.2 × 10^{-4}	9.7 × 10^{-5}	2.3 × 10^{-5}	5.3 × 10^5
1.7 × 10^{-4}	13.8 × 10^{-5}	3.2 × 10^{-5}	5.5 × 10^5
2.0 × 10^{-4}	16.0 × 10^{-5}	4.0 × 10^{-5}	5.1 × 10^5

$\beta Ni(OH)_2FA^{2-} = 5.3 \times 10^5$.

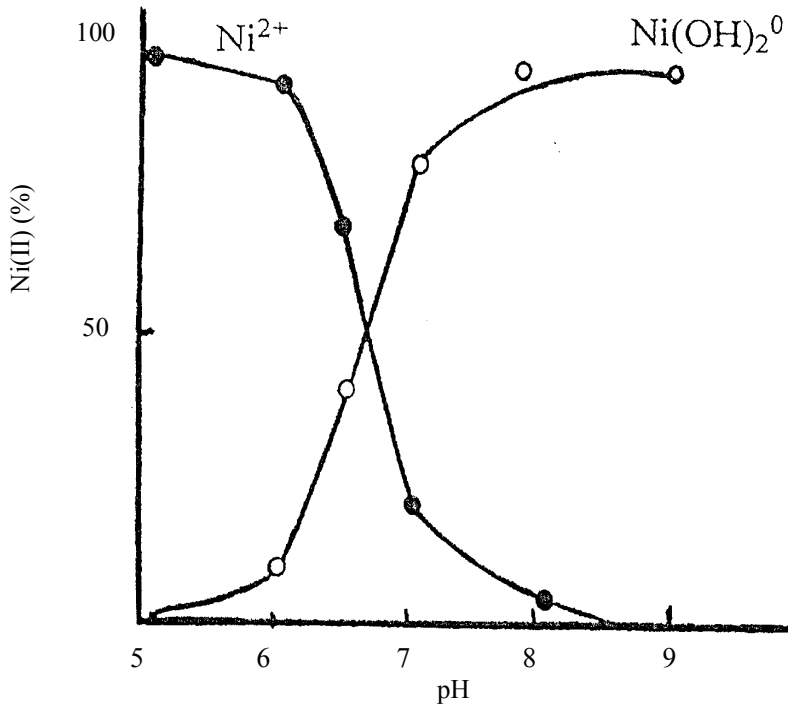


Fig. 1 The distribution diagram of the forms of Ni(II) in diluted water solutions (in %).

Table 2 The data to calculate the meaning of *m* by the least square method.

x_i lg C_{FA}	y_i lg $[C_{Ni} - C'_{Ni}]$	x_i^2	$x_i y_i$
-4.2076	-4.3010	17.7038	18.0968
-4.1426	-4.2291	17.1611	17.5194
-4.0315	-4.1307	16.2529	16.6529
-3. 9586	-4.0506	15.6705	16.0347
-3.9208	-4.0132	15.3726	15.7349
-3.7695	-3.8601	14.2091	14.5506
-3.6989	-3.7958	13.6818	14.0402

Σx_i = -27.7295, Σy_i = -28.3805, Σx_i^2 = 110.0518, $\Sigma x_i\, y_i$ = 112.6295, $(\Sigma x_i)^2$ = 768.9251, $\Sigma x_i\, \Sigma y_i$ = 786.9770, m = 0.99.

sphere of complex equals to tangens of tilt angle of straight line built in coordinates:

$$\text{lg } [C_{Ni}\text{-}C'_{Ni}] \text{ —— } m\text{lg } C_{FA} \quad (5)$$

where, C'_{Ni} is the initial concentration of nickel, C_{Ni} is the final concentration of nickel, received after formation of complex and C_{FA} is concentration of FA in solution.

To calculate the exact value of tangens, tilt angle of straight line was used the least square method (Table 2):

$$m = \text{tg}\alpha = (n\Sigma x_i y_i - \Sigma x_i \Sigma y_i)/\,(n\Sigma x_i^2 - (\Sigma x_i)^2) \quad (6)$$

$$x_i = \text{lg} C_{FA} \text{ and } y_i = \text{lg}[C_{Ni} - C'_{Ni}]$$

After the calculations we obtained the numeral meaning of stechiometral coefficient (m), which equals to 0.99, which demonstrates that complex with the structure 1:1 dominates in the $Ni(OH)_2$-H_2O-FA system. Therefore, the formula for calculating the stability constant can be expressed in the following way:

$$\beta = [C_{Ni}\text{-}C'_{Ni}]/\{[C'_{Ni}][FA^{2-}]\} \quad (7)$$

where,

$$[FA^{2-}] = C_{FA}\text{-}[C_{Ni}\text{-}C'_{Ni}] \quad (8)$$

Taking into account the average molecular mass of associate at pH = 8, (M_w = 1,350 pH-4,540 [24]), the average stability constant of nickel fulvic complex

was calculated on the basis of experimental data (Table 1).

So, in $Ni(OH)_2$ (solid)-$Ni(OH)_2^o$ (solution)-FA^{2-}-H_2O system at pH = 8 dominates the nickel dyhydroxofulvic complex with the structure 1:1, $[Ni(OH)_2FA]^{2-}$, which average stability constant is: $\beta Ni(OH)_2FA^{2-} = 5.3 \times 10^5$.

4. Conclusions

So, in $Ni(OH)_2$ (solid)-$Ni(OH)_2^o$ (solution)-FA^{2-}-H_2O system at pH = 8 dominates the nickel dyhydroxofulvic complex with the structure 1:1, $[Ni(OH)_2FA]^{2-}$, which average stability constant is: $\beta Ni(OH)_2FA^{2-} = 5.3 \times 10^5$.

References

[1] Zhang, H. In-Situ Speciation of Ni and Zn in Freshwaters: Comparison between DGT Measurements and Speciation Models. *Environmental Science and Technology* **2004,** *38,* 1421-1427.

[2] Town, R. M.; Van Leeuwen, H. P.; Buffle, J. Chemodynamics of Soft Nanoparticulate Complexes: Cu(II) and Ni(II) Complexes with FA and Aquatic Humic Acids. *Environmental Science and Technology* **2012,** *46,* 10487-10498.

[3] Liping, W.; Willem, H.; Van, R.; Tjisse, H. Cu^{2+} and Ca^{2+} Adsorption to Goethite in the Presence of Fulvic Acids. *Geochimica et Cosmochimica Acta* **2008,** *72,* 5857-5870.

[4] Esterves, S. J. C. G.;Machado, A. S. C.; Pinto, S. S. D. Fluorescence Quenching of Anthropogenic FA by Cu(II), Fe(III) and UO_2^{2+}. *Talanta* **1998,** *45,* 1155-1165.

[5] Shizuko, H. Stability Constants for the Complexes of Transition-Metal Ions with Fulvic and Humic Acids in Sediments Measured by Gel-Ffiltration. *Talanta* **1981,** *28,* 809-815.

[6] Buckau, G.; Kim, J. I.; Klenze, R.; Rhee, D. S.; Wimmer, H. A Comparative Spectroscopic Study of the Fulvate Complexation of Trivalent Transuranium Ions. *Radiochim. Acta* **1992,** *57,* 105-111.

[7] McCarthy, J. F.; Czervinski, K. R.; Sanford, W. E.; Jardine, P. M.; Marsh, J. D. Mobilization of Transuranic Radionuclides from Disposal Trenches by Natural Organic Matter. *J. of Contaminant Hydrology* **1998,** *30,* 49-77.

[8] Claret, F.; Schaver, T.; Rabung, T.; Wolf, M.; Bauer, A.; Buckau, G. Differences in Properties and Cm(III) Complexation Behavior of Iisolated Humic and Fulvic Acid Derived from Opalinus Clay and Callovo-Oxfordian Argillite. *Applied Geochemistry* **2005,** *20,* 1158-1168.

[9] Glaus, M. A.; Hummel, W.; Van Loon, L. R. Trace Metal-Humate Interaction.I. Experimental Determination of Conditional Stability Constants. *Applied Geochemistry* **2000,** *15,* 953-973.

[10] Cheam, V.; Gamble, D. S. Metal-Fulvic Acid Chelation Equilibrium in Equeous $NaNO_3$ Solution Hg(II), Cd(II) and Cu(II) Fulvate Complexes. *Can. J. Soil Science*. **1974,** *54,* 413-417.

[11] Makharadze, G. A.; Supatashvili, G. D.; Varshal, G. M. The Research of the Forms of Copper in Surface Waters. *Hydrochemical Materials* **1988,** *103,* 3-16.

[12] Varshal, G. M.; Velyukhanova, T. K.; Koshcheeva, I. Y.; Dorofeeva, V. A.; Buachidze, N. S.; Kasimova, O. G.; et al. Investigation of Chemical Forms of Elements in Surface Water. *Journal of Analytical Chemistry* **1983,** *38,* 1590-1599.

[13] Buffle, J.; Deladoey, P.; Greter, F. L.; Haerdi, W. Study of the Complex Formation of Copper(II) by Humic and Fulvic Substances. *Analitica Chimica Acta* **1980,** *116,* 255-274.

[14] Joris, W. J.; Van, S.; Dan, B. K.; Jon, P. G. Acid-Base and Copper-Binding Properties of Three Organic Matter Fractions Isolated from a Forest Floor Soil Solution. *Geochimica et Cosmochimica acta* **2010,** *74,* 1391-1406.

[15] Rey-Castro, C.; Mongin, S.; Huidobro, C.; David, C.; Salvador, J.; Garces, J.; et al. Effective Affinity Distribution for the Binding of Metal Ions to a Generic Fulvic Acid in Natural Waters. *Environmental Science and Technology* **2009,** *43,* 7184-7191.

[16] Orsetti, S.; Marco-Brown, J. L.; Andrade, E. M.; Molina, F. V. Pb(II) Binding to Humic Substances: An Equilibrium and Spectroscopic Study. *Environmental Science and Technology* **2013,** *47,* 8325-8333.

[17] Lenoir, T.; Manceau, A. Number of Independent Parameters in the Potentiometric Titration of Humic Substances. *Langmuir* **2010,** *26,* 3998-4003.

[18] Makharadze, G. A.; Supatashvili, G. D.; Varshal, G. M. Humic Acids in Surface Waters of Georgia. *Hydrochemical Materials* **1989,** *106,* 22-30.

[19] Schnitzer, M.; Hansen, E. H. An Evaluation of Methods for the Determination of Stability Constants of Metal-Fulvic Acid Complexes. *Soil Science* **1970,** *109,* 333-340.

[20] Schnitzer, M.; Skinner, S. I. M. Stability Constants of Pb, Ni, Mn, Co, Ca and Mg Fulvic Acid Complexes. *Soil Science* **1967,** *103,* 247-252.

[21] Mantoura, R. F. C.; Dixon, A.; Rilly, J. P. The

Speciation of Trace Metals with Humic Compounds in Natural Waters. *Thalassia Jugoslavica* **1978,** *14,* 127-145.

[22] Goncharova, T. O.; Kolosov, I. V.; Kaplin, B. T. Hydrolysis and Complexation of Nickel Ions in Solutions of FA. *Hydrochemical Materials* **1978,** *71,* 64-72.

[23] Varshal, G. M.; Kosheeva, I. Y.; Sirotkina, I. S.; Velukhanova, T. K.; Intskirveli, L. N.; Zamokina, N. C. The Study of Organic Substances in Surface Waters and Their Interaction with Metal Ions. *Geochemistry* **1979,** *4,* 598-607.

[24] Revia, R.; Makharadze, G. Cloud-Point Preconcentration of Fulvic and Humic Acids. *Talanta* **1999,** *48,* 409-413.

[25] Nazarenko, V. A.; Antonovich, V. N.; Nevskaya, E. M. *The Hydrolise of Metal Ions in Diluted Solutions;* Moscow, 1979, p 190.

[26] Makharadze, G.; Makharadze, T. Method of Calculation of Stability Constants of Fulvic Complexes on the Example of Copper. *Journal of Chemistry and Chemical Engineering* **2014,** *8,* 108-111.

J. Chem. Chem. Eng. 8 (2014) 349-357

Microwave Preparation of SiO_2-B_2O_3-Na_2O-K_2O-CaO-Fe_2O_3-TiO_2 Glass System

Ashis Kumar Mandal[1*], Prasanta Kumar Sinha[1], Santanu Sen[1], Sitendu Mondal[1], Chandan Guha[2] and Ranjan Sen[1]

1. CSIR-Central Glass and Ceramic Research Institute, Kolkata 700032, India

2. Department of Chemical Engineering, Jadavpur Unirversity, Kolkata 700032, India

Received: January 21, 2014 / Accepted: February 17, 2014 / Published: April 25, 2014.

Abstract: This study reports preparation of glass composition (54.50 wt.%) SiO_2, (10.80 wt.%) B_2O_3, (14.20 wt.%) Na_2O, (1.20 wt.%) K_2O, (6.00 wt.%) CaO, (4.00 wt.%) Fe_2O_3 and (9.30 wt.%) TiO_2 by melt quenching method using direct microwave heating and conventional resistive heating. Study of dielectric loss factor of the glass as function of temperature illustrated increasing loss factor above 370 ^oC, 550 ^oC, 650 ^oC and 900 ^oC, indicating enhanced microwave absorption by the glass at above these temperatures. Chemical analysis results of both the glasses depicted more volatilization loss of volatile ingredients in conventional heating. The study of chemical durability was performed from leachate analysis describing less leaching of Na_2O, K_2O and other constituents from glass melted in microwave furnace. Glass transition temperatures (T_g) were found to be 576.3 ^oC and 569.5 ^oC for glass melted in conventional and microwave heating route, respectively. Laboratory experiment of glass melting utilizing microwave energy as an alternate heating source demonstrated 70%-75% electrical power saving.

Key words: Microwave heating, energy efficient glass melting, dielectric constant, loss factor, chemical durability.

1. Introduction

Microwave heating has find its application in material processing mainly because of rapid volumetric heating, flexibility in furnace operation (i.e., switching off at maximum temperature) and comfortable working environment owing to only sample heating keeping the cavity cold, substantial reduction in energy consumption, improved mechanical properties and many others [1, 2]. The difficulty of glass melting using microwave energy is mainly due to low dielectric loss factor of major raw material at room temperature making the material as microwave transparent material. However, the loss factor of glass increases with temperature enabling microwave coupling with materials above "critical temperature" and thereby generating heat within it [3]. Hence, glass batches are heated conventionally above ~ 500 ^oC before direct microwave heating for melting [4]. Feasibility study of glass melting by microwave heating has been reported in different glass systems such as, niobium phosphate [5], alumino-phosphate [6], molybdo-phosphate and tungsto-phosphate [7], iron phosphate [8] and inorganic glasses [9] etc.. However, most of researches were carried out in kitchen microwave oven in which proper control of process parameter could not be done.

Present study reports preparation of glass composition (54.47 wt.%) SiO_2, (10.81 wt.%) B_2O_3, (14.16 wt.%) Na_2O, (1.19 wt.%) K_2O, (6.02 wt.%) CaO, (4.05 wt.%) Fe_2O_3 and (9.30 wt.%) TiO_2 using microwave heating. Some of the physical and optical properties were measured and compared with the glass melted from identical batch in resistive heating. The study of power consumption in microwave heating and in conventional resistive heating were presented and discussed.

[*]**Corresponding author:** Ashis Kumar Mandal, B.E (Chemical), research field: microwave melting of glass. E-mail: ashis@cgcri.res.in.

2. Experiments

2.1 Conventional Melting of Glass

The glass was prepared using high purity raw materials like quartz, H_3BO_3, Na_2CO_3, K_2CO_3, $CaCO_3$, Fe_2O_3 and TiO_2. Properly mixed raw materials for 60 g glass was uniaxially pressed to form pellet in a hydraulically operated pellet press and the pellet was placed in a 50 mL alumina crucible which was subjected to heating in electrical resistive furnace (raising hearth furnace from Bysakh & Co., India; heating zone: 230 m × 230 m × 300 m). B-type thermocouple was fixed with the furnace to monitor the temperature. Power consumption, temperature and time were recorded to generate T-t-P (temperature-time-power) profile in resistive heating. Melting was carried out at 1,300 ^oC for 2 h with a heat up rate 4 ^oC/min and manual stirring was adopted twice with 30 min interval using silica rod to yield homogeneous glass prior to pouring into a preheated steel mold. The hot glass block was annealed in a muffle furnace at 560 ^oC, below glass transition temperatures T_g, for 2 h followed by controlled cooling to room temperature. The annealed glass was termed as SBNRH (glass prepared in resistive heating).

2.2 Microwave Melting of Glass

Identical pellet of glass batch for 60 g glass was placed inside an alumina crucible insulated by microwave transparent cage insulating box and placed inside a 3 kW, 2.45 GHz, multimode microwave furnace (from M/S Enerzi Microwave Systems Pvt. Ltd., India, microwave cavity size 367 mm × 349 mm × 386 mm). An opening of 20 mm diameter was made at top cover of insulation box to allow temperature monitoring through a non contact IR (Infrared) pyrometer (260-1,800 °C). The temperature measurement accuracy and repeatability was ± 0.3% of the measured value + 1 °C with adjustable emissivity (ε: 0.1-1.0). MW power (Microwave output power) and temperature were recorded by DAQSOFT software in a separate computer. A separate energy meter (kW-h meter) was also connected to the input of the electrical circuit to monitor mainly consumption of instant electrical power and total power consumption for overall system including utilities. An integrated closed loop water cooling system was used to cool the microwave cavity, magnetron housing (model: 2M265-M12WJ-Panasonic) and others. The melting of the studied glass was carried out in air atmosphere. Fumes, hot gas generated during melting of batch was exhausted out intermittently by a diaphragm pump. Glass melting was carried out at 1,350 ^oC for 1 h. Molten glass was cast into a preheated mold and annealed as explained earlier section. The annealed glass was termed as SBNM (glass melted in microwave furnace).

2.3 Characterization

XRD (X-ray diffraction) analysis was performed on 94 X'Pert, PANalytical using Ni-filtered CuKα radiation with wavelength of 1.5406 Å to confirm the sample amorphous characteristic. The scanning was carried out in the range of 10^o-85^o with a step size of 0.05 ^{o}/min.

ICP-AES (inductively coupled plasma atomic emission spectroscopy) (model: Spectro Ciros Vision, Germany) was used for chemical analysis of Fe_2O_3, TiO_2, Na_2O and K_2O; volumetric titrimetry for SiO_2 and B_2O_3 and complexiometry for Al_2O_3 and CaO. Chemical durability was evaluated from leachate analysis by ICP-AES. The bulk glasses were pulverized and sheaved (within mesh No. 40-60). Then, the glasses were washed in acetone and dried at 110 ^oC for 2 h. The washed and dried glasses were cooled down inside a desiccator. Each sample of weight 5 g was taken into a Teflon beaker with 100 mL deionised water and kept at 90 ^oC for 14 days. During the treatment in the above mentioned condition, some of the constituents of the glasses were leached out into the water and these were measured by ICP-AES

(model: Spectro Ciros Vision, Germany). The relative standard deviation of three successive measurements for all the constituents was in the range from 0.59%-0.74%.

Dielectric loss factor and dielectric constant were measured at 2.45 GHz as a function of temperature (up to 1,000 ^{o}C). A cylindrical cavity, a vector network analyzer, a microwave amplifier, an infrared pyrometer and a computer were employed to carry out the measurement. The cylindrical rod shape sample was placed inside a quartz tube containers and microwave are applied for heating and measuring simultaneously inside a microwave cavity [10]. Typical uncertainty of these measurements is around 2% in real part and 5% in imaginary part. For high-temperatures (around 1,000 ºC), the uncertainty can increase to 10% because the dimensions of the sample change when the materials are melting. The dimension of the sample is a variable used in the dielectric calculations.

The T_g was identified by DSC (differential scanning calorimeter) (NETZSCH STA 449F3) at a heating rate of 10 K/min in flowing nitrogen with an accuracy ± 1 ^{o}C. The refractive indices of glass samples prepared by both methods were measured at five different wavelengths (473 nm, 532 nm, 633 nm, 1,064 nm and 1,552 nm) on Prism Coupler (Metricon Model-2010, NJ, USA) fitted with five different lasers as illuminating sources. Three measurements were recorded for each sample and the standard deviation was reported as error of measurement (± 0.0004).

FTIR (Fourier transform infrared spectroscopy) measurements of both the glasses were performed on a FTIR spectrophotometer (model: 1615, Perkin Elmer Corporation, USA) with a spectral resolution of 4 cm^{-1} over a spectral range of 400-2,000 cm^{-1} to see the structural changes, if any.

Longitudinal velocity (V_L) and shear velocity (V_T) were measured by the ultrasonic pulse-echo method, using Ultrasonic Flaw Detector (model No. EPOCH 1000, Blue Star). An ultrasonic pulse of 20 MHz frequency employed through longitudinal and shear transducers. The Poisson's ratio (v), Young's (E), shear (G) and bulk (K) modulus were calculated applying the measured bulk density (ρ), V_L, and V_T in Eqs. (1)-(4) [11, 12].

$$v = 0.5\ \frac{(V_L^2 - 2V_T^2)}{(V_L^2 - V_T^2)} \quad (1)$$

$$E = \rho \cdot \left(\frac{3V_T^2\, V_L^2 - 4V_T^4}{V_L^2 - V_T^2}\right) \quad (2)$$

$$G = \rho \cdot V_T^2 \quad (3)$$

$$K = \frac{\rho}{3} \cdot (3V_L^2 - 4V_T^2) \quad (4)$$

2.4 T-t-P Profile

Temperature and variation of MW power with time for melting of 60 g studied glass using direct microwave heating was presented in Fig. 1. MW power was manually controlled to see the microwave interaction with sample. A rapid temperature increase was observed after 30 min with slow increase of MW power at 0.6 kW. A sharp increase of T-t profile at 900 ^{o}C was seen in the Fig. 1, predicting higher dielectric loss factor of the glass above this temperature. Fig. 1 also depicted maximum MW power ~ 0.60 kW during the melting till 1,350 ^{o}C. However, efficiency of microwave generator was within the range 55%-65% of input electrical power. Thus maximum input electrical power would be ~ 1 kW during the melting of studied glass in microwave furnace. Fig. 1 further illustrated that total time was within 3 h during melting including 30 min initial start up time prior to initiation of heating. Further, operation flexibility in microwave furnace enables easy switch off at high temperature reducing further time and energy.

Temperature and variation of input power with time for the studied glass melted in the resistive heating furnace was displayed in Fig. 2. Heating rate in conventional furnace was restricted to 4 ^{o}C/min to protect the life of heating element and refractory lining inside the furnace. Soaking time at maximum temperature in conventional melting was almost

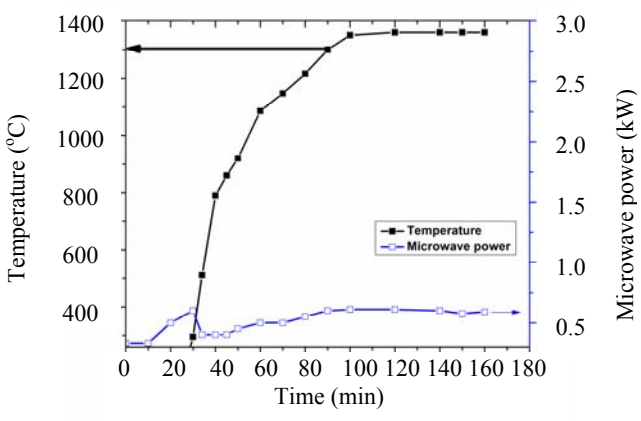


Fig. 1 Temperature and variation of microwave output power with time during microwave melting of glass.

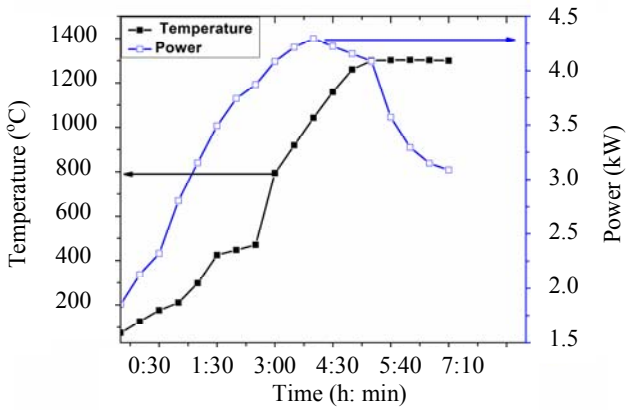


Fig. 2 Temperature and electrical power profile with time for conventional heating in resistance heating furnace.

double the time needed for microwave processing resulting total melting time was around ~ 7 h. Fig. 2 also illustrated that maximum instant electrical power in electrical raising hearth furnace was ~ 4.00 kW almost four times than that of microwave heating.

A comparison of total power consumption for both the heating method using above furnaces for the equal amount of studied glass was illustrated in Fig. 3. It was clearly seen from the Fig. 4 that the total power consumption was ~ 26 kWh in the conventional laboratory glass melting process using above raising hearth furnace. Overall melting time was found to be 7 h[1] in conventional glass melting process. In microwave melting, the total power consumption was recorded ~ 6 kWh incorporating additional power load for utilities, i.e., chilled water system, fume exhaust system. However, total power requirement could be further minimised by changing the design of the microwave furnace using air-cooled magnetron and by placing a small amount of microwave susceptor like SiC around the crucible, which preheats the raw material before directly absorbing microwave radiation. At higher temperature, microwaves interact with the entire volume of glass at the same rate causing volumetric heating, which further reduces holding time at maximum temperature in glass melting compared to conventional glass melting. Since glass melting is a huge energy consuming process, it would be of great relief if alternate method of producing glass reduces energy requirement substantially. In this context, microwave glass melting could be a potential energy efficient technology saving a significant amount of electrical energy and time, needed for present glass making. Further, microwave melting of glass would eventually contribute to the cleaner environment. However, the difficulty remains in microwave glass melting with proper melting crucible and design of suitable microwave equipment for larger scale glass melting.

3. Results and Discussion

3.1 Microwave Absorption of Material

Microwave heating is the result of absorption of electromagnetic energy by the material exposed to the microwave field distributed within a reflective cavity. It is based on the power absorbed per unit volume (Eq. (5) [13, 14]).

$$P = \sigma \left| E^2 \right| = 2\pi f \varepsilon_0 \varepsilon'_r \tan\delta E^2 \quad (5)$$

where, E is the magnitude of the internal electric field, ε_o is the permittivity of free space, f is the microwave frequency, σ is the total effective conductivity, ε'_r is the relative dielectric constant, and tanδ is the energy loss required to store a given quantity of energy, ε''_{eff}

[1]Furnace cooling down to room temperature was not considered.

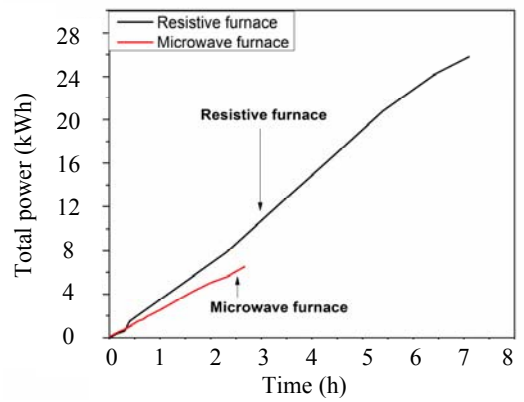


Fig. 3 Total power consumption profile with temperature; for resistance heating and for microwave heating.

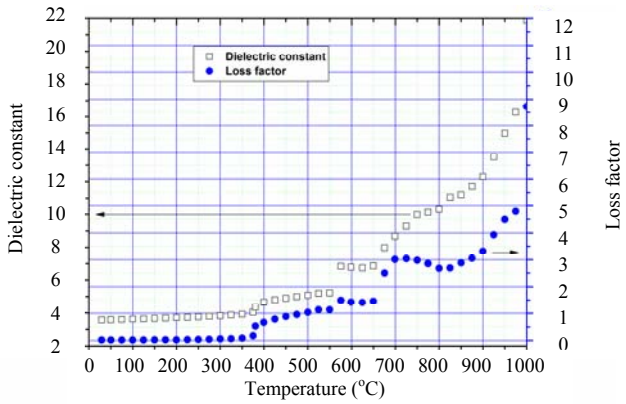


Fig. 4 Dielectric constant and loss factor for the studied glass was measured around 2.45 GHz as a function of temperature up to 1,000 °C.

(= $\varepsilon'_r \cdot \tan\delta$) is the relative effective dielectric loss factor. It is clearly seen from the above Eq. (5) that the dielectric properties (ε_o, ε'_r and $\tan\delta$) assume a significant role in determining the extent of power absorbed by a material.

Fig. 4 portrayed the dielectric constant and dielectric loss factor as function of temperature (up to 1,000 °C) for this glass. Dielectric loss factor, one of the important parameters, indicates the degree of microwave absorption by the material to generate heating within it for a fixed frequency (2.45 GHz) and a given electrical field within the material. The Fig. 4 depicted that loss factor increased at ~ 370 °C, ~ 560 °C, ~ 650 °C and ~ 900 °C suggesting enhance microwave absorption and heating of glass at these temperatures. Sharp increase of loss factor 0 at around 900 °C corroborated the rapid heating observed from the T-t profile in microwave heating in Fig. 1. However, microwave interaction with batch material at lower temperature was found different due to the presence of different raw material (i.e., carbonate, H_3BO_3).

3.2 Comparison of Properties

Fig. 5 displayed photograph of 1mm thick polished glass (15 mm × 20 mm) melted in a conventional resistance-heating (SBNRH) and in microwave heating (SBNM). In Fig. 5, improved homogeneity of SBNM was seen, apparently compared to SBNRH. Though the SBNM was prepared without employing any mechanical stirring, improved homogeneity was due to the result of microwave induced "self-stirring" effect [15].

The XRD patterns for the SBNRH and SBNM samples, shown in Fig. 6, depicting identical broad humps confirmed the amorphous nature of the samples. The absence of sharp Bragg peak in the XRD profile of SBNM, similar to that of SBNRH, confirmed no unmelted crystalline phase left within the glass melted using microwave.

Chemical analysis results for SBNM and SBNRH samples were listed in Table 1. B_2O_3 and Na_2O were found less in SBNRH glass illustrating higher evaporation loss of these ingredients in conventional melting. Al_2O_3 was found 6.47% in SBNRH and 1.56% in SBNM sample. In conventional heating, heat travels from the heating element to the material by means of

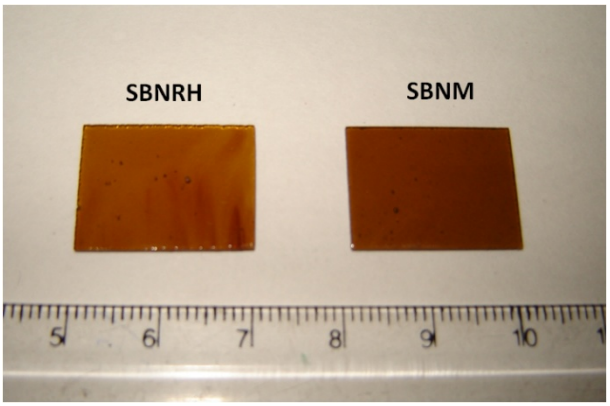


Fig. 5 Photographs of polished SBNRH and SBNM glass samples.

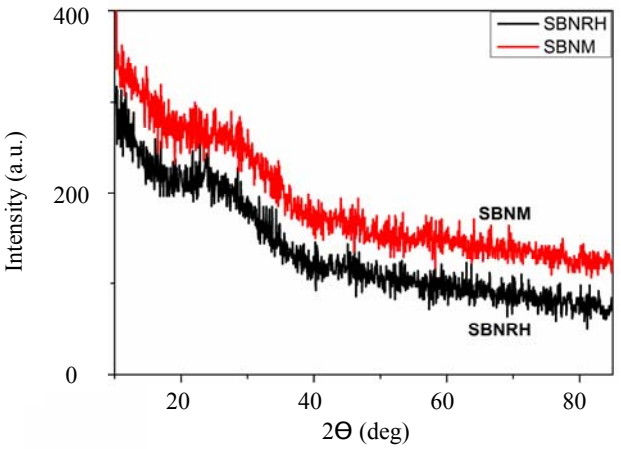


Fig. 6 XRD curves for SBNM and SBNRH samples.

radiation, conduction, convection mechanism and thus temperature of the crucible wall remains higher than the molten glass. This higher wall temperature together with higher melting time contributed higher leaching of Al_2O_3 into the molten glass in conventional melting. In microwave heating, heat generates within the material internally resulting in volumetric heating within the glass without heating the alumina crucible owing to its low dielectric loss factor. Due to this rapid internal heating, temperature gradient in microwave heating exists in the reverse direction than that of conventional heating resulting less temperature in crucible wall and in the top surface of molten glass. Thus, less crucible wall temperature along with less melting time favour low contamination of alumina into the glass melt in microwave heating. This reverse temperature gradient also contributes less evaporation of volatile ingredients of glass in microwave heating. However, slightly higher melting temperature is needed in case of microwave melting due to less surface temperature of molten glass.

The chemical durability of both the glasses was evaluated from leachate analysis by Inductively Coupled Plasma-Atomic Emission Spectroscopy. The results, as shown in the Table 2, illustrated higher concentration of Al_2O_3, CaO, Fe_2O_3, TiO_2, Na_2O and K_2O, leached out into water from the SBNRH sample signifying higher leaching rate of above constituents from SBNRH sample. This indicated improved chemical durability of glass was prepared in microwave heating. This may be explained that more evaporation of glass former, i.e., SiO_2 and B_2O_3 the main building block in glass, weaken the glass structure in conventional heating method.

Fig. 7 exemplified DSC thermograph for both the glasses SBNRH and SBNM. T_g was identified 569.5 ^oC and 576.3 ^oC for SBNM and SBNRH samples, respectively. T_g value for SBNM was observed less due to difference in the composition of the glasses resulting from low loss of volatile constituents of glass. Higher presence of Al_2O_3 in SBNRH owing to leaching from crucible wall, also contributed the higher T_g in SBNRH.

The some of the physical, optical and elastic properties of SBNM and SBNRH were listed in Table 3. Optical properties for SBNRH and SBNM samples were calculated from their measured refractive indices using relevant expressions and were presented in Table 2.

Fig. 8 portrayed dispersion curves, obtained by fitting the measured refractive indices with the

Table 1 Chemical analysis results for SBNRH and SBNM samples.

Composition (wt.%)	SBNRH	SBNM
SiO_2	56.36 (± 0.08)	58.88 (± 0.08)
B_2O_3	7.92 (± 0.04)	9.13 (± 0.04)
Na_2O	10.92 (± 0.04)	12.02 (± 0.04)
K_2O	0.68 (± 0.03)	0.82 (± 0.03)
CaO	4.82 (± 0.04)	5.03 (± 0.04)
Fe_2O_3	3.65 (± 0.03)	3.65 (± 0.03)
TiO_2	8.91 (± 0.04)	8.57 (± 0.04)
Al_2O_3	6.47 (± 0.03)	1.56 (± 0.03)

Table 2 Glass transition temperature, optical properties and elastic properties for SBNRH and SBNM are presented.

Property	SBNRH	SBNM
Measured Refractive index (n) at		
473 nm (± 0.0004)	1.5969	1.6006
532 nm (± 0.0004)	1.5904	1.594
633 nm (± 0.0004)	1.5827	1.586
1,064 nm (± 0.0004)	1.5691	1.573
1,552 nm (± 0.0004)	1.5624	1.5656
Estimated Refractive indices at		
$n_{d\text{-}587.6}$ (± 0.0005)	1.5860	1.5895
$n_{F\text{-}486.1}$ (± 0.0005)	1.5953	1.5988
$n_{C\text{-}656.3}$ (± 0.0005)	1.5814	1.5848
$n_{d\text{-}1}$	0.586	0.59
Mean dispersion (n_F-n_C)	0.014	0.014
Abbe No.	42.16	42.10
Reflection loss (%)	5.17	5.13
Elastic properties		
Longitudinal velocity (m/s)	5,776	5,813
Shear velocity (m/s)	3,448	3,505
Young's modulus (E, GPa)	78.90	80.20
The Poisson's ratio (v)	0.219	0.235
Shear modulus (G, GPa)	90.07	93.76
Bulk modulus (K, GPa)	46.90	50.46
Glass transition temperature, T_g (± 1 °C)	576.3	569.5

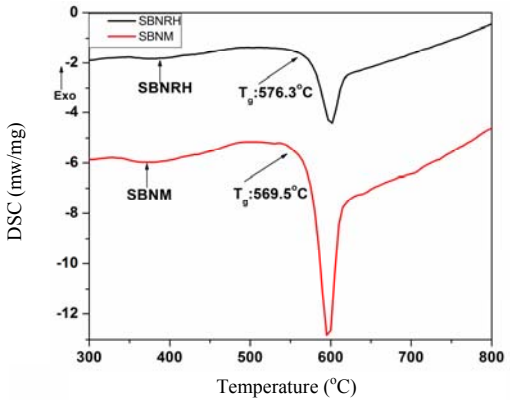


Fig. 7 DSC thermographs for SBNRH and SBNM sample.

Cauchy Eq. (6). The refractive indices at standard wavelengths n_d (at 587.6 nm), n_F (at 486.1 nm) and n_C (at 656.3 nm) were estimated from the curve.

$$n(\lambda) = A + \frac{B}{\lambda^2} + \frac{C}{\lambda^2} + \cdots \quad (6)$$

where, n is refractive index at wavelength λ. The Abbe number V of a material is defined as Eq. (7):

$$V = \frac{(n_d - 1)}{(n_F - n_c)} \quad (7)$$

where, n_d, n_F and n_C are the refractive indices of the samples at the wavelengths 587.6 nm, 486.1 nm and 656.3 nm, respectively. Abbe number was calculated and found very similar for both SBNRH and SBNM as 42.16 and 42.10, respectively. Mean diffraction and reflection loss for SBNRH and SBNM samples were also found similar.

Elastic properties like v, Young's (E)-shear (G)-bulk (K) modulus were calculated and listed in Table 1. The identical or slightly higher value of these properties in the microwave prepared glass confirmed that similar glass or slightly improved property of glass could be prepared in microwave heating.

The FTIR reflectance spectra of samples SBNRH and SBNM were presented in Fig. 9. Both the spectra of these glasses consisted of similar broad and sharp bands in different regions (400-2,000 cm^{-1}) confirming identical structure. FTIR spectra for both glasses showed the presence of silicate peak centered at 1,022 cm^{-1} and Si-O-Si bend at around 443 cm^{-1} [16]. The bands at around 1,020 cm^{-1} peak were attributed

Table 3 The concentration (in ppm) of different constituents present in deionised water after 14 days insertion of SBNRH and SBNM glasses at 90 ^oC.

Leachate from samples	Al_2O_3	CaO	Fe_2O_3	TiO_2	Na_2O	K_2O
SBNM	31	19	10	15	131	21
SBNRH	59	68	21	35	377	74

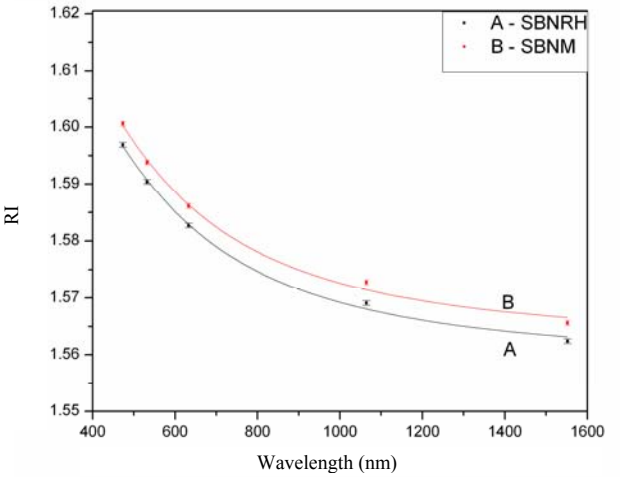


Fig. 8 RI vs. wavelength fitted by Cauchy curve fitting equation.

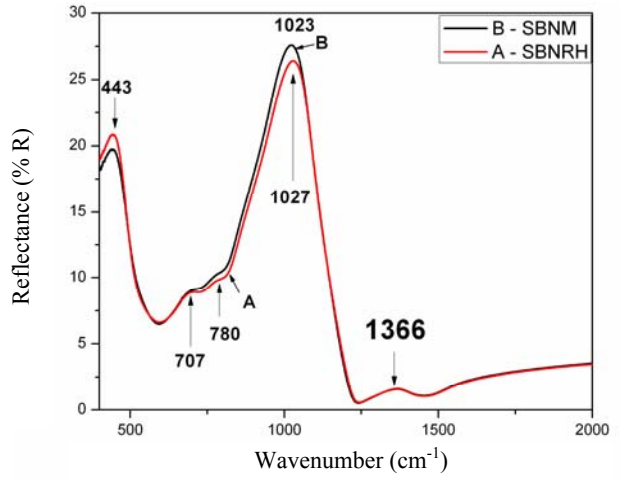


Fig. 9 FTIR reflectance spectra of studied samples in the wave number range 400-2,000 cm^{-1}.

to a stretching vibration of B-O-Si linkage [17]. The peak ~ 700 cm^{-1} was due to the bending of B-O-B linkages in the borate glassy network [18]. The boroxol ring appeared at 780 cm^{-1} [19]. The band around 1,360 cm^{-1} was assigned to B-O stretching vibration of trigonal [BO_3] unites [20, 21].

4. Conclusions

A glass containing SiO_2-B_2O_3-Na_2O-K_2O-CaO-Fe_2O_3-TiO_2 was successfully melted using direct microwave heating. Dielectric constant and loss factor as function temperature depicted increase of these properties at 370 ^oC, 550 ^oC, 650 ^oC and 900 ^oC, indicating enhanced microwave absorption with this glass composition above these temperatures. Similar glass was also prepared from identical batch in conventional resistive heating. Physical properties and structure of both the glasses were found similar. Glass melted in microwave heating was found closer chemical composition as prescribed in batch, improved chemical durability and lower glass transition temperature. Substantial less consumption of energy and shorter processing time was demonstrated in laboratory scale glass melting in microwave furnace. Thus, microwave processing of glass could be a potential method for reduction of energy consumption and time.

Acknowledgements

This work was funded by SupraInstitutional Network Project ESC0202 (GLASSFIB) of Council of Scientific and Industrial Research, India. Authors are thankful to the Director, CSIR-CGCRI for his kind support and encouragement to pursue this work. Authors also like to thank Mr. A. R. Molla, Dr. K. Biswas, Dr. K. Annapurna for their help in characterization of glass samples. Authors sincerely acknowledge the contribution of staff in GSTS, CSIR-CGCRI for their help as when required. Authors are thankful to Prof. J. M. Catala Civera for measurement of dielectric properties.

References

[1] Sutton, W. H. Microwave Processing of Ceramic Materials. *Cer. Bull.* **1987,** *68,* 376-386.

[2] Thostenson, E. T.; Chou, T. W. Microwave Processing:

Fundamentals and Applications. *Composites: Part A* **1999,** *30,* 1055-1071.

[3] Siligardi, C. D.; Arrigo, M. C.; Leonelli, C.; Pellacani, G. C.; Cross, T. E. Bulk Crystallization of Glasses Belonging to the Calcia-Zirconia-Silica System by Microwave Energy. *J. Am. Ceram. Soc.* **2000,** *83,* 1001-1003.

[4] Knox, M. P.; Copley, G. J. Use of Microwave Radiation for the Processing of Glass. *Glass Technol.* **1997,** *38,* 91-96.

[5] Ghussn, L.; Martinelli, J. L. A Novel Method to Produce Niobium Phosphate Glasses by Microwave Heating. *J Mater Sci.* **2004,** *39,* 1371-1376.

[6] Mandal, A. K.; Biswas, K.; Annapurna, K.; Guha, C.; Sen, R. Preparation of Alumino-Phosphate Glass by Microwave Radiation. *J. Mater. Res.* **2013,** *28(14),* 1955-1961.

[7] Chenu, S.; Rocherullè, J.; Lebullenger, R.; Merdrignac, O.; Chevire, F.; Tessier, F.; et al. Synthesis and Characterization of Tin Containing Molybdophosphate and Tungstophosphate Glasses. *J. Non-Cryst. Solids* **2010,** *356,* 87-92.

[8] Almeida, F. J. M.; Martinelli, J. R.; Partiti, C. S. M. Characterization of Iron Phosphate Glasses Prepared by Microwave Heating. *J. Non-Cryst. Solids* **2007,** *353,* 4783-4791.

[9] Vaidhyanathan, B.; Ganguli, M.; Rao, K. J. A Nobel Method of Preparation of Inorganic Glasses by Microwave Irradiation. *J. Solid State Chem.* **1994,** *113,* 448-450.

[10] Peñaranda-Foix, F. L.; Janezic, M. D.; Civera, J. M. C.; Canós, A. J. Full-Wave Analysis of Dielectric-Loaded Cylindrical Waveguides and Cavities Using a New Four-Port Ring Network. *IEEE T Microw. Theory* **2012,** *60,* 2730-2740.

[11] Varshneya, A. *Fundamentals of Inorganic Glasses;* Academic Press: New York, 1994.

[12] Afifi, H.; Marzouk, S. Ultrasonic Velocity and Elastic Moduli of Heavy Metal Tellurite Glasses. *Mater. Chem. Phys.* **2003,** *80,* 517-523.

[13] Clark, D. E.; Folz, D. C.; West, J. K. Processing Materials with Microwave Energy. *Mat. Sci. Eng. A-Struct.* **2000,** *287,* 153-158.

[14] Rao, K. J.; Vaidhyanathan, B.; Ganguli, M.; Ramakrishnan, R. K. Synthesis of Inorganic Solids Using Microwaves. *Chem. Mater.* **1999,** *11,* 882-895.

[15] Mandal, A. K.; Agrawal, D.; Sen, R. Preparation of Homogeneous Barium Borosilicate Glass Using Microwave Energy. *J. Non-Cryst. Solids* **2013,** *371,* 41-46.

[16] Abiraman, S.; Varma, H. K.; Kumari, T. V.; Umashankar, P. R.; John, A. Preliminary *in vitro* and *in vivo* Characterizations of a Sol-Gel Derived Bioactive Glass-Ceramic System. *Bull. Mater. Sci.* **2002,** *25,* 419-429.

[17] Tenny, A. S.; Wong, J. Vibrational Spectra of Vapor-Deposited Binary Borosilicate Glasses. *J. Chem. Phys.* **1972,** *56,* 5516-5523.

[18] Dwoeidari, H.; Abou, Z.; Damraway, E. I. Effect of Gamma Radiation and Thermal Treatment on Some Physical Properties of ZnO-PbO-B_2O_3 Glasses. *J. Phys. D: Appl. Phys.* **1991,** *24,* 2222-2228.

[19] Silim, H. A. Structure and Properties of BaO-B_2O_3-Al_2O_3-NaCl Glass System Egypt. *J. Sol.* **2003,** *26,* 15-24.

[20] Nolan, M.; Perova, T. S.; Moore, R. A.; Beitia, C. E.; McGilp, J. F.; Gamble, H. S. Spectroscopic Investigations of Borosilicate Glass and Its Application as a Dopant Source for Shallow Junctions. *J. Electro Chem. Soc.* **2000,** *147,* 3100-3105.

[21] Lal, R.; Sharma, N. D.; Chandra, K. Mössbauer and Infrared Studies of Some Glasses and Glass-Ceramics from the $MnO_{(40-X)Y}Fe_2O_{3.10}Al_2O_{3.50}B_2O_3$ System. *Indian J. Pure Appl. Phys.* **2004,** *42,* 498-505.

J. Chem. Chem. Eng. 8 (2014) 358-363

Electrochemical Behavior of Electrodeposited Sn Films: Possible Negative Electrode for Na^+ Rechargeable Batteries

Reza Fathi, Riccardo Ruffo* and Claudio Maria Mari

Department of Materials Science, University of Milano Bicocca, Milano 20125, Italy

Received: January 13, 2014 / Accepted: January 28, 2014 / Published: April 25, 2014.

Abstract: Tin films on copper substrate, obtained by electrodeposition procedure, were structural and electrochemical characterized. In particular to investigate the possibility to use such metal as possible negative electrode in Na^+ rechargeable batteries, EPS (electrochemical potential spectroscopy) and galvanostatic charge/discharge cycling of the electrodes were investigated, at room temperature in organic electrolyte. Three crystalline and one amorphous phases were identified as well as high discharge capacity (738 mAh/g) was obtained after 4 cycles. Unfortunately material fading, due to the internal stress during sodiation/desodiation process, causes poor cyclability.

Key words: Sodium ion batteries, anode materials, electrodeposed tin, potential spectroscopy.

1. Introduction

Since first commercial production of Li-ion batteries in 1991, Li row material has been highly demanded to power not only portable electronic devices but also EVs and HEVs (electronic and hybrid electric vehicles). This issue has turned Li to a strategic and expensive material [1] which is unfortunately in short supply and it may not meet the industrial needs in the near future. This concern has motivated scientists to develop different battery systems and, recently, among them the Na ion rechargeable batteries, which were initially investigated earlier than Li-ion batteries became commercially available [2-4]. Since Na is one of the most abundant elements in the Earth's crust, Na^+-ion systems can really become alternative for Li-ion batteries. Considering carbon [5] and $Na_{x(x=0.66)}Mn_{0.5}Fe_{0.5}O_2$ [6] as a possible anode and cathode, respectively, the energy density, calculated according to only active materials weigh, for such a Na ion battery would be around 275 Wh/kg, which is about 70% of commercially available Li-ion battery, so far. This limitation is mainly due to two factors: The discharge voltage profiles of the mixed oxide which would reduce the operative voltage of the whole system and the lower specific capacity of the hard carbon/Na^+ system compared to the lithiated graphite. Moreover, the specific power of the battery may be limited by the low discharge kinetic of hard carbon. Similar electrochemical properties of Na and Li show that materials, electrolytes, and cell structures, which have been used in Li-ion batteries, may be suitable for Na ion rechargeable batteries; this has been already proven. Many positive electrodes, constituted of some metal oxides ($Na_{0.44}MnO_2$ [7], Na_xCoO_2 [8] $Na_xMn_{0.5}Fe_{0.5}O_2$ [6]), NASICON-type materials ($Na_3V_2(PO_4)_3$ [9]), olivine phases ($NaFePO_4$ [10]), and others ($NaVPO_4F$ [11]) were successfully used. On the contrary, even if there are some studies of possible anode materials, a good negative electrode is still one of the fundamental impediments in

*Corresponding author: Riccardo Ruffo, Assistant Professor, research fields: materials for renewable energy and electrochromic devices. E-mail: riccardo.ruffo@mater.unimb.it.

progressing Na-ion batteries; in fact, Na does not intercalate between typical graphitic carbon sheets [12]. Nevertheless, other different materials can be used as negative electrodes, among them the Na-metal alloys showing, in phase diagram, wide biphasic regions can play an important role; in particular, if the composition of each compound has high amount of sodium. For this reason, the Na-Sn system was investigated; in fact, as reported by Sangster and Bale [13], at temperatures lower than 100 °C, many biphasic regions with compounds having large amount of sodium (from $NaSn_6$ to $Na_{15}Sn_4$) are present. In such conditions, invariant and high chemical potentials of Na have to be present and electrodes with theoretical capacity of about 850 mAh/g might be realized. However, these capacity values are generally observed for a very few cycles in conventional composite electrodes. Looking at the wide knowledge coming from the investigation of such class of materials in lithium ion batteries, the first source of electrode failure is the decrepitation due to the large volume expansion and contraction during the alloying/dealloying process, respectively. In fact, the commercial available binders are not able to accept the stress induced by the strain coming from the reaction with the consequent electrode pulverization. A good way to avoid using binder is to produce Sn layer directly onto proper current collectors. This can be made by several methods, among them electro-deposition is one of the most convenient procedures for preparing Sn in different morphologies. In addition, this technique is very cheap with respect to the others, and it does not need any advanced facility. For this reason, in the present paper the charge-discharge characteristics of Sn films electrodeposited onto copper current-collectors were performed. The experiments were carried out, at room temperatures, using three electrodes T-shaped Swagelok cells having Na as counter and reference electrode and 1 M $NaClO_4$ in propylene carbonate as electrolyte; cyclability and capacity of the electrodes were investigated between 0.01 V and 1 V vs. Na/Na^+ electrode potential.

2. Experiments

2.1 Tin Films Preparation

Tin films have been deposited electrochemically on copper substrates from a chloride bath, using $SnCl_2 \cdot 2H_2O$ and tri-ammonium citrate [14]. Deposition bath was made of 50 g/L tin chloride(II) and 50 g/L tri-ammonium citrate, dissolved in distilled water. Platinum net, copper foil (1 cm^2) and SCE (standard calomelan electrode) were used as counter, working and reference electrodes, respectively. Before electro-deposition, copper substrates were degreased in acetone by applying ultrasonic waves. Depositions have been done while solution was stirring, and current density was 24 mA/cm^2 for all depositions.

2.2 Characterization

Microstructure and chemical composition of Sn metal films have been characterized by SEM (scanning electron microscopy) (Vega TS5136 XM Tescan) equipped with an EDX (energy dispersive x-ray) detector, in high vacuum configuration. X-ray diffraction measurement was carried out by Bruker D8 advance XRD (X-ray diffraction) equipped with secondary beam monochromator, copper source (kα radiation), and operating at 0.02 deg/step, and 3 sec/step.

2.3 Electrochemical Characterization

Electrochemical characterizations were carried out using three electrodes T-shaped Swagelok cells equipped with stainless steel current collectors. Sn films, deposited on Cu substrates, were sandwiched between stainless steel and Na metal disc, the latter pasted on the top of current collector. Metallic Na was used as both counter and reference electrodes, and trilayer polypolprylene membranes were used as separators. Separators were wetted by the solution of 1 M $NaClO_4$ in propylene carbonate, which was used as electrolyte. In order to remove all the aqueous remains present in the Sn films, all the electro-deposited

samples were dried in vacuum chamber over-night, after drying at 130 °C for 2 h. All potentials are reported vs. Na/Na^+ electrode value, and the electrochemical characterizations were performed using Biologic VMP3 multi-channel battery tester, at room temperature. Typical Sn load was 2.5 mg/cm^2.

3. Results and Discussion

3.1 Crystal Structure and Morphology

Fig. 1a shows SEM image of electrodeposited Sn on copper current collector in two different magnifications.

Landscape image and cross section view (Fig. 1b) show very good coverage of Sn on Cu substrate. The Sn tetragonal morphology can be easily observed at higher resolution. The EDX spectra (Figs. 1d and 1e), corresponding to the points a_1 and a_2 in Fig. 1a, show the presence of only elemental tin. In our hypothesis, at the solution/current collector interface a Sn film of few m is firstly formed acting as seeds layer for the growth of highly ordered tetragonal structures. The total film thickness is about 38 m. It has been proved that such rough morphology shows better cyclic properties with respect to smooth one [15]. Fig. 1c shows the XRD pattern of deposited tin film on copper. There are eight peaks: Six of them can be indexed to tetragonal tin [16], with a lattice parameter of a = 0.58329(8) nm and c = 0.31826(7) nm; the other two peaks can be indexed to the copper current collector.

copper. There are eight peak: Six of them can be indexed to tetragonal tin [16] with a lattice parameter of a = 0.58329(8) nm and *c* = 0.31826(7) nm; the other two peaks can be indexed to the copper current collector.

copper. There are eight peak: Six of them can be indexed to tetragonal tin [16] with a lattice parameter of a = 0.58329(8) nm and *c* = 0.31826(7) nm; the other two peaks can be indexed to the copper current collector.

copper. There are eight peak: Six of them can be indexed to tetragonal tin [16] with a lattice parameter of a = 0.58329(8) nm and *c* = 0.31826(7) nm; the other two peaks can be indexed to the copper current collector.

copper. There are eight peak: Six of them can be indexed to tetragonal tin [16] with a lattice parameter of a = 0.58329(8) nm and *c* = 0.31826(7) nm; the other two peaks can be indexed to the copper current collector.

copper. There are eight peak: Six of them can be indexed to tetragonal tin [16] with a lattice parameter of a = 0.58329(8) nm and *c* = 0.31826(7) nm; the

Table 1 Planimetric composition of studiem rocks.

No. of sample	Planimetric composition (% obj.)					Name of rock
	Ne	K-fs	Pl	Dark	Others	
07CH02	25	24	5	30	15 (ap)	Foidic syenite (khibinite)
08CH02	3	7	4	69	7 (ol) 10 (ap)	Melteigite
10CH02	20	30	0	35	7 (ap) 8 (zr)	Foidic syenite (khibinite)
11CH02-II wyp.	10	12	0	71	8 (ap)	Ijolite
11CH02-I wyp.	7	41	9	39	4 (ap)	Foidic syenite (khibinite)
13CH02	24	10	0	37	17 (ap) 12 (zr)	Foidic syenite (khibinite)
14CH02	17	14	0	58	2 (ap) 9 (zr)	Ijolite
15CH02	2	55	0	34	9 (ap)	Fiodic mikrosyenite
16CH02-II wyp.	13	16	0	71	0	Foidic syenite (khibinite)
16CH02-I wyp.	39	0	0	55	7 (ap)	Ijolite
17CH02	3	25	0	72	0	Foidic syenite (khibinite)
18CH02	15	15	9	55	6 (ap)	Melteigite
19CH02-I wyp.	13	57	0	27	4 (ap)	Foidic syenite (khibinite)
19CH02-II wyp.	6	18	0	52	24 (ap)	Foidic syenite (khibinite)
20CH02	1	38	0	55	6 (ap)	Foidic syenite (khibinite)
21CH02	1	12	0	84	4 (ap)	Ijolite
22CH02-I wyp.	3	20	3	28	48 (zr)	Foidic syenite (khibinite)
22CH02-II wyp.	0	91	0	5	5 (ap)	Foidic syenite (khibinite)
23CH02	5	22	1	72	0	Microsyenite-tinguaite
24CH02	11	20	0	45	11 (ap) 13 (zr)	Foidic syenite (khibinite)

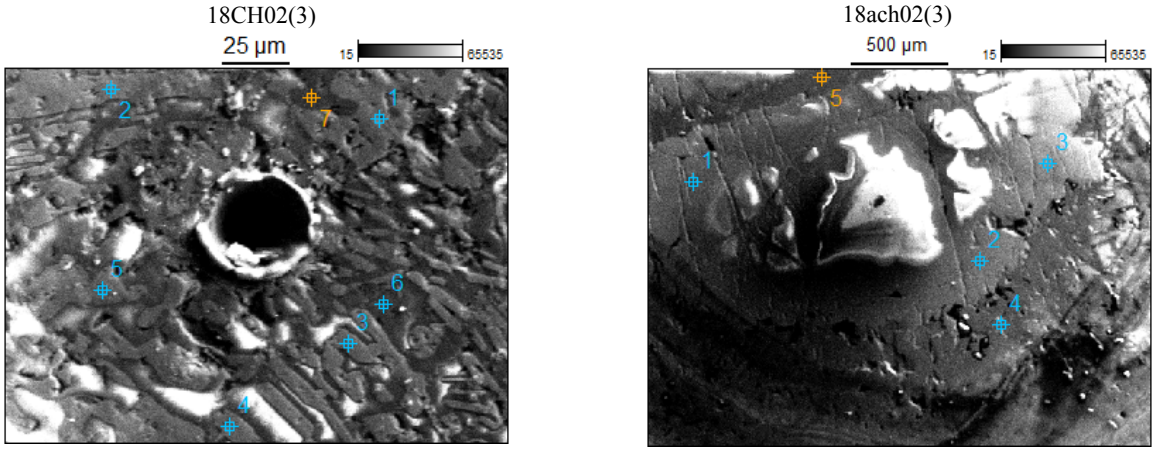
ore minerals, mainly from the group of oxides of iron and titanium with admixtures of sulfides (including copper). Such melanocratic variety of syenite more often found in repeated vein fillings. The background are the crystalls of orthoclase rarely microclines (under to 55% vol.), and aegirines (under 53% vol.) with arfvedsonite (24%), ith addition of apatite (24%), nepheline (39%), eudialite (do 48% obj), acid plagioclases (Ab, Lb, 9% vol. of rocks), and ilmenite, titanite with sulphides (pyrite and chalkopyrite). The apatite is rich with strontium-calcium compounent. Near these minerals is present the inclusions of fluorite.

Tinguaites hale a beautifull grenish color, nematoblastic, fibroblastic structure, radial, dense texture. Matrix consists of radial concentrations of aegirine and astrophillite (up to 45% vol.). Near these minerals are orthoclase (22%), nepheline (5%), and titanite (up to 3% vol.). The rocks have also magnetite and ilmenite (up to 4% vol.). These minerals form narrow blades supporting aegirynes. These veins are most frequently met in the central part of Khibina. In the background of these rocks, they are present a radial conglomerates of aegirine with astrophyllites (under 45% vol.).

Melteigites there are veins have sharp contacts with host rocks. They have lepido-nemato-crystallic structures, massive, poikilite, porphyritic textures. Phenocrystalls of minerals are augite with addition of diopsides (to 24% vol.), and nodules, usually made up of olivine (rich in Fe, Fig. 4) with rims of Fe-biotite and phlogopite (Fig. 3). Matrix is composed of apatite (up to 10% vol.), nepheline (up to 15% vol.), orthoclase (up to 15% vol.) and plagioclase (up to 9% vol.). Less frequently rocks are pyroxenites occurring in what are called pyroxene (augite) suns (79% vol.). In melteigites, pyroxene is sometimes characterized by structures such as radial augite sun. The presents pyrites have a small additin of Ni (0.5 wt.%) and Cd (0.2 wt.%).

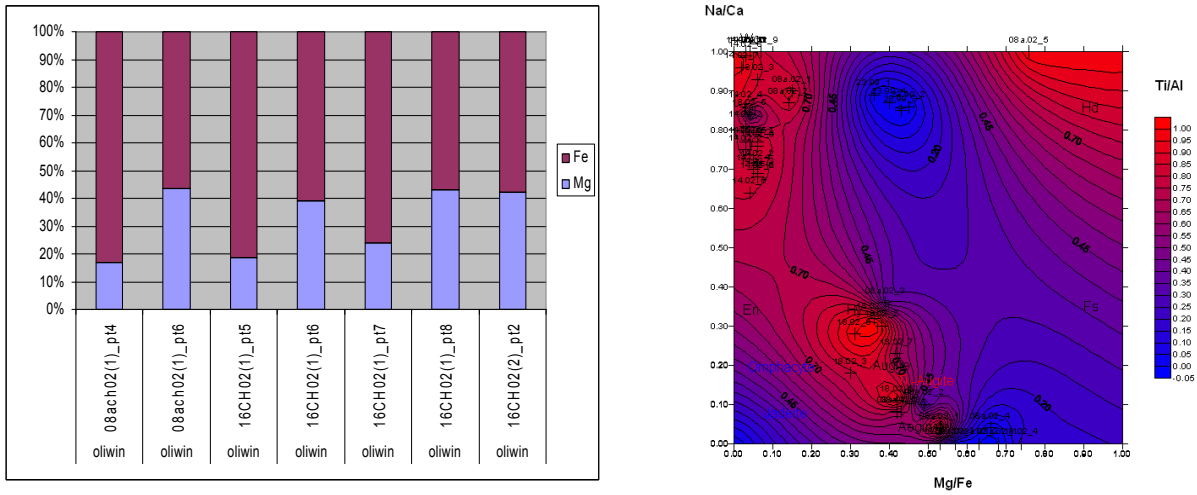
3.2 LA-CP Analysis

In the Tables 2 and 3, it is resent results of analysis



(a) The fotograph after La ICP analysis on theilmenite and augite. (b) Olywine with micas corona.

Fig. 3 Microphotographs from electron microscopy (SE) of samples rock.



(a) Projection of olywine from the melteigite rocks. (b) Pyroxene projection from the analysed samples.

Fig. 4 EDS analysis of selected minerals.

Table 2 Chemical composition of rocks used by the LA-ICP-MS (reference material: polymetalic sulphide MASS-1, USGS).

Sample	Pb	Cu	As	Zn	Cd	Ni	Co	Ag
	mg/kg (ppm)							
21CH02	15,508	3.3	24	208	23	84	11	< 1
	15,827	31	35	101	30	30	6	< 1
	15,744	33	2	233	25	10	5	< 1
	15,867	37	32	218	24	231	25	< 1
08CH02	15,888	345	25	40	24	34	17	< 1
	15,919	36	35	215	24	8	1	< 1
	15,895	32	36	234	24	8	1	< 1
	15,899	38	36	243	25	8	1	< 1
14CH02	< 1	2	< 1	< 1	< 1	2	< 1	< 1
	< 1	< 1	< 1	24	< 1	2	< 1	< 1
	< 1	2	< 1	30	< 1	2	3	< 1
18CH02	< 1	2	< 1	8	< 1	3	< 1	< 1
	< 1	1	< 1	20	< 1	7	7	< 1

Table 3 Chemical composition of rocks used by the LA-ICP-MS (reference material: REE element sof the glass matrix NIST 612).

Sample	Pb	Cu	Ni	Co	Ag	Ti	Eu	Gd	Ce
	mg/kg (ppm)								
16CH02	3	1,420	13,029	1,103	15	316	1	2	28
	< 1	26	37	7	< 1	199	13	25	771
	< 1	8	16	< 1	< 1	95,207	1	4	131
	< 1	16	19	25	< 1	4,434	3	9	91
15CHCH	24	56	53	77	3	28,387	27	78	2,275
	23	57	61	72	< 1	42,221	3	7	269
	48	109	111	178	5	52,081	< 1	3	103
23CH02	3	< 1	< 1	< 1	< 1	246	< 1	< 1	1
	3	2	2	< 1	< 1	240	< 1	< 1	4
	2	312	696	2,341	2	871	< 1	< 1	6
	3	36	9	23	< 1	640	1	1	48
	4	2	< 1	1	1	214	< 1	< 1	< 1
	3	36	7	4	< 1	153	< 1	< 1	4

selected rock samples from the study area. In the veins samples is present a higher content of Pb and Zn (samples 21CH02 and 08CH02). In samples: 16CH02 and 15CH03 was measured a high contents of Ti, Ni and Ce.

4. Conclusions

Describe veins rocks from Khibina have advanced syenitization processes. The primitive mineral association has a corrosion in rocks veins. This was a product of mixed chemical composition of veins materials with occur rocks. The melteigite rock probably is a differenciation product in the intrusive magma and migration of basic derivates with contamination of syenite fluids. These fluids make unstable the ol-opx association (Figs. 3 and 4). In next step, a cpx minerals was crystallized which was make aegirinization (secondary processes). It can provide the numerous structures disintegrating, crowns reaction in olivine and pyroxene around, and relatively high content in the background a nepheline and feldspar. In addition, vein rocks fill the various discontinuities accompanying the transition zone which is undoubtedly limit ore occurrences and khibinites. This causes multistage migration of fluids in zones splits and enrichment rock core in the phase associated with the crystallization of residual and after-magmas processes [4]. Hence, are visible in the area of various multiple fill the same vein different generation and the presence of carbonate minerals found in many rocks in Khibina [3, 9, 10] and the enrichment of these rocks in the elements cerium group. In addition, the activity associated with hydrothermal after-magmas processes involves the enrichment of these rocks Zn-Pb sulphides and minerals, for example, fluorite.

Acknowledgments

Special thanks to Professor Agnieszka Gałuszka from the Jan Kochanowski University in Kielce for making the analyses using the LA-ICP-MS technique of selected rocks samples.

References

[1] Borucky, B. E. *Rock-Forming Minerals of High-alkaline Complexes;* Nauka, 1989; p 214.

[2] Kogarko, L. N.; Kononova, V. A.; Orlova, M. P.; Woolley, A. R. *Alkaline Rocks and Carbonatites of the World. Part 2: Former USSR;* Chapman&Hall: London, 1995; p 226.

[3] Kramm, U.; Kogarko, L. N.; Kononova, V. A.; Vartiainen, H. The Kola Alkaline Province of the CIS and Finland: Precise Rb-Sr Ages Define 380-360 Ma Age Range for All Magmatism. *Lithos*. **1993,** *30,* 33-44.

[4] Huber, M. Preliminary Characterization of the Mineral Veins Occurring in the Malaya Belaya Valley in the Khibiny. *J. Biol. Earth Sci*. **2013,** *3(1),* E1-E11.

[5] Pozhylienko, W. I. *Geology of Mineral Areas in Murmansk Region;* Apatity, 2002; p 360.

[6] Arzamastsev, A. A. *Unique Paleozoic Intrusions of the Kola Peninsula;* Apatity: Kola Scientific Centra, 1994; p 79.

[7] Arzamastsev, A.; Yakovenchuk, V.; Pakhomovsky, Y.; Ivanyuk, G. The Khibina and Lovozero Alkaline Massifs: Geology and Unique Mineralization. *33 IGC Excursion Materials* **2008.**

[8] Mitrofanov, A. F. *Geological Characteristics of Kola Peninsula;* Russian Academy of Science: Apatity, 2000; p 166.

[9] Huber, M.; Hałas, S.; Sikorska, M. Evolution of Prehnite-Albite-Calcite Veins in Metamorphic Rocks from the Lapland Granulite Belt (Kandalaksha Region of Kola Peninsula). *Geologija* **2007,** *57,* 1-7.

[10] Hałas, S.; Huber, M.; Piestrzynski, A. Petrology of Gabbroides and Isotope Signature of Sulfide Mineralization from Fedorov-Pansky Layered Mafic Intrusion. *Geochronometria* **2009,** *33,* 19-22.

J. Chem. Chem. Eng. 8 (2014) 371-377

Obtaining Porosity of Concrete Using X-ray Microtomography or Digital Scanner

Jose Renato de Castro Pessoa*, Joel Sanchez Dominguez, Gil de Carvalho and Joaquim Teixeira de Assis
Politechnical Institute of Rio de Janeiro State University, Nova Friburgo 28625-570, Brazil

Received: March 14, 2014 / Accepted: April 08, 2014 / Published: April 25, 2014.

Abstract: The aim of this work is to determine the porosity of concrete by means of two NDT (non-destructive testing) using digital images. In one test, the images were obtained through X-ray microtomography and for another test via digital scanner. In both of the tests, the images were processed using techniques of mathematical morphology and pixel processing. For both NDT, it was used concrete samples with 20-30 MPa of compressive strength. The results for the porosity were compared with results obtained by the standard test proposed by NBR (Norma Brasileira) 9778 (2005) showing the compatibility between two studied methods and pattern method.

Key words: Concrete porosity, X-ray microtomographic, images processing, matematical morfology.

1. Introduction

The porosity of a material can be thought as a property to present pores or voids and is symbolized by the fraction of the total mass of a sample that is occupied by pores or voids. In the concrete matrix, the porosity has a great influence on their mechanical strength, workability and durability. By the previous becomes important to develop methods to regulate not only the index of voids, but besides the physical characteristics and placement of the pores.

Different methods for determining the porosity of concrete does not always result in similar values. That is because traditional testing methods for determining this index usually change the structure of the cement paste, especially when they involve the addition or emulsion of liquid [1]. An example is the use of mercury intrusion to study the pore system of the cement paste, admitting that the pores will be narrowing with increasing depth, whereas in fact, some pores have a narrower aperture, thus distorting the value of the porosity determined by this method [2]. Systematization of methods to determine the porosity of some materials has been the object of the works being produced over time. Some of these methods use high-quality images and work with techniques and programs of digital image processing.

In this study, two NDT (non-destructive testing) to obtain the porosity of concrete were used. In the first, NDT X-ray microtomography was used with the purpose of being acquired digital images of the internal structure of the test-bodies. In the second, NDT a commercial scanner was used to directly scan the surfaces of cross sections of these tests-bodies. For both tests, the images were digitally processed to measure the porosity of the material. This digital image processing consisted mainly in performing mathematical morphology operations and processing of pixels.

The average surface porosity found in the concrete were compared with the volumetric porosity detected using the Brazilian standard NBR (Norma Brasileira) 9778 (2005) [3]. This method is a pattern for this kind of measures; tests with the standard method were performed in the Department of Materials Engineering,

*Corresponding author: Jose Renato de Castro Pessoa, Professor, research fields: concrete technology, materials characterization, tomography, images processing and structural analyzes. E-mail: jpessoa@iprj.uerj.br.

Federal University of São Carlos SP. In Section 2, we are presented some basics related to image processing and mathematical morphology; the Section 3 showing the experimental procedure and commented the performed tests and the Section 4 presented the obtained results and conclusions.

2. Images Processing

Understanding an image as a compact way to represent a lot of information, in a system of image processing this information may go through diverse forms of representation depending on the purpose defined for the application. The first step of the system is the acquisition of an image, where one type of sensor can be used for digitizing. The sensor may be a scanner, a TV camera, a photo camera, a CT scan, etc.. The nature of the sensor and the image it producing is determined by the application.

In image processing, morphological study focuses on the geometric characteristics of the images and applies in many areas of image processing, such as filtering, segmentation, enhancement and others [4].

The main idea of mathematical morphology consists of sets of picture elements (pixels), which are placed in groups, representing a 2D structure (shape), and over which mathematical operations are carried to highlight specific aspects of the forms so that they can be recognized and measures [5].

A mathematical morphology can be translated as the application of mathematical definitions and principles emphasizing specific aspects of the forms allowing them to be counted or recognized. It is a methodology for the description of operators, and its base is to extract from unknown image its geometry and topology by using the transformation of another completely defined image, called structuring element image. The main applications of mathematical morphology are in the process of noise filtering, segmentation parts, skeletization, etc. [6].

3. Experimental Procedure

The test-bodies were molded in concrete with 20 MPa and concrete with 30 MPa compressive strength, the materials were collected in a cement truck. Table 1 shows the dimensions of cylindrical test-bodies used in each testing.

The bodies were originally molded with 200 mm × 100 mm, and which were cut to build the smaller bodies.

3.1 Volumetric Porosity by NBR 9778

The procedures for performing this test are described in detail in the Brazilian standard NBR 778 (2005). The method is based on the technique of mercury porosimetry. This technique consists essentially in measuring the extent of mercury penetration into an evacuated solid as a function of the applied hydrostatic pressure. The use of these techniques requires specialized equipment and the proper handling of mercury for it to be a contaminant element. Table 2 shows the values of volumetric porosity obtained in the test for each of the studied samples.

3.2 Surface Porosity by Microtomography

To accomplish, the X-ray microtomography was used a compact instrument for high-resolution microtomography (14.97 μm) from Sky Scan, model 1172. This system has a variable size of focus depending on the power applied. Table 3 summarizes the main characteristics of this equipment.

In order to minimize distorting effects of CT due to the beam hardening effect [7], two filters (Al + Cu) were used, placed between the radiation source and the object to be inspected. Fig. 1 shows the CT

Table 1 Dimensions for cylindrical test-bodies.

Method	Diameter (mm)	Height (mm)
NBR 9778	100	200
Micro CT	25	50
Scanner	100	15

Table 2 Values of volumetric porosity with NBR 778.

Concrete	Volumetric porosity (%)
20 MPa	1.9
30 MPa	2.1

Table 3 Main features of the Sky Scan 1172.

Device	Characteristics
X-ray source	20-100 kV, 10 W, < 5 µm 20-80 kV, 8 W, < 8 µm
X-ray detector	11 Mp, CCD (charge couple device) of 12-bits with optical coupling to a scintillator
Maximum size of the object	27 mm in diameter (single sweep)
Details of detectability	< 0.8 µm at the highest resolution
Reconstruction	Computer or cluster
Radiological safety	< 1 µSv/h at any point on the equipment surface

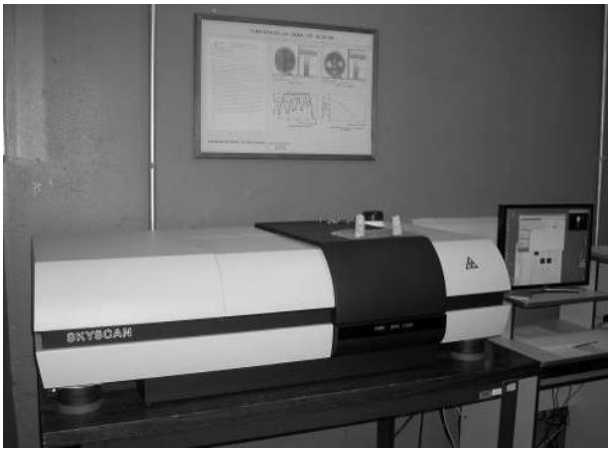


Fig. 1 CT scanner Sky Scan 1172.

scanner used in the research. Due to the CT scanner used can only measure samples of concrete with small diameter, we used 7 cylindrical test-bodies whose dimensions were specified in Table 1.

A program was developed in MATLAB® to read each generated image and determine the area of voids to obtain the surface porosity. In this program, only two parameters required user intervention the contrast intensity and the binarization threshold. These parameters were modified for each set of processed images. For each body-test, an average of 1,000 images were obtained. Each image was adjusted in contrast, binarized and filtered using morphological closing operation (dilatation followed by erosion) with circular structuring element with 2 pixels of radius to remove isolated points interpreted as noise. In the 2D result, the empty spaces images were counted. The Fig. 2 showed the sequence of operations of the developed program.

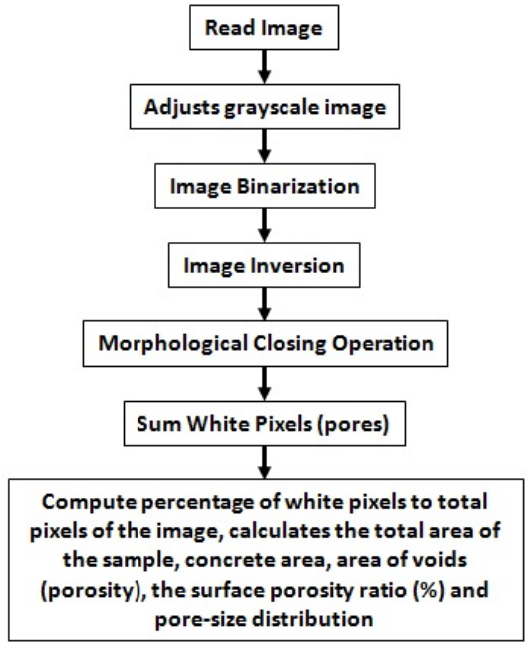


Fig. 2 Flow diagram of software to process tomography images.

The Eq. (1) was used to compute the surface porosity of concrete.

$$P(\%) = \frac{A_T - A_c}{A_T} * 100 \quad (1)$$

where, P represented the superficial porosity and A_T, A_C are total area and concrete area, respectively.

Fig. 3 shows a cross-section with two cuts from an image reconstructed from radiographs obtained.

Fig. 4 shows the processing stages of reconstructed slice acquired in microtomography process.

Tables 4 and 5 show the results achieved with this method for the samples tested with compressive strength of 20 MPa and 30 MPa, respectively. The

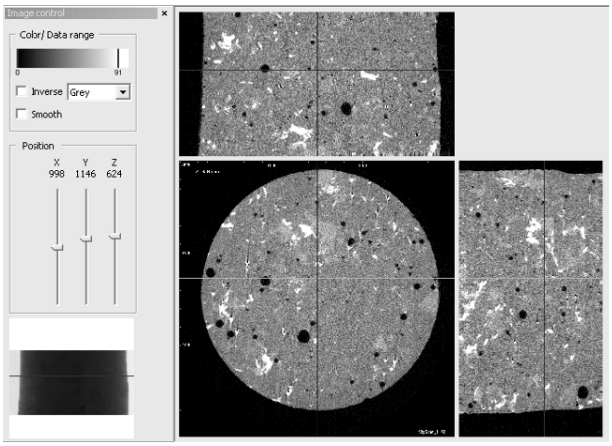


Fig. 3 Two cuts from a reconstructed images.

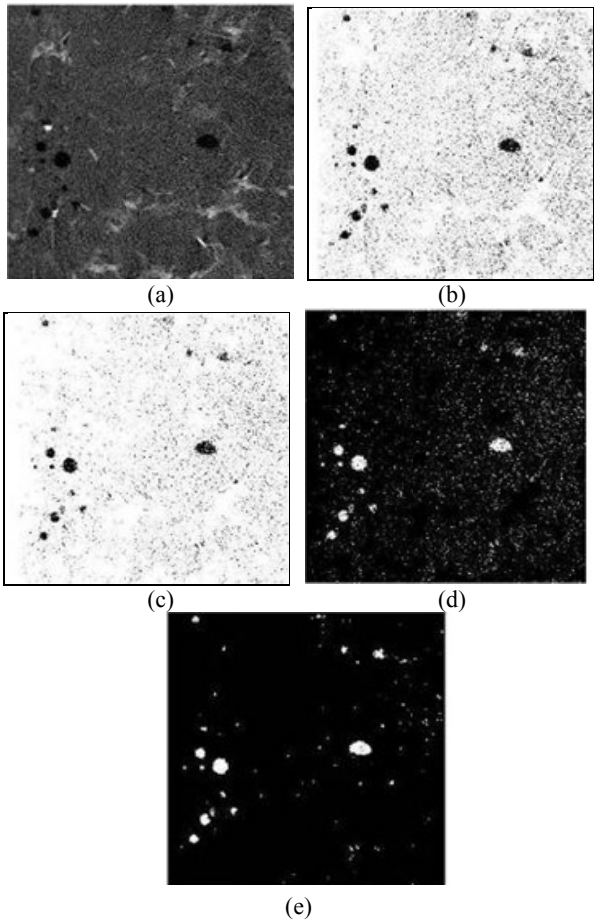


Fig. 4 Processing stages of tomography images: (a) Original image; (b) Ajusted image; (c) Binarized image; (d) Inverted image and (e) Filtered image.

Table 4 Surface porosity for bodies of 20 Mpa concrete.

Test-body	Images	Surface porosity (%)	Standard deviation (%)
1	1,045	1.1	0.57
2	1,044	0.8	0.42
3	1,044	1.4	0.97
4	1,044	0.6	0.52
5	1,046	1.2	1.27
6	1,046	0.9	0.77
7	1,046	1.4	1.06

Table 5 Surface porosity for bodies of 30 Mpa concrete.

Test-body	Images	Surface porosity (%)	Standard deviation (%)
1	1,046	1.0	0.80
2	1,046	1.2	0.55
3	1,046	2.3	1.62
4	962	0.9	0.57
5	1,046	2.5	1.26
6	1,046	1.3	0.67
7	1,046	2.2	0.95

Table 6 Porosity values obtained with microCT.

Concrete	Number of images	Volumetric porosity (%)
20 MPa	7,315	1.0
30 MPa	7,238	1.6

Tables 4 and 5 columns represent the sample number, the number of images analyzed, the surface porosity and the standard deviation between images of the same test-body.

The standard deviation of about 1% of all samples studied indicate the similarity of the porosity values calculated for each slice of the reconstruction belonging the same test-body. Table 6 shows the total mean surface porosity for the two series of test-bodies.

3.3 Surface Porosity by Scanner

Forty-two circular surfaces measuring 100 mm in diameter acquired from cylindrical test-bodies of 100 mm diameter by 15 mm in height were used for each type of concrete. On each surface were acquired four square images measuring 25 mm side, totaling 168 images to be analyzed for each particular type of concrete. A shield made with transparent plastic with openings in the reading area was used so the concrete surface, which did not damage the scanner glass. Fig. 5 shows an example of the concrete surface to be scanned.

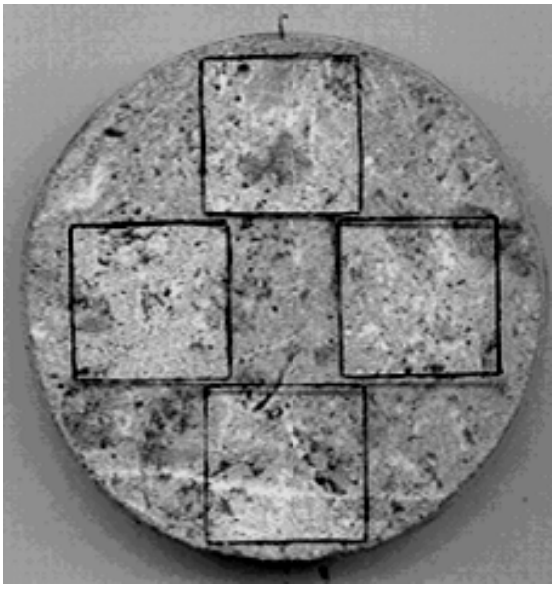


Fig. 5 Concrete surface to be scanned.

The images were scanned using a multifunctional EPSON TX200 and digitized with 2400 dpi of resolution. To crop the interest areas, the tools available on a typical software was used to manipulate images how to Paint or Photoshop. A program was developed in MATLAB® to read the cropped images and process them in order to determine which areas are empty. Each image was read and subsequently separated into its HSV (Hue, Saturation and Value mode color) components, since the images obtained by the scanner are in RGB (Red, Green and Blue color mode) and not grayscale as in the case of images obtained by microtomography. HSV was chosen over the standard RGB because this was not possible to clearly identify the pores in any of its layers, R, G or B. Making use of the HSV standard, the layer V was chosen for processing; due to this layer had the best representation of pores in the image. Each image was converted to HSV pattern, extracted V layer; then V layer was adjusted in contrast, binarized and filtered using morphological closing operation. In the result image, the empty spaces were counted. The Fig. 6 showed the sequence of operations of the developed program to process the cropped images acquired with the scanner.

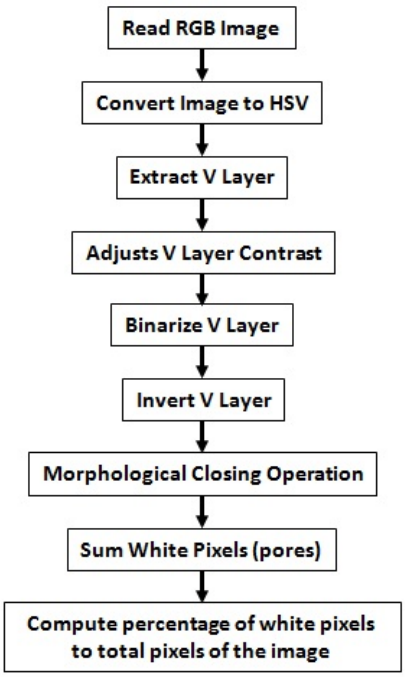


Fig. 6 Flow diagram of software to process scanned images.

In this program, it also the parameters contrast intensity and binarization threshold requiring user intervention. These parameters were adjusted for each group of processing images. Fig. 7 shows the processing stages of the image acquired cutting scanned image.

With the same structure of Tables 4 and 5, Tables 7 and 8 shows the results achieved with this method for both types of concrete.

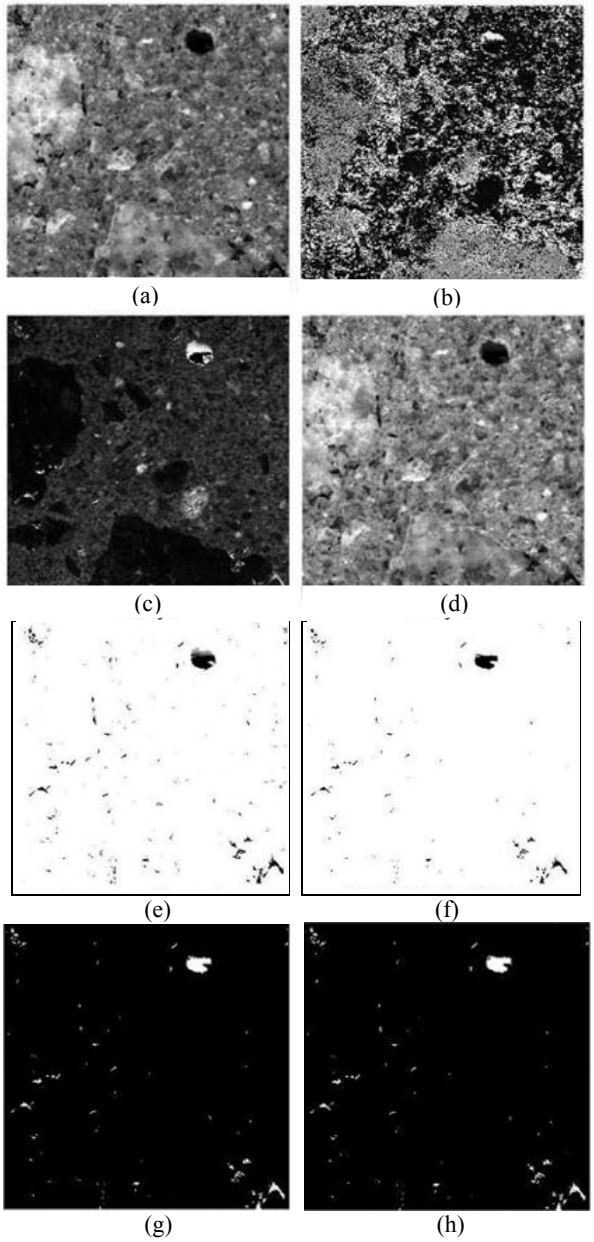


Fig. 7 Processing stages of scanned images: (a) Original image; (b) H layer; (c) S layer; (d) V layer; (e) Ajusted image; (f) Binarized image; (g) Inverted image and (h) Filtered image.

Table 7 Surface porosity for bodies of 20 Mpa concrete.

Test-body	Images	Surface porosity (%)	Standard deviation (%)
1	24	1.08	0.53
2	24	1.67	0.82
3	24	1.46	0.45
4	24	2.28	1.46
5	24	2.03	1.81
6	24	1.63	0.57
7	24	1.79	0.73

Table 8 Surface porosity for bodies of 30 Mpa concrete.

Test-body	Images	Surface porosity (%)	Standard deviation (%)
1	24	1.04	0.48
2	24	1.15	0.56
3	24	1.65	0.58
4	24	1.98	0.71
5	24	1.58	0.53
6	24	1.64	0.53
7	24	1.92	0.71

Table 9 shows the total mean surface porosity for the two series of test-bodies.

4. Analysis of Results and Conclussions

Table 10 summarizes a comparison between the results obtained by the two methods discussed in this work and the results of the test prescribed in NBR 9778.

Considering that, the linear surface porosity and volumetric porosity must be equivalent. The average surface porosity found using microtomography and scanner can be compared with the volume porosity found in the samples of concrete, prepared with the same batch and tested by the method shown in NBR 9778. Table 10 shows some differences between the values found for the concrete porosity by different methods; these possible differences were also commented by other authors [7].

Analyzing the two methods used to measure the concrete surface porosity, similar results were found in the 30 MPa concrete and difference values for the 20 MPa concrete. These differences could be due to the selection of parameters contrast intensity and binarization by the program user. With this selection,

Table 9 Porosity values obtained with scanner.

Concrete	Number of images	Volumetric porosity (%)
20 MPa	7,315	1.0
30 MPa	7,238	1.6

Table 10 Results summary to concrete porosity.

Concrete	Average surface porosity		Volumetric porosity (%)
	MicroCT	Scanner	NBR 9778
20 MPa	1.7	1.0	1.9
30 MPa	1.6	1.6	2.1

what may happen is that some pores are lost or some noise can be considered as pore.

It can be seen that the porosity found for 20 MPa concrete by the method was shown in NBR 9778 and found by analysis of images obtained by microtomgraphy is lower than that found in the 30 MPa concrete. This may be due to changes in the water cement ratio in the feeder of cement truck change the voids in concrete with higher strength, since that the technical literature reports higher values of porosity for concrete with lower resistance. In general, to analyze the compressive strength of the concrete should also be considered the size and distribution of pores; in our samples the 30 MPa concrete has a higher amount of smaller pores.

The use of imaging by microtomography or the use of a scanner (in both cases complemented with techniques of image processing) is shown as viable methods to estimate the concrete porosity. The method using the scanner is presented as an acceptable method for their results, and especially for its low cost and ease operation.

Acknowledgments

The authors acknowledge the support given by the Carlos Chagas Filho Foundation for Research Support of the State of Rio de Janeiro (FAPERJ), and Embrapa/CNPDIA-San Carlos.

References

[1] Neville, A. M. *Concrete Properties;* São Paulo, 1997.

[2] Cook, R. A.; Hover, K. C. Mercury Porosimetry of Cement-Based Materials and Associated Correction

Factors. *ACI Materials Journal* **1993,** *90(2),* 152-161.

[3] ABNT. NBR Hardened Mortar and Concrete-Determination of Water Absorption and Void Index Density, 2005.

[4] Jain, A. K. *Fundamentals of Digital Image Processing;* Prentice Hall: New Jersey, 1989.

[5] Banon, G. J. F.; Barrera, J. Bases da Morfologia para a Analysis of Binary Images. INPE, São José dos Campos, 1998.

[6] Meyer, F. Automatic Screening of Cytological Specimens. Computer Vision. *Graphics and Image Processing* **1993,** *35,* 356-369.

[7] Lima, I. Histomorphometric Quantification 2D from 3D CT. Master Thesis 2002.

J. Chem. Chem. Eng. 8 (2014) 378-384

Nano Fibrous Cerium(IV) Hydrogen Phosphate Membrane Self Supported Indole Polymerization Agent

Sadek Khalifa Shakshooki*

Department of Chemistry, Faculty of Science, Tripoli University, Tripoli 13203, Libya

Received: February 13, 2014 / Accepted: February 28, 2014 / Published: April 25, 2014.

Abstract: Nanosized fibrous cerium(IV) hydrogen phosphate membrane, $Ce(HPO_4)_2 \cdot 2.9H_2O$ ($nCeP_f$), was prepared and characterized by chemical, XRD (X-ray diffraction), TGA (thermogravimetric analysis), SEM (scanning electron microscopy) and TEM (transmission electron microscopy). Novel supported nanofibrous Ce(IV) phosphate/polyiondole nanocomposite membranes were prepared via in-situ chemical oxidation of the monomer that was promoted by the reduction of Ce(IV) ions present in the inorganic matrix. The presence of Ce(IV) ions allows redox reactions necessary to oxidative polymerization to occur. The resultant material was characterized by TGA, elemental (C, H, N) analysis and FT-IR (Fourier transform spectroscopy). SEM images of the resulting nanocomposite reveals a uniform distribution of the polymer on the inorganic matrix. Amount of polyindole polymer present in the composite is found to be ~ 7.0%.

Key words: Nanofibrous cerium(IV) hydrogen phosphate membrane, self support polymerization, indole.

1. Introduction

In recent years, heterocyclic conducting polymers containing nitrogen atoms like polyaniline and polypyrrole, and their substituted derivatives have received increasing attention in various fields, electronics, industry and others [1-3]. Their electrical and electrochemical properties show great promise for commercial applications. However, among various aromatic compounds-based conducting polymers, polyindole and its derivatives has been less investigated although there exists close structural similarities with the polymers mentioned above [4]. Polyindole can be obtained from chemical, electrochemical and interfacial polymerization of indole [2, 3, 5, 6]. Its electrical and electrochemical properties show great promise for commercial applications [5-10]. Polyindole is an electro active polymer, owns advantages especially fairly good thermal stability [5, 6]. Some studies shows polyindole has similar properties like polyaniline, based on their high conductance and good environmental stability [2, 4, 11-13]. Inorganic layered nanomaterials are receiving great attention because of their size, structure, and possible biochemical applications [14, 15], that have been proven to be good carriers for organic polar molecules. Examples of these are zirconium phosphates, $Zr(HPO_4)_2 \cdot H_2O$ (ZrP), which are inorganic cation exchange materials with high thermal stability, solid-state ion conductivity, resistance to ionizing radiation, and which are known as hosts capable of incorporating different types and sizes of guest molecules [15].

Researchers have been capable of encapsulating functional biomolecules into these inorganic matrices protecting them from interacting with environment, avoiding denaturation and enhancing their shelf life [14, 15]. Crystalline cerium phosphates have been studied for a long time as ion exchangers, their structures remains unknown until recently [16-18].

*Corresponding author: Sadek Khalifa Shakshooki, Professor, research field: inorganic chemistry of tetravalent metal phosphates and tellurates. E-mail: shakshooki2002@yahoo.com.

The reason is that, the composition, the structure and the degree of crystallinity of their precipitates results from reaction of solutions containing a Ce(IV) salt which is mixed with a solution of phosphoric acid of [(PO_4)/Ce(IV) ratio], strongly depend on the experimental conditions such as rate and order of mixing of the solutions, stirring, temperature and digestion time, this also implemented on fibrous cerium phosphate [19]. To date, most of the work on fibrous cerium phosphate was carried out on its ion exchange [20], intercalation [21] and electrical conductance properties [22]. Studies on its polystyrene, polyacrylamide [23] and (polyvinyl chloride-based polyvinyl (alcohol) [24] composites have been reported. Nanoscaled tetravalent metal phosphates and their organic polymer composites comprise an important class of synthetic engineering. However, research in such area is still terra incognita [25-28]. Nanotechnologies are at the center of numerous investigations and huge investments. However, chemistry has anticipated for long the importance decreasing the size in the search of new properties of materials, and of materials structured at the nanosize in a number of applications relate to daily life. Organic-inorganic nanocomposite membranes have gained great attention recently [28, 29]. The composite material may combine the advantage of each material, for instance, flexibility, processability of polymers and the selectivity and thermal stability of the inorganic filler [26-30]. Conducting polymers are interesting materials owing to their electrical properties [25, 27]. Belonging to this class are polyaniline, polypyrrole, polybenzimidazole and others. Polyppyrole polymerization by fibrous ceium phosphate has been reported [31, 32].

In our laboratory, we are carrying systematic investigations on novel tetravalent metal phosphates/organic heterocyclic conducting polymers nanocomposite membranes. Recently, we have reported [33] the preparation and characterization of fibrous cerium phosphate/polybenzimidazole nanocomposite membrane. The present study describes the preparation and characterization of novel supported fibrous cerium phosphate/polyindole nanocomposite membranes via in-situ chemical oxidation that was promoted by the reduction of Ce(IV) ions presenting in the inorganic matrix.

2. Experiments

Chemicals $Ce(SO_4)\cdot 2.4H_2O$, H_3PO_4 (85%) of British drug house, PVA (Polyvinylealcohol), MWt (molecular weight) = 25,125 g/mol of Aldrich., Indole of Reidel de-Haen, were used as such. Other reagents used were of analytical grade.

2.1 Instruments Used for Characterization

X-ray powder diffractometer Siemens D-500, using Ni-filtered CuKα (λ = 1.54056 Å); TG/DTA (thermogravimetric loss/differential thermal analysis), DTSIIExtra 6000 Thermogram and TG/DTA Perkin-Elmer SII; Fourier Transform IR spectrometer, model IFS 25 FT-IR, Bruker; SEM (scanning electron microscopy) Jeol SMJ Sm 5610 LV; TEM (transmission electron microscopy) Zeiss TEM 10CR and pH Meter WGW 521.

2.2 Preparation of Nanofibrous Cerium Phosphate Membrane: $Ce(HPO_4)_2\cdot 2.9H_2O$

Nanofibrous cerium phosphate membrane was prepared from adding 150 mL of 0.05 M $CeSO_4\cdot 4H_2O$ in 0.5 M H_2SO_4 solution, dropwise, to 150 mL of 6 M H_3PO_4 at 80 °C with stirring. After complete addition, the resultant material left to digest at that temperature for 5 h. To that, 1 L of hot distilled water, (~ 60 ^oC), was added with stirring for 1 h. The resulting fibrous cerium phosphate was subjected to washing by with distilled water up to pH 3, then filtered, washed with ethanol and dried in air.

2.3 Exchange Capacity

Exchange capacity of nanosized fibrous cerium phosphate membrane was determined by addition of 25 mL of 0.1 M NaCl solution to 100 mg of the

material, with stirring for 1 h, then titrated with 0.1 M NaOH solution.

2.4 Thermal Analysis

Thermal analyses were carried out at temperature range about 20-775 °C in nitrogen atmosphere, the rate was 10 °C/min.

2.5 Preparation of Nanofibrous Cerium Phosphate Polyindole Composite Membranes

Cerium phosphate/polyindole nanocompsite membranes were prepared as follows:

(1) By immersion of fibrous cerium phosphate self supported-sheet 160 mg in 10 mL ethanol solution containing 200 mg indole, at room temperature for 5 days. It was observed with time the color changes gradually (pale brown, brown and finally to dark brown). The impregnated sheet was removed, washed with ethanol and left to dry in air.

(2) By immersion of fibrous cerium phosphate self supported-sheet 160 mg in 10 mL ethanol solution containing 200 mg indole, at room temperature for 2 days. It was observed with time the color changes gradually (pale brown and finally to brown). The impregnated sheet was removed, washed with ethanol and left to dry in air.

3. Results and Discussion

Nanofibrous cerium phosphate membrane, Ce $(HPO_4)_2 \cdot 2.9H_2O$ (nCePf), was prepared and characterized by chemical, XRD, TGA, FT-IR, SEM and TEM.

XRD of nCePf is shown in Fig. 1, with d_{001} = 10.89 Å

Thermogram of nCePf is shown in Fig. 2. The thermal decomposition occurs in continuous process, the thermal analysis was carried out at temperatures between 10-775 °C, the final product was CeP_2O_7. Loss of water of hydration occurs between 60-200 °C, followed by POH groups condensation. The total weight loss found to be equal to 19.09%.

Fig. 3 shows FT-IR spectrum of fibrous $Ce(HPO_4)_2 \cdot 2.9H_2O$, with a trend similar to that of M(IV) phosphates. It consists of broad band centered at 3,350 cm^{-1} is due to OH groups symmetric stretching of H_2O, small sharp band at 1,628 cm^{-1} is related to H-O-H bending, and sharp broad band centered at 1,045 cm^{-1} is corresponds to phosphate groups vibration. The bands at the region 630-450 cm^{-1} are ascribe the presence of $\delta(PO_4)$.

SEM morphology image of the nanosized fibrous cerium phosphate (nCePf) is shown in Fig. 4. The photograph shows its average size is ~ 20.5 nm.

The ion exchange capacity of nanosized fibrous cerium(IV) phosphate, $Ce(HPO_4)_2 \cdot 2.9H_2O$, found to be equal to 5.21 meq/g.

TEM image of the nanosized fibrous cerium phosphate (nCePf) is shown in Fig. 5. The photograph shows its average size is ~ 15 nm.

New supported polyindole nanocomposite was

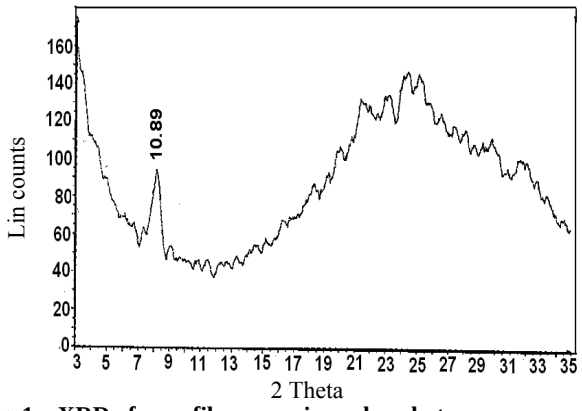


Fig. 1 XRD of nanofibrous cerium phosphate.

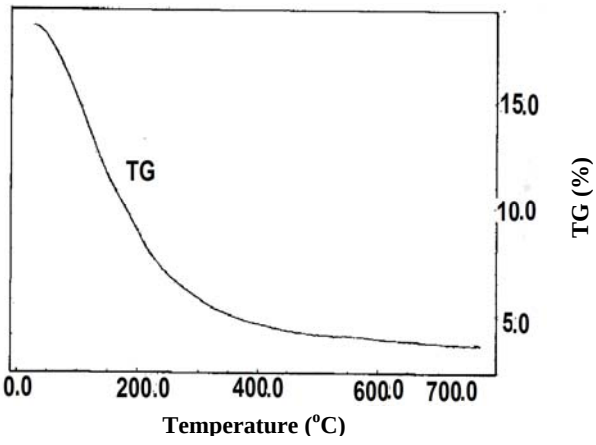


Fig. 2 TGA of nanofibrous cerium phosphate.

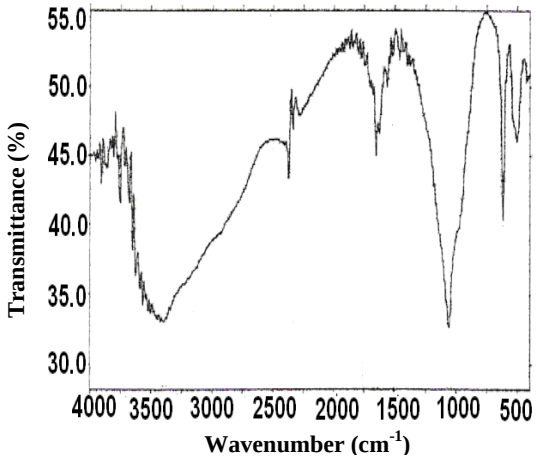


Fig. 3 FT-IR spectra of nanofibrous cerium phosphate.

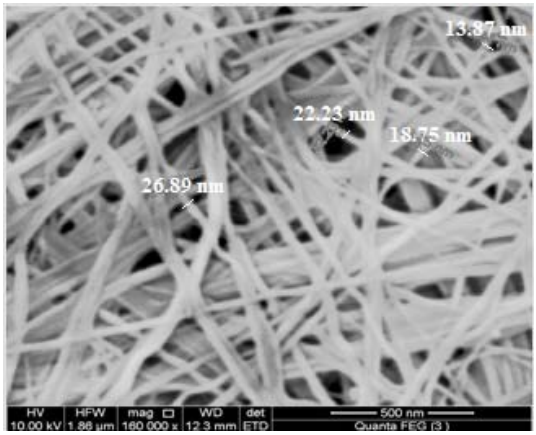


Fig. 4 SEM morphology image of (nCePf).

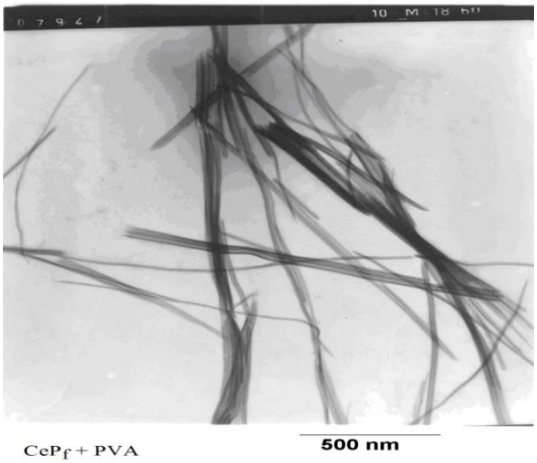


Fig. 5 Miograph image (TEM) of (nCePf) composite thin film in PVA matrix.

prepared and investigated in this work. Self-supported sheet of nanosized fibrous cerium(IV) hydrogenphosphate, $Ce(HPO_4)_2 \cdot 2.9H_2O$ (nCePf), was used as the inorganic matrix, since the fibrous morphology present by this material makes molding possible, giving desired shape to the final (nCePf)/polyindole naoncomposite membrane. It was found that when nanosized fibrous cerium(IV) hydrogen phosphate immersed in ethanolic solution of polyindole the color of self supported sheet gradually changes with time to (pale brown, brown and finally to dark brown) due to the formation of nanocomposite membrane. It is important to note that the self-suported sheet integrity is preserved. This result is interesting because the shape integrity makes the building of molded conducting device possible. The resultant material was characterized by elemental (C, H, N) analysis TGA and by FT-IR spectroscopy.

From elemental (C, H, N) analysis, the amount of organic material present in the (nCePf) polyindole naoncomposite was 6.81% in weight. The % of elemental (C, H, N) related to the organic polymer found to be C = 5.58%, H = 0.41% and N = 0.82%. From TGA analysis, the amount of the organic polymer found to be 7% in weight. However, on repeating the same experiment for a period 48h time immersion of fibrous cerium phosphate in indole solution, gave low yield of polyindole (3.97% in weight). It is elemental (C, H, N) analysis, were C = 3.26%, H = 0.327% and N = 0.475%. So, the degree of polymer loading can be controlled by varying aging time.

Fig. 6 shows SEM image for (nCePf)/polyindole naoncomposite membrane, reveal a uniform distribution of the polymer on the inorganic matrix, coating the nCePf and filling the empty spaces between the fibers. Amount of polyindole present in the composites was found to be 7% in weight.

Fig. 7 shows FT-IR spectrum of (nCePf)/polyindole nanocomposite membrane. It consists of broad band centered at 3,425 cm^{-1} is due to OH groups symmetric stretching of H_2O, small sharp band at 1,632 cm^{-1} is related to H-O-H bending, and sharp broad band centered at 1,055 cm^{-1} is corresponds to phosphate groups vibration. Small band at 2,921 cm^{-1} corresponds

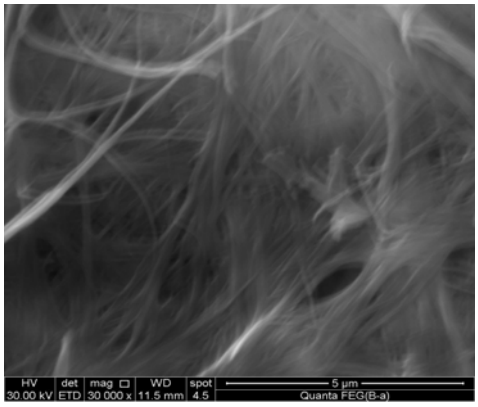


Fig. 6 SEM image of (nCePf)/polyindole nanocomposite.

to C-H bonds, bands in the region of 1,557-1,500 cm^{-1} are related to stretching C-C bonds characteristic of indole unites, bands in the region 1,500-1,400 cm^{-1} corresponds to C-N bonds. The band at 742 cm^{-1} is correspond to out of plane deformation of C-H bond in the benzene ring [34].

Thermogram of (nCePf)/polyindole nanocomposite membrane is shown in Fig. 8, the weight loss up to 180 °C is 7.35% due to the removal of external water molecules. The weight loss occurs between 180-700 °C corresponds to the decomposition of polyindole and condensation of P-OH groups of the inorganic material to pyrophosphate, CeP_2O_7. The POH groups condensation found to cuoerimose with that of polyindole. The total weight loss found to equal to 18.562%. From thermal and elemental (carbon, hydrogen, nitrogen) C, H, N analysis, the resultant

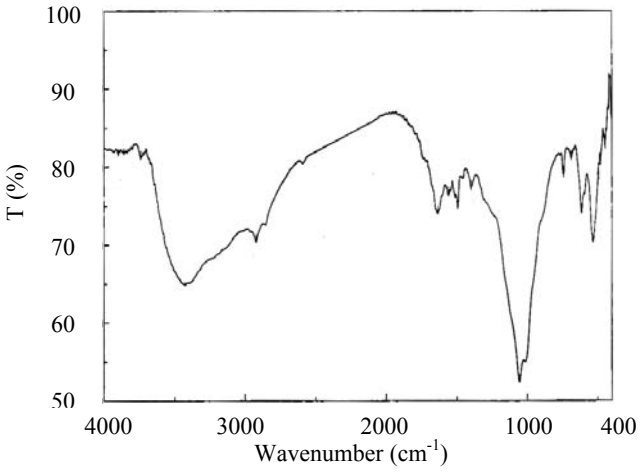


Fig. 7 FT-IR spectrum of (nCePf)/polyindole nanocomposite.

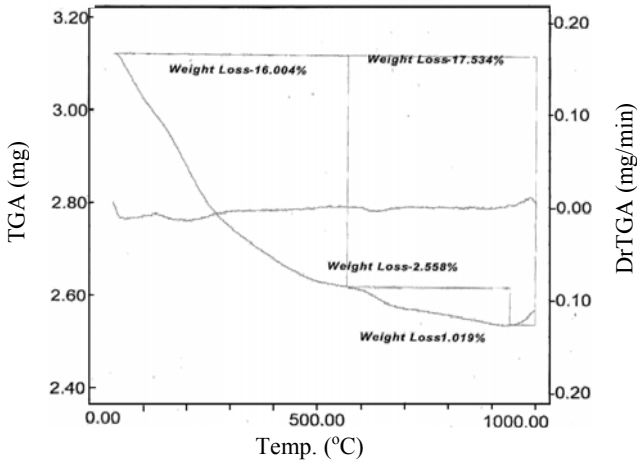


Fig. 8 TG/DTA of (nCePf)/polyiondole nanocomposite.

product was formulated as: $Ce(HPO_4)_2 \cdot (PInd)_x \cdot 2.1\ H_2O$., where, x = ~ 7.0%.

4. Conclusions

Novel supported nanofibrous cerium phosphate/polyindole nanocomposite membrane was prepared via in-situ chemical oxidation of the monomer that was promoted by the reduction of Ce(IV) ions present in the inorganic matrix. The presence of Ce(IV) ions allows redox reactions necessary to oxidati.ve polymerization to occur. The self-supported sheet integrity is preserved. This result is interesting because the shape integrity makes the building of molded conducting device possible. The formulation of the fibrous cerium phosphate nanocomposite was supported by thermal, elemental (C, H, N) analysis, FT-IR spectrum and SEM. The degree of polymer loading can be controlled by varying aging time.

Acknowledgements

To Department of Chemistry, Faculty of Science, Tripoli University, for providing facilities for this research, to Yarmouk University, Jordan, for providing TEM analysis facilities, to Geol. Adel Bayuomi, Institute of Mineral Resources, Cairo, Egypt for providing facilities for TGA, SEM analysis.

References

[1] Freund, M. S.; Deore, B. A. *Self Doped Conducting*

Polymers; John Wiley and Sons, 2007.

[2] Kucheldorf, H. R.; Luken, O.; Swift, G. *Handbook of Polymer Synthesis;* CRC Press, 2010.

[3] Banerjee, S.; Tayagi, A. K. *Functional Materials: Preparation, Proscessing and Applications;* Elsevier, 2012.

[4] Cai, Z.; Grang, M.; Tang, Z. Novel Battery Using Conducting Polymers and Polyaniline. *J. of Mater. Sci.* **2004,** *39,* 4001-400.

[5] Billand, B.; Maarouf, E.; Hamecant, E. An Investigation of Electrochemically and Chemically Polymerized Polyindole. *Mater. Rech. Bull.* **1994,** *29,* 1239.

[6] Fajan, A.; Been, B. Structural and Optical Properties of Polyindolemanganese Oxide Nanocomposite. *Indian J. of Adv. In Chem. Sci.* **2013,** *2,* 95-96.

[7] GiFajan, A.; Beribabu, K.; Manegand, R.; Sinesh, R.; Vijaialakchmi, L.; Stephen, A.; et al. Polyindole Nanowires: Synthesis, Characterization and Electrochemi Sensing Properties. *Chem. Sci. Trans* **2013,** *2,* S13-S16.

[8] Tuker, T.; Yazich, B.; Erbil, M. The Use of Polyindole for Preventing Copper Corrosion. *Surf. Coat. Technol.* **2006,** *200,* 4802-4809.

[9] Eraldemir, O.; Sari, B.; Gok, A.; Unal, H. I. Synthesis and Characterization of Polyindole/Poly (Vinylactate) Conducting Composities. *Journal of Macromol. Sci. A* **2008,** *45,* 205-211.

[10] Trung,V. Q.; Huyen, D. N.; Synthesis, Properties and Application of Polyindole/TiO_2, Asean Work Shop on Advanced Materials Science and Nanotechnology. *J. of Physics, Conferences Seriec* **2009,** *187,* 012058.

[11] Zhijiang, C.; Guang, Y. Synthesis Polyindole and Its Evaluation for Li-ion Battery Applications. *Synth. Met.* **2010,** *160,* 1902-1905.

[12] Dosio, S. T.; Mert, B. D.; Yazicch, B. Polyidole Top Coat on TiO_2 for Corrosion Protection of Steel. *Corrosion Sci.* **2013,** *66,* 51-58.

[13] Rejani, P.; Beena, B. Structural and Optical Properties of Polyindole-Mamganese Oxide Nanocomposite. *Ind. J. of Adv. Chem. Sci.* **2013,** *2,* 95-99.

[14] Clearfield, A. *Inorganic Ion Exchange Materials;* CRC Press Fl.: Bocca Raton, 1988.

[15] Colon, J. L.; Diaz, A.; Clearfeild, A. Nanoincapsulation of Insulin into Zirconium Phosphate for Oral Delivery Applications. *Biomacro Molecules* **2010,** *9,* 2465.

[16] Diaz, A.; Saxena, V.; Gunzalez, J.; David, A.; Casanas, B.; Carpenter, C.; et al. Zirconium Phosphate Nano-Platelets: A Novel Platform for Drug Delivery in Cancer Therapy. *Chem. Commun.* **2012,** *48,* 1754.

[17] Tushato, M.; Danjo, M.; Baba, Y.; Murakom, M.; Nana, H. Preparation and Chemical Properties of a Novel Layered Cerium(IV) Phosphate. *Bulletin of Chem. Soc Jap.* **1997,** *70,* 143.

[18] Salvado, M. A.; Pertierra, P.; Tropajo, C.; Garcia, G. R. Crystal Structure of Cerium (IV) Bis (Hydrogen Phosphate Derivative. *J. Am. Chem. Soc.* **2007,** *129,* 10970.

[19] Alberti, G.; Costantino, U. Recent Progress in the Field of Synthetic Inorganic Exchanger Having a Layered and Fibrous Structure. *J. Chromatogr.* **1974,** *102,* 5.

[20] Parangi, T.; Wani, P.; Chudasama, U. Synthesis, Characterization and Application of Cerium Phosphate. *Desalination and Water Treatment* **2012,** *38,* 126.

[21] Romano, R.; Alves, O. S. Fibrous Cerium(IV) Phosphate Host of Weak and Strong Lewis Bases. *Inclus. Phenom. and Macrocyclic* **2005,** *51,* 211.

[22] Casciola, M.; Costantino, U.; Damico, S. Conductivity of Cerium(IV) Phosphate in Hydrogen Form. *Solid State Ionics* **1988,** *28,* 617.

[23] Varsheny, K. G.; Tayal, N.; Gupta, P.; Agrawal, A.; Drabik, M. Synthesis, Ion-Exchange and Physical Studies on Polystyrene Cerium(IV) Phosphate Hybrid Fibrous Ion Exchanger. *Ind. J. of Chem.* **2004,** *43,* 2586.

[24] Metwally, S. S.; El-Gammal, B.; Ali, H. F.; Abo-EL-Enein, S. A. Removal and Separation of Some Radionuclides by Poly-Acrylamide Based Ce(IV) Phosphate. *Separation Sci. and Tech.* **2011,** *46,* 11.

[25] Alberti, G.; Casciola, M.; Captani, D.; Donnadio, A.; Narducci, R.; Pica, M.; et al. Novel Nafion-Zirconium Phosphate Composite Membranes with Enhanced Stability of Proton Conductivity. *Electrochemica Acta* **2007,** *52,* 8125.

[26] Yang, Y.; Liu, C.; Wen, H. Preparation and Properties of Polyvinyl Alcohol/Exfoliated α-Zirconium Phosphate. *Polym. Test.* **2009,** *28,* 185.

[27] Nagarale, R. K.; Shin, W.; Singh, P. K. Progress in Ionic Organic-Inorganic Composite Membranes for Fuel Cell Application. *Polym. Chem.* **2010,** *1,* 388.

[28] Shakshooki, S. K.; Elejmi, A. A.; Khalfulla, A. M.; Elfituri, S. S. *Int. Conf. on Mater. Imperative* **2010,** *11,* 49-70.

[29] Feng, Y.; He, W.; Zhang, X.; Jia, X.; Zhao, H. The Preparation of Nanoparticle Zirconium Phosphate. *Mater. Letters* **2007,** *61,* 3258.

[30] Bao, C.; Gua, Y.; Song, L.; Lu, H.; Yuan, B.; Hu, Y. Facile Synthesis of Poly (Vinyl Alcohol)/α-Titanium Phosphate Nanocomposite with Markedly Enhanced Properties. *Ind. Eng. Chem. Res.* **2011,** *50,* 11109.

[31] Verissimo, C.; Alves, O. L. Preparation of the Conducting Nanocomposites Using Molded Inorganic Matrix: Fibrous Cerium Phosphate as a Self Supported Pyrrole Polymerization. *J. Mater. Sci.* **2003,** *13,* 1378-1383.

[32] Salomaki, M.; Rasanan, M.; Leiro, J.; Huti, T.; Tenho, M.; Lukkari, J.; et al. Oxidative Inorganic Multilayer for Polypyrrole Film Generation. *Adv. Funct. Mater.* **2010,** *20,* 2140-2147.

[33] Shakchooki, S. K.; El-Akari, F. A.; El-Fituri, M. S.; El-Fituri, S. S. Fibrous Cerium(IV) Hydrogen Phosphate Membrane Self Supported Benzimidazole Polymerization Agent. *Adv. Mater. Res.* **2014,** *856,* 3.

[34] Gribabu, K.; Manigandan, R.; Ljalakshmi, L.; Suregh, R.; Stephen, A.; Narayanan, V. Polyindole Nanowires; Characterization and Chemical Sensing Properties. *Chem. Sci. Trans.* **2013,** *2(S1),* S13-S16.

J. Chem. Chem. Eng. 8 (2014) 385-389

Synthesis and Study of Heteronuclear Citrates

Nani Bidzina Zhorzholiani*, Iamze Alim Beshkenadze, Maia Avtandil Gogaladze and Givi Tengiz Begheluri

Petre Melikishvili Institute of Physical and Organic Chemistry, Ivane Javakhishvili Tbilisi State University, Tbilisi 0186, Georgia

Received: March 08, 2014 / Accepted: April 01, 2014 / Published: April 25, 2014.

Abstract: Terms of synthesis were determined for creation of new generation premixes and for their testing in experiments. Heteronuclear chelate citrates of general formula: $M^{I}_{2}M^{II}L_{2}\cdot nH_{2}O$ (where, M^{I} = Zn, Co, Fe, Mn, Cu; M^{II} = Mn, Zn, Co, Cu; n = O/4) were synthesized. Identity and composition of synthesized compounds were defined by microelemental analysis, determination of melting temperature and X-ray diffraction analysis. X-ray diffraction method was used also to define crystallinity of the compounds and their citric acid (H_4L) component. X-ray amorphous and iso-structural orders were also revealed.

Key words: Bio-metals, chelate compounds, microelemental analysis, X-ray diffraction analysis.

1. Introduction

Even the most primitive forms of live organisms are unable to provide vital processes without participation of bio-metals. In optimal doses they are able to affect actively growth and development, propagation, productivity, resistance of organisms to diseases. Investigations of researchers prove that bio-metals play active role in the physiological and biological processes going on in poultry and animals. Up to 75 chemical elements are found in their organisms and namely this conditioned the interest shown to the so-called “vital metals” by wide specter of researchers. We considered five microelements (Zn, Co, Fe, Mn, Cu), because these microelements belong to a number of very critical and essential for life elements that animal organisms have. They play an important role in a water and organic compounds metabolism, absorbtion and utilization of nutrients. They generateoptimal conditions for the normal function of many organs including cardiac muscule and nervous system [1-4]. Their role and significance are exemplified by the fact that one of the main factors which defines low quantity and quality indices of foodstuff is the deficiency of bio-metals in plants, soil, as well as in agricultural animals and poultry. Decisive role in the resolution of this problem is attributed to the provision of live organisms with optimal quantity and ratio of microelements. Since bio-metals in live organisms fulfill their functions in the form of chelates, at filling up of deficit in bio-metals in the form of chelates, we observe sharp increase in their biological activity [5-8].

*Corresponding author: Nani Bidzina Zhorzholiani, Association Professor, research fields: inorganic and coordination chemistry. E-mail: nanizhorzholi@gmail.com.

2. Materials and Methods

For synthesis, we used the following original compounds: ZnO, $MnCO_3$, $CoCO_3Co(OH)_2$, $CuCO_3Cu(OH)_2$, $Fe(CH_3COO)_2\cdot 4H_2O$, and important for vital processess oxyacid-citric acid (H_4L). Composition of compounds and their identity were defined by well-known methods: microelemental analysis (CHN Analyser, Labertherm GmbH). Purity was determined by melting temperature measuring (Dynalon SMP10) and X-ray diffraction method on DPOH-3Mtype diffractometer, at copper anode emission. The same method was used to define their crystallinity, and X-ray amorphous and iso-structural orders were also revealed.

3. Results

Investigations are continued at the Laboratory of

Problems Agrarian Chemistry for creation of new generation premixes and for their testing in experiments [9-17]. With this in view heteronuclear chelate citrates of the following general formula:

$M^I_2 \cdot M^{II} \cdot L_2 \cdot nH_2O$ (where, M^I = Zn, Co, Fe, Mn, Cu; M^{II} = Mn, Zn, Co, Cu; n = O/4) were created. To obtain these citrates, we take a mix: (1) $ZnO:MnbCO_3$, (2) $CoCO_3Co(OH)_2:ZnO$, (3) $CuCO_3Cu(OH)_2:CoCO_3Co(OH)_2$, (4) $CoCO_3Co(OH)_2:MnCO_3$, (5) $CoCO_3Co(OH)_2:CuCO_3Cu(OH)_2$, (6) $Fe(CH_3COO)_2 \cdot 4H_2O:MnCO_3$, (7) $Fe(CH_3COO)_2 \cdot 4H_2O:ZnO$, (8) $Fe(CH_3COO)_2 \cdot 4H_2O:CoCO_3Co(OH)_2$ and (9) $MnCO_3:CuCO_3Cu(OH)_2$ at 2:1 molar ration on porcelain cup, crush intensely till it is reduced to fine dispersion condition, then we add citric acid dissolved in minimal volume of hot water. We observe intense isolation of CO_2 and changes of color. The obtained solutions are left at room temperature till the next day, are filtered and the residue after its washing by ether is dried on air.

Identity and composition of synthesized chelate composites: $Zn_2 \cdot Mn \cdot L_2 \cdot 2H_2O$, $Co_2 \cdot Zn \cdot L_2$, $Cu_2 \cdot Co \cdot L_2 \cdot H_2O$, $Fe_2 \cdot Mn \cdot L_2 \cdot 2H_2O$, $Co_2 \cdot Mn \cdot L_2 \cdot 4H_2O$, $Co_2CuL_2 \cdot 4H_2O$, $Mn_2CuL_2 \cdot 4H_2O$, $Fe_2ZnL_2 \cdot 2H_2O$ and $Fe_2CoL_2 \cdot 4H_2O$ were defined by microelemental analysis (Table 1), by melting temperature detection (Table 2), by X-ray diffraction method (Table 3).

We also defined their crystallinity and revealed X-ray amorphous and iso-structural orders by X-ray diffraction analysis.

Table 3 represents the results of relative intensities (I/I_0), reflection angle (2θ), inter-plane distances (d) obtained by deciphering of X-ray diffraction patterns of the composites.

4. Discussions

X-ray diffraction studies did not reveal presence of starting compounds in the samples in the form of separate phase. Therefore, we can conclude that

Table 1 Results of microelemental analysis of chelates.

#	Formula	Practical (%)				Theoretical (%)			
		M^I	M^{II}	C	H	M^I	M^{II}	C	H
1	$Zn_2 \cdot Mn \cdot L_2 \cdot 4H_2O$	20.94	9.05	24.03	2.15	21.69	9.17	24.00	2.34
2	$Co_2 \cdot Zn \cdot L_2$	20.87	10.72	25.09	2.17	21.01	11.58	25.66	2.49
3	$Cu_2 \cdot Co \cdot L_2 \cdot H_2O$	22.11	9.96	24.45	1.91	21.81	10.12	24.73	2.06
4	$Co_2 \cdot Mn \cdot L_2 \cdot 4H_2O$	19.03	8.73	20.96	2.72	18.91	8.83	21.11	2.89
5	$Co_2 \cdot Cu \cdot L_2 \cdot 4H_2O$	18.21	9.79	22.75	2.63	18.66	10.05	22.79	2.85
6	$Fe_2 \cdot Mn \cdot L_2 \cdot 2H_2O$	19.33	9.14	24.62	2.15	19.27	9.46	24.77	2.41
7	$Fe_2 \cdot Zn \cdot L_2 \cdot 2H_2O$	19.15	11.13	24.79	2.23	18.94	10.99	24.35	2.37
8	$Fe_2 \cdot Co \cdot L_2 \cdot 4H_2O$	17.78	8.93	22.98	2.65	18.03	9.49	23.18	2.89
9	$Mn_2 \cdot Cu \cdot L_2 \cdot 4H_2O$	17.17	10.09	22.97	2.77	17.63	10.18	23.08	2.89

Table 2 Results of measurements of composites melting temperatures.

#	Formula	Melting, T (^oC)	Color
1	$Zn_2 \cdot Mn \cdot L_2 \cdot 4H_2O$	> 286	White
2	$Co_2 \cdot Zn \cdot L_2$	> 286	Lilac
3	$Cu_2 \cdot Co \cdot L_2 \cdot H_2O$	> 286	Dark light-blue
4	$Co_2 \cdot Mn \cdot L_2 \cdot 4H_2O$	> 286	Grey-lilac
5	$Co_2 \cdot Cu \cdot L_2 \cdot 4H_2O$	> 286	Dark lilac
6	$Fe_2 \cdot Mn \cdot L_2 \cdot 2H_2O$	> 286	Mustard yellow
7	$Fe_2 \cdot Zn \cdot L_2 \cdot 2H_2O$	> 286	Light brown
8	$Fe_2 \cdot Co \cdot L_2 \cdot 4H_2O$	> 286	Grey-brown
9	$Mn_2 \cdot Cu \cdot L_2 \cdot 4H_2O$	> 286	Light green

Table 3 Results of X-ray diffraction analysis of chelate composites and citric acid.

H_4L			1. $Zn_2{\cdot}Mn{\cdot}L_2{\cdot}4H_2O$			2. $Co_2{\cdot}Zn{\cdot}L_2$			3. $Cu_2{\cdot}Co{\cdot}L_2{\cdot}H_2O$		
2θ	d	J/J_0	2θ	d	J/J_0	2θ	d	J/J_0	2θ	d	J/J_0
11.5	0.3	2.5	10.66	8.301	0.0608	8.500	8.152	1.1696	10.89	8.120	0.2350
15.2	4.5	37.5	11.49	7.699	0.0043	11.37	7.782	0.0393	12.31	7.187	0.1800
17.0	1.6	13.3	11.93	7.419	0.0530	12.27	7.214	0.2606	13.30	6.656	0.1033
18.3	6.5	54.2	12.09	7.323	0.2286	13.32	6.645	0.1818	14.53	6.096	0.0100
19.0	0.4	3.3	13.06	6.778	0.0156	15.72	5.636	0.0909	15.81	5.605	1.0000
22.3	4.5	37.5	15.52	5.711	0.0486	15.83	5.599	0.2545	17.20	5.157	0.0866
23.1	12.0	100.0	15.50	5.717	0.0660	16.66	5.322	0.0303	18.41	4.820	0.0533
23.8	0.5	4.2	16.20	5.473	0.0173	17.23	5.147	0.0787	19.39	4.577	0.0683
24.5	1.0	8.3	16.93	5.238	0.0269	18.47	4.803	0.0484	19.86	4.470	0.2166
27.1	0.5	4.2	18.23	4.865	0.0026	20.03	4.434	1.0000	21.77	4.083	0.1316
28.8	0.4	3.3	19.38	4.579	0.0382	20.34	4.367	0.3454	22.82	3.896	0.0350
29.4	2.5	20.8	19.8	4.484	1.0000	20.67	4.298	0.0636	23.17	3.839	0.1533
30.8	1.5	12.5	20.13	4.411	0.0376	21.70	4.095	0.0757	23.72	3.751	0.0933
32.7	1.5	12.5	20.57	4.318	0.0339	21.75	4.085	0.1151	24.66	3.611	0.0816
33.5	0.8	6.7	21.39	4.155	0.0921	22.36	3.976	0.0515	25.44	3.502	0.1183
37.0	1.0	8.3	22.78	3.904	0.0269	22.90	3.881	0.1181	26.82	3.373	0.2483
41.9	0.5	4.2	23.51	3.784	0.0113	23.81	3.737	0.0818	28.15	3.170	0.0433
45.8	0.5	4.2	24.09	3.695	0.1052	24.31	3.661	0.0575	28.97	3.082	0.1216
56.8	0.5	4.2	24.4	3.648	0.0113	24.69	3.606	0.0303	30.44	2.937	0.0600
			24.62	3.615	0.0147	26.54	3.358	0.2696	30.90	2.893	0.1316
			26.07	3.418	0.0400	28.79	3.101	0.1242	31.81	2.813	0.0650
			28.58	3.123	0.0800	29.41	3.035	0.0151	33.93	2.642	0.1050
			29.24	3.056	0.0756	29.99	2.979	0.0878	35.49	2.529	0.0516
			29.76	3.002	0.0939	31.07	2.879	0.2424	37.31	2.410	0.0350
			30.32	2.948	0.0182	31.89	2.806	0.1515	40.36	2.235	0.0466
			31.36	2.852	0.0313	32.43	2.761	0.0575			
			32.25	2.775	0.0521	34.37	2.609	0.0424			
			34.88	2.572	0.0252	35.87	2.503	0.0454			
			35.64	2.512	0.0800	38.56	2.335	0.0181			
			37.34	2.408	0.0443	40.26	2.240	0.0545			
			38.77	2.323	0.0243	40.58	2.223	0.0424			
			40.23	2.242	0.0104	42.22	2.190	0.0606			
			40.39	2.233	0.0260						
			41.05	2.199	0.0330						
			42.91	2.107	0.0252						
			43.56	2.078	0.0269						
			43.70	2.072	0.0339						
			44.64	2.030	0.0313						
			45.49	1.994	0.0034						
			46.10	1.969	0.0243						
			46.19	1.965	0.0078						
			47.41	1.918	0.0365						
			48.15	1.890	0.0313						
			48.07	1.893	0.0495						
			49.2	1.852	0.0269						

Table 3 continued

4. $Co_2{\cdot}Mn{\cdot}L_2{\cdot}4H_2O$			5. $Co_2{\cdot}Cu{\cdot}L_2{\cdot}4H_2O$			6. $Fe_2{\cdot}Zn{\cdot}L_2{\cdot}2H_2O$			7. $Mn_2{\cdot}Cu{\cdot}L_2{\cdot}4H_2O$		
2θ	d	J/J_0	2θ	d	J/J_0	2θ	d	J/J_0	2θ	d	J/J_0
10.70	8.267	0.0636	9.800	9.024	0.0645	6.67	13.247	1.0000	9.02	9.804	0.3888
11.75	7.532	0.0454	10.84	8.160	0.1612	7.18	12.295	0.5714	10.77	8.213	0.5000
13.17	6.725	0.0606	12.28	7.206	0.1612	8.44	10.466	0.1428	12.30	7.196	0.1611
14.27	6.208	1.0000	15.49	5.719	0.0645	8.86	9.978	0.2857	13.10	6.760	0.2388
14.84	5.968	0.0666	15.77	5.619	1.0000	10.87	8.133	0.6642	13.70	6.461	0.1111
15.61	5.677	0.0909	17.07	5.193	0.0645	13.41	6.601	0.4285	13.74	6.445	0.0916
17.02	5.210	0.0303	18.30	4.847	0.0967	14.34	6.175	0.2000	14.57	6.079	0.2500
17.83	4.974	0.0939	19.77	4.488	0.1612	14.96	5.920	0.3214	15.58	5.688	0.7138
18.39	4.824	0.4121	23.12	3.845	0.2580	17.01	5.211	0.2000	16.79	5.279	0.0722
18.70	4.744	0.2303	23.28	3.820	0.1459	17.98	4.933	0.2857	16.93	5.236	0.2666
20.42	4.348	0.3333	24.62	3.616	0.0967	19.49	4.553	0.1785	18.15	4.888	0.2500
21.50	4.133	0.1333	25.36	3.511	0.1451	19.99	4.440	0.5000	18.22	4.870	0.1222
21.61	4.110	0.3272	26.25	3.394	0.0645	20.63	4.303	0.1428	19.64	4.520	0.1611
23.20	3.833	0.2303	27.48	3.245	0.0032	21.66	4.101	0.1785	20.21	4.393	0.1027
23.59	3.772	0.1939	28.31	3.151	0.0516	22.46	3.958	0.1785	21.43	4.147	0.3055
23.90	3.723	0.1393	29.30	3.047	0.0258	23.35	3.808	0.1428	21.83	4.072	0.2146
24.65	3.612	0.0575	31.00	2.884	0.1290	26.99	3.303	0.1428	22.47	3.957	0.0833
25.90	3.440	0.1606	31.49	2.840	0.0870	27.11	3.288	0.1785	23.44	3.795	0.1500
26.96	3.307	0.2303	34.5	2.599	0.0645	30.77	2.906	0.1214	26.01	3.426	0.5000
27.74	3.216	0.0606	37.41	2.404	0.0645	40.59	2.222	0.2142	28.77	3.103	0.1666
28.70	3.111	0.1666	42.00	2.120	0.0419	46.04	1.971	0.1214	30.24	2.955	0.4166
29.98	2.980	0.1515				48.95	1.861	0.1428	31.59	2.832	0.2547
31.74	2.819	0.1000				55.10	1.666	0.1571	31.70	2.823	0.0962
32.64	2.795	0.1763							33.10	2.706	0.1166
33.91	2.662	0.1536							33.56	2.671	0.1611
35.86	2.504	0.1667							34.84	2.575	0.1777
35.87	2.503	1.393							35.78	2.510	0.1666
36.55	2.458	0.0787							36.87	2.438	0.1444
38.12	2.361	0.0515							37.32	2.409	0.1166
42.46	2.129	0.0939							39.85	2.262	0.2222
43.21	2.094	0.1333							41.36	2.183	0.0527
44.18	2.050	0.1288							43.67	2.073	0.1666
47.45	1.916	0.1060							46.43	1.956	0.1611
48.27	1.885	0.0303							47.94	1.898	0.1388
49.08	1.856	0.0606									

absolutely new individual compounds are obtained which are in full conformity with the results of the above given micro elemental analysis and melting point measurements (Tables 1 and 2).

X-ray diffraction patterns of the composites $Fe_2{\cdot}Mn{\cdot}L_2{\cdot}H_2O$ and $Fe_2{\cdot}Co{\cdot}L_2{\cdot}4H_2O$ are characterized by weakly expressed diffuse peaks, therefore they represent X-ray-amorphous compounds. Other compounds are characterized by clearly expressed crystalline structures, various relative intensities (I/I_0), reflection angles (2θ), and definite intra-spatial distance (d) values. It should be stated that X-ray diffraction patterns of the composites $Cu_2{\cdot}Co{\cdot}L_2{\cdot}H_2O$ and $Co_2{\cdot}Cu{\cdot}L_2{\cdot}4H_2O$ are identical, which speaks of their iso-structure that is conditioned by analogousness of their chemical composition and geometrical characteristics of crystalline structure, which can not be said about the composites: $Zn_2{\cdot}Mn{\cdot}L_2{\cdot}2H_2O$, $Co_2{\cdot}Zn{\cdot}L_2$, $Co_2{\cdot}Mn{\cdot}L_2{\cdot}4H_2O$, $Mn_2{\cdot}Cu{\cdot}L_2{\cdot}4H_2O$, $Fe_2{\cdot}Zn{\cdot}L_2{\cdot}2H_2O$ (Table 3).

5. Conclusions

For the first time, we synthesized Heteronuclear chelate citrates of general formula: $M^{I}_2M^{II}L_2 \cdot nH_2O$ by using modified and simplified methods. We studied identity and composition of synthesized compounds, determined their crystallinity, and revealed X-ray amorphous and iso-structural orders.

We have conducted preliminary studies on these synthesized compounds as new poultry premixes. Based on good preliminary data, we concluded to conduct large-scale studies in this direction.

Acknowledgments

We thank Science & Technology Center in Ukraine and ShotaRustaveli National Science Foundation. The work was implemented with the support of Science & Technology Center in Ukraine Project Proposal #5461 and ShotaRustaveli National Science Foundation Grant #30/06.

References

[1] Tanatarov, A. B. Mineral Elements in Biology and Their Use in Medicine and Agriculture. *Moscow* **1986,** *3,* 358.

[2] Kalashnikov, A. P.; Fisinin, V. I.; Scheglev, V. V. *Norms and Rations in the Feeding of Agricultural Animals;* Moscow, 2003; p 456.

[3] Menkin, V. K. *The Feeding of Animals;* Moscow, 2003; p 360.

[4] Draganov, I. F.; Buryakova, M. A. *Working Program of Teaching Discipline "Essentials of Research in Agricultural Animals";* Timiryazeva, 2006; p 13.

[5] Dobrinina, N. A. *Biological Chemistry;* Lomonosov Moscow State University: Moscow, 2007; p 36.

[6] Ribkina, T. I. *Biological and Toxic Impact of Chemical Elements and Their Inorganic Compounds on Human Organism;* Novomoskovsk, 1999; p 92.

[7] Dobrinina, N. A. *Bioinorganic Chemistry;* Moscow, 2007; p 36.

[8] Lebedev, S. V.; Miroshnikov, S. A.; Sukhanova, O. N.; Rakhmatullin, S. G.; Malyishin, E. N.; Sipailova, O. Y.; et al. Method for Increase of Productivity of Chicken-Broilers. Patent 2,370,095, Oct. 20, 2010.

[9] Beshkenadze, I. A.; Tsitsishvili, V. G.; Urotadze, S. L.; Gogaladze, M. A.; Zhorzholiani, N. B. In *Natural Zeolites and Biometal-Containing Compozites,* Proceedings of Materials of IV International Conference Sorbents as Factors of Life Quality and Health, Belgorod, Sept 24-28, 2012.

[10] Beshkenadze, I. A.; Gogaladze, M. A.; Zhorzholiani, N. B.; Urotadze, S. L.; Burkiashvili, N. O.; Gogua, L. D. Synthesis of the Chelates Containing Amino Acids and Citric Acid for Creation of New Generation Premixes. *Annals of Agrarian Science* **2013,** *11(2),* 84-86.

[11] Beshkenadze, I.; Gogaladze, M.; Zhorzholiani, N. *Chemical Admix to Poultry Fodder;* National Center for Intellectual Property of Georgia: Tbilisi, 2000.

[12] Beshkenadze, I.; Gogaladze, M.; Zhorzholiani, N. *Chemical Admix to Poultry Fodder;* National Center for Intellectual Property of Georgia: Tbilisi, #P4917, 2008.

[13] Beshkenadze I., Zhorzholiani N., Gogaladze M. *Chemical Admix to Poultry Fodder;* National Center for Intellectual Property of Georgia: Tbilisi, #P4918, 2008.

[14] Beshkenadze, I.; Zhorzholiani, N.; Gogaladze, M. Chelate-Containing Chemical Admix for Poultry Feeding; 2013.

[15] Kozmanishvili, A.; Beshkenadze, I.; Zhorzholiani, N. *Chemical Editions for Rabbit Food Ration;* Bulletin of the Academy of Agricultural Sciences of Georgia: Tbilisi 2003.

[16] Beshkenadze, I.; Gogaladze, M.; Zhorzholiani, N. Synthesis of the Chelates Continuing Amino Acids and Citric Acid for Creation of New Generation Premixes. *Annals of Agrarian Science* **2013,** *11(2),* 84-86.

[17] Tsintsadze, G.; Beshkenadze, I.; Mestiashvili, N.; Zhorzholiani, N. In *Physical-Chemical Investigation of* $M^{I}M^{II}L \cdot nH_2O$ *Heteronuclear Citrates,* Proceedings of the Georgian Academy of Sciences, 2006.

J. Chem. Chem. Eng. 8 (2014) 390-394

Influence of Technological Operations in the Dissolved Oxygen Content of Wines

Ana Catarino[1], Sandra Alves[2] and Helena Mira[1*]

1. Polytechnic Institute of Santarém. Escola Superior Agrária de Santarém, Department of Food Technology, Biotechnology and Nutrition, Quinta do Galinheiro-S. Pedro 2001-904, Santarém

2. Esporão, S.A. Herdade do Esporão, 7200-999 Reguengos de Monsaraz

Received: February 10, 2014 / Accepted: February 28, 2014 / Published: April 25, 2014.

Abstract: Oxygen plays a crucial role in oenology. The oxygen leads to changes in the chemical and sensory profile of wines. On one hand, the impact of moderate oxygen exposure of red wine has a positive effect in its colour, aromatic bouquet and mouth-feel properties. On the other hand, oxygen has a negative effect on white wine's quality, as well as the sensory and compositional levels. The purpose of this study was to quantify the dissolved oxygen in red and white wine, during different cellar operations such as racking, tartaric stabilization, filtering and bottling. The techniques that contribute most to the enrichment of oxygen in wine are: cold tartaric stabilization (2.29 mg/L, white wines), bottling (1.38 mg/L red wines and 1.11 mg/L white wines) and bag-in-box filling (2.47 mg/L red wines; 2.22 mg/L white wines). After identifying the most critical technical operations in wine making, preventive and corrective measures had to be taken to reduce the dissolved oxygen content of wines, as well as preventing their depreciation.

Key words: Wine, oxygen, oxidation, dissolution.

1. Introduction

Oxygen exists as a gaseous element representing 20.9% of earth atmosphere, under standard temperature and pressure, and it is indispensable for the majority of the living organisms.

The oxygen plays a crucial role in enology. Louis [1] had already noted that oxygen could be a great enemy of wine or wine making.

Oxygen can dissolve in wine at several stages during winemaking, bottling and aging. It plays a beneficial role during the winemaking process: in promoting yeast multiplication, in the maturation and stabilization of wine colour, in the removal of the reduced compounds taste, and attenuation of the vegetable character, etc.. However, when the wine is exposed to excessive amounts of oxygen, it can have negative effects such as the promotion of the growth of unfavourable microorganisms in wine (acetic bacteria, *Brettanomyces*), the degradation of colour and the production of organoleptic defects, etc..

The oxidation in white wine causes important sensory alterations in the colour and the aroma. The browning is characterized by progressive darkening which can be globally characterized by absorbance at 420 nm [2]. The oxygen induces a loss of freshness and fruitiness, and develops an unpleasant oxidized character, which is generally described as non-desirable flavours of "honey-like", "boiled-potato", "cooked vegetable", "farm-feed" and "woody-like" [3-7].

Phenolics compounds are the main oxidation substracts. Various researchers have studied the impact of oxygen exposure on the polyphenolic composition of red wines [8-10]. Some controlled and continuous O_2 is introduced into red wine (micro-oxygenation) to improve wine quality, such as colour stability and intensity, softening of astringent

*Corresponding author: Helena Mira, Professor Adjunto, research fields: wine, fruits and vegetables, postharvest. E-mail: helena.mira@esa.ipsantarem.pt.

tannins, and decreases reductive and vegetative aromas.

During winemaking, the different unit operations may integrate some oxygen from the atmosphere into the wine. The operations such as pumping, transport, racking, centrifugation, stabilization, filtration and bottling have been studied by various authors [11-17].

Various researchers have monitored the dissolved oxygen of wine at bottling and during storage and the influence of packaging in wine conservation [3, 6, 10, 13, 14, 17-19].

The Esporão SA is one of the biggest wineries in Portugal. The purpose of this study was to quantify the dissolved oxygen in red and white wine, during different oenological treatments such as racking, tartaric stabilization, filtering and bottling, to identify the critical points (the unit operations) that contribute most to the integration of oxygen in wine and to establish preventive and corrective measures.

2. Experiments

2.1 Wines

The white or red wines analyzed were produced during 2010 vintage in Esporão S.A. (Alentejo) from different varieties (Arinto, Antão Vaz, Perrum; Moreto, Trincadeira e Castelão, Touriga Nacional, Cabernet Sauvignon, among other). All wines were obtained following the usual winemaking processes.

2.2 Wine Treatments

Red and white wines were submitted to specific oenological treatments (Table 1) with systems, equipment and procedures commonly used in winery. The increase of dissolved oxygen (O_{diss}) was calculated as the difference between the oxygen concentration measured before (O_{bef}) and immediately after (O_{aft}) each treatment ($O_{diss} = O_{aft} - O_{bef}$).

2.3 Measurement of Dissolved Oxygen

The measurement of dissolved oxygen was carried out using a portable oxímeter Crison OXI 45 P.

2.4 Statistical Procedures

(1) Data of the increase of dissolved oxygen are expressed as the average and standard deviation of measurements performed for the different wines.

(2) The influence of oenological treatments was analyzed by non-parametric procedures by the paired-samples *T*-test (before and after treatment), with the Wilcoxon signed ranks test, using the SPSS statistics software (Version 17.0).

3. Results and Discussion

The level of dissolved oxygen at a given time in the wine depends on the dissolution and consumption kinetics. When applied to a wine movement (pumping, filling and stirring) the kinetics of oxygen dissolution is higher than the consumption by the wine's compounds. Dissolved oxygen reacts with the constituents of the wine and disappears gradually, reaching very low levels.

After racking, the evolution of dissolved oxygen consumption in the wine was monitored over time (Fig. 1). It was found that the kinetics of consumption varied depending on the type of wine, having been noted that the white wine kinetics were slower than the red wines kinetics. Red wines consume oxygen faster than white wines because of its constitution of phenolic compounds. In the case of red wines, in just four days phenolic compounds consumed more than half of dissolved oxygen. For white wines, it took more than 30 days. Increasing temperature increases the kinetics of dissolved oxygen consumption.

The monitoring of oxygen concentrations before and after specific oenological treatments provided data on the levels of enrichment of the winery and its variability.

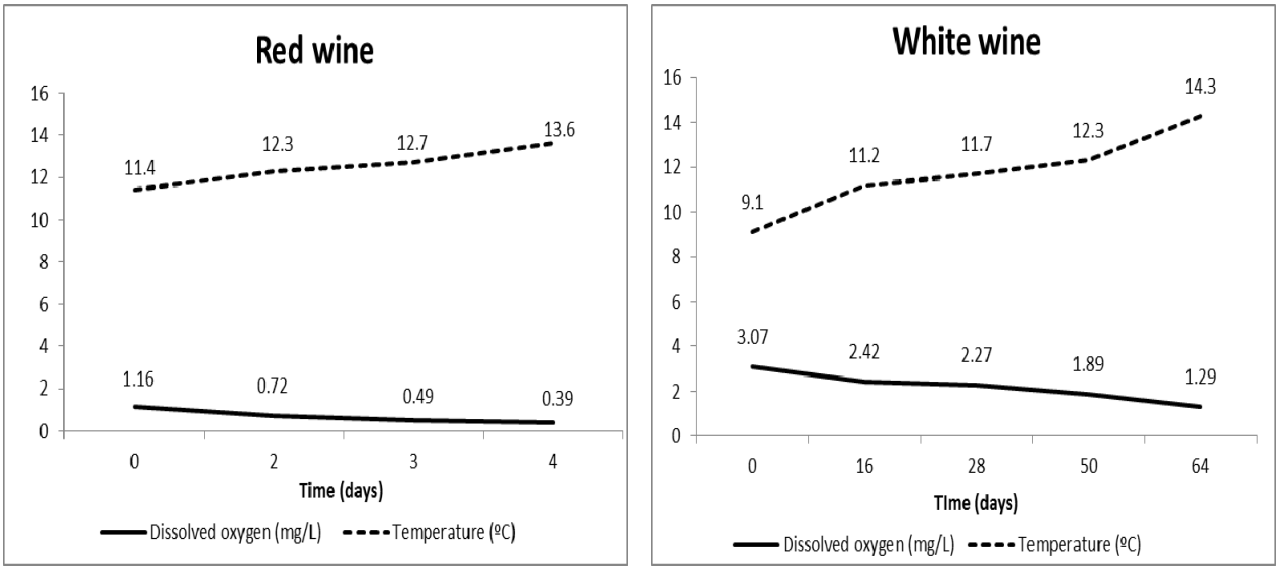
Statistical analysis performed using nonparametric paired samples revealed that the enrichment in dissolved oxygen is significant for all operations performed (Table 2).

The increase of dissolved oxygen for each treatment is shown in Table 3.

Table 1 Description of oenological treatments.

White wine	*n*	Red wine	*n*
Protein stabilization (bentonite addition)	4	Racking (bottom-bottom)	110
Continuous tartaric stabilization (cooling method)	12	Tartaric stabilization (metatartaric acid addition)	12
Filtration (membrane cartridges, nominal porosity 1-0.45 μm)	29	Tangential filtration	47
Bottling (glass bottles)	28	Bottling (glass bottles)	147
Packaging (bag-in-box, 5 L)	9	Packaging (bag-in-box, 5 L)	26

n = number of analysed wines.



(a) (b)

Fig. 1 Evolution of dissolved O_2 in wine after racking: (a) red wine, (b) white wine.

Table 2 The average content of dissolved oxygen (mg/L), before and after each oenological treatment and *p*-value of Wilcoxon signed ranks test.

	Oenological treatment	Before treatment	After treatment	*p*-value (Wilcoxon test)
Red wine	Racking	0.19 ± 0.12	0.65 ± 0.34	0.000
	Tartaric stabilization	0.28 ± 0.25	0.38 ± 0.26	0.002
	Tangential filtration	0.14 ± 0.49	0.40 ± 0.33	0.000
	Bottling (glass bottles)	0.49 ± 0.42	1.87 ± 0.93	0.000
	Packaging (bag-in-box)	0.98 ± 0.28	3.45 ± 0.86	0.000
White wine	Protein stabilization	1.22 ± 0.85	1.35 ± 0.89	0.042
	Cold tartaric stabilization	0.60 ± 0.37	2.89 ± 1.80	0.008
	Filtration (membrane cartridges)	0.20 ± 0.17	0.71 ± 0.16	0.000
	Bottling (glass bottles)	0.67 ± 0.24	1.78 ± 0.42	0.000
	Packaging (bag-in-box)	0.65 ± 0.22	2.87 ± 0.96	0.008

Racking increased the dissolved oxygen content by on average of 0.46 mg/L, exceeding that observed [11, 15]. The oxygen enrichment in the racking occurs essentially at the beginning and end of the transfer, due to the dissolution of air contained in the pipes and tanks. The racking should be performed bottom to bottom of the tanks, and it uses inert gas in the pipes and tanks before starting the transfer process [13, 14].

For the tartaric stabilization of red wine, metatartaric acid was added just prior to bottling. The homogenization of the wine was achieved with nitrogen. The addition of the metatartic acid leads to an increase of 0.10 mg/L of dissolved oxygen, which is a reduced amount when compared to the cold tartaric stabilization.

Table 3 Increase of dissolved oxygen (mg/L) in each oenological treatment.

	Oenological treatment	O_2D (mg/L) (mean ± standard deviation)
Red wine	Racking	0.46 ± 0.31 (n = 110)
	Tartaric stabilization	0.10 ± 0.06 (n = 12)
	Tangential filtration	0.26 ± 0.30 (n = 47)
	Bottling (glass bottles)	1.38 ± 0.49 (n = 147)
	Packaging (bag-in-box)	2.47 ± 0.93 (n = 26)
White wine	Protein stabilization	0.13 ± 0.05 (n = 4)
	Cold tartaric stabilization	2.29 ± 1.78 (n = 12)
	Filtration (membrane cartridges)	0.51 ± 0.18 (n = 29)
	Bottling (glass bottles)	1.11 ± 0.47 (n = 28)
	Packaging (bag-in-box)	2.22 ± 0.77 (n = 9)

The important enrichment that occurred during cold tartaric stabilization of the white wines was on average 2.21 mg/L (Table 3), and these results are consistent with data found by other authors [12, 13, 15]. The sharp temperature drop caused an increase in the oxygen dissolution rate, therefore, it is important to protect the wine from the oxygen in the operation.

The protein stabilization of white wine by the addition of bentonite showed a small enrichment in dissolved oxygen. It was noted that this operation did not contribute a lot to the increase of dissolved oxygen in the wine, similar to what was observed for the tangential filtration of red wines, in which the dissolved oxygen was lower than that reported by Vidal et al. [11, 13].

The filtration by membrane cartridges increased the dissolved oxygen content mainly due to air inlets in the circuit, in particular through the pipe connections, the pump and filter body. The dissolved oxygen in wine is higher than that reported in Refs. [11, 13, 15], these authors noted average values of 0.10 mg/L and 0.06 mg/L, respectively. This is due to the length and the diameter of the tubing as well as the turbulent flow, which influences the kinetics of oxygen dissolution.

Unlike the results of Vidal et al. [13, 14], filling in BIB (bag-in-box) has contributed to a greater enrichment in dissolved oxygen than bottling. This is due to a problem with an inertized filling machine used to fill BIB containers. To reduce the risk of wine oxidation in BIB, the concentration of SO_2 was increased up to a maximum of 50 mg/L, (1 mg/L oxygen oxidizes 4 mg/L SO_2), so that the SO_2 protects the wine from oxidation and browning [19].

Bottles were filled using a filling machine inertized with nitrogen. However, this operation was responsible for some increase in dissolved oxygen content, both in white wine and in red wine. These results are in agreement with those previously described [13, 14, 18]. The filling is the main critical point for wine enrichment in oxygen.

4. Conclusions

The rationalization of the operating conditions and the reasonable use of neutral gases, especially at the beginning and the end of operation, are necessary to control and decrease significantly the oxygen pick up in all the operations.

The most important enrichments occur especially during the operations of cold tartaric stabilization and during the bottling and packaging, especially if no protection is taken to protect the wine from the oxygen in the air.

Controlling the oxygen ingress during filling (bottle or BIB) is an important way of improving the quality and the shelf-life of wine.

Acknowledgments

The authors thank Esporão S. A. for the means for carrying out this work.

References

[1] Pasteur, L. *Studies on Wine: Its Diseases, Causes, New Methods to Conserve and for Aging;* Printed by Royale: Paris, 1873; p 264.

[2] Singleton, V. L. Oxygen with Phenols and Related Reactions in Musts, Wines and Model Systems: Observations and Practical Implications. *American Journal of Enology and Viticulture* **1987,** *38,* 69-77.

[3] Escudero, A.; Asensio, E.; Cacho, J.; Ferreira, V. Sensory and Chemical Changes of Young White Wines Stored under Oxygen as Assessment of the Role Played by Aldehydes and Some Other Important Odorants. *Food Chemistry* **2002,** *77,* 325-331.

[4] Silva, F. A. C.; Guedes, P. P.; Rodrigues, P.; Hogg, T. Kinetics of Oxidative Degradation of White Wines and How They Are Affected by Selected Technological Parameters. *Journal of Agricultural and Food Chemistry* **2002,** *50,* 5919-5924.

[5] Silva, F. A. C.; Hogg, T.; Guedes, P. P. Identification of Key Odorants Related to the Typical Aroma of Oxidation-Spoiled White Wines. *Journal of Agricultural and Food Chemistry* **2003,** *51,* 1377-1381.

[6] Lopes, P.; Silva, M. A.; Pons, A.; Tominaga, T.; Lavigne, V.; Saucier, C.; et al. Impact of Oxygen Dissolved at Bottling and Transmitted through Closures on the Composition and Sensory Properties of a Sauvignon Blanc Wine during Bottle Storage. *Journal of Agricultural and Food Chemistry* **2009,** *57,* 10261-10270.

[7] Karbowiak, T.; Gougeon, R. D.; Alinc, J. B.; Brachais, L.; Debeaufort, F.; Voilley, A.; et al. Wine Oxidation and the Role of Cork. *Critical Reviews in Food Sciences and Nutrition* **2010,** *50,* 20-52.

[8] Atanasova, V.; Fulcrand, H.; Cheynier, V.; Moutounet, M. Effect of Oxygenation on Polyphenol Changes Occuring in the Course of Wine-Making. *Analytica Chimica Acta* **2002,** *458,* 15-27.

[9] Toit, W. J.; Marais, J.; Pretorius, I. S.; Toir, M. Oxygen in Must and Wine: A Review. *South African Journal of Enology and Viticulture* **2006,** *27(1),* 76-91.

[10] Wirth, J.; Morel-Salmi, C.; Souquet, J. M.; Dieval, J. B.; Aagaard, O.; Vidal, S.; et al. The Impact of Oxygen Exposure before and after Bottling on the Polyphenolic Composition of Red Wines. *Food Chemistry* **2010,** *123,* 107-116.

[11] Vidal, J. C.; Dufourcq, T.; Boulet, J. C.; Moutounet, M. Oxygen Contributions during Treatments of the Wines Assessment of the Observations on Site 1. *French Review of Oenology* **2001,** *190,* 24-31.

[12] Vidal, J. C.; Boulet, J. C.; Moutounet, M. Oxygen Contributions during Treatments of the Wines Assessment of the Observations on Site 2. *French Review of Oenology* **2003,** *201,* 32-38.

[13] Vidal, J. C.; Boulet, J. C.; Moutounet, M. Oxygen Contributions during Treatments of the Wines Assessment of the Observations on Site 3. *French Review of Oenology* **2004,** *205,* 25-33.

[14] Vidal, J. C.; Boulet, J. C.; Moutounet, M. Comparison of Methods for Measuring Oxygen in the Headspace of a Bottle of Wine. *Journal International des Sciences de la Vigne et du Vin* **2004,** *38(3),* 191-200.

[15] Castellari, M.; Simonato, B.; Tornielli, G. B.; Spinelli, P.; Ferrarini, R. Effects of Different Enological Treatments on Dissolved Oxygen in Wines. *Italian Journal of Food Science* **2004,** *16(3),* 387-396.

[16] Valade, M.; Tribaut-Sohier, I.; Bunner, D.; Pierlot, C.; Moncomble, D.; Tusseau, D. Oxygen Contributions in Wine Making and Their Impacts on the Wines—The Particular Case of Champagne 1. *French Review of Oenology* **2006,** *221,* 1-8.

[17] Valade, M.; Tribaut-Sohier, I.; Bunner, D.; Laurent, M.; Moncomble, D.; Tusseau, D. Oxygen Contributions in Wine Making and Their Impacts on the Wines—The Particular Case of Champagne 2. *French Review of Oenology* **2007,** *222,* 17-28.

[18] Vidal, J. C.; Moutounet, M. Monitoring of Oxygen in the Gas and Liquid Phases of Bottles of Wine at Bottling and during Storage. *Journal International des Sciences de la Vigne et du Vin* **2006,** *40(1),* 35-45.

[19] Ghidossi, R.; Poupot, C.; Thibon, C.; Pons, A.; Darriet, P.; Riquier, L.; et al. The Influence of Packaging in Wine Conservation. *Food Control* **2012,** *23(2),* 302-311.

J. Chem. Chem. Eng. 8 (2014) 395-399

Purification of Bromelain Enzyme from Curauá (*Ananaserectifolius LB Smith*) White Variety, by Aqueous Two-Phase System PEG 4000/Potassium Phosphate

Juliana Ferrari Ferreira, Dalva Sbruzzi, Kleber Vânio Gomes Barros, Daniela Diniz Ehrhardt and Elias Basile Tambourgi*

Department of Engineering of Chemical Systems, School of Chemical Engineering, State University of Campinas, Campinas 500, Brazil

Received: March 21, 2014 / Accepted: April 08, 2014 / Published: April 25, 2014.

Abstract: The Curauá (*Ananaserectifolius LB Smith*) is a species belonging to the family *Bromeliaceae*. Occurs in the states of Para, Amazonas, Amapá, Acre, Mato Grosso and Goiás, has two varieties, purple and white, and its fibers are used in automotive and textile industries due to its strength, softness and lightweight. Currently, only the fiber is used in industry, the rest is considered waste. However, this residue contains compounds with important properties to be discovered and studied. An enzyme complex found in this residue is bromelain, a group of proteolysis' enzymes with application in several areas such as in the food, pharmaceutical and cosmetics industries. Today, its use is aiming the pharmaceutical industry, the production of ointments, gels, creams and lotions because they offer a wide range of therapeutic efficacies: antiedemas, anti-inflammatory, antithrombotic and fibrinolytic activities. This work studied the enzyme purification and recovery presented in the leaves of Curauá by means of an ATPS (aqueous two-phase system) PEG 4000/potassium phosphate. The protein content was measured by Bradford reagent and the enzymatic activity was measured by the Biuret reagent. Batch assays were performed aiming the enzyme extraction and recuperation, using the partition coefficient as indicator. It was used pH 7.0, 8.0 and 9.0, varying the proportional composition between the polymeric and the saline phases (tie-lines). The white variety of Curauá was used. The best purification factor was 4.53 and about 113.04 μg/mL of total protein measured by Bradford.

Key words: Curauá, purification, bromelain.

1. Introduction

Enzymes are organic molecules present in cells of living organisms, with the specific function of catalyzing chemical reactions. The enzyme starts increasing velocity of a chemical reaction by acting as a catalyzer [1]. A catalyzer does not modify the balance of a reaction, however, it reduces the amount of energy required to make the reaction to happen.

Economically viable, the use of enzymes in various industrial sectors has been increasing over the years [2-3]. Among enzymes with industrial use, the bromelain stands out due to its diversity in applications: leather processing in textile industries; softening fibers and detergent production [4]; in food industry providing meat softening [5]; and in breweries it is used to purify beers hydrolyzing tannin-protein complexes produced during fermentation [5].

Bromelain is also used in the pharmacological research area due to its anti-inflammatory effect [6] and its potential to help treating health problems such as angina, indigestion and breathing problems [7]. In

*Corresponding author: Elias Basile Tambourgi, Associate Professor/Ph.D., research field: protein purification. E-mail: tambourgieb@gmail.com.

therapies against cancer, it is used to increase lysis of cancer cells [8].

Curauá (*Ananaserectifolius*) is a little known and studied species. Its cultivation started at Lago Grande de Curuaí, city of Santarém in Para state, and has been expanding to other regions of the same state. Researches have shown that Curauá fiber presents excellent quality, being compared to fiberglass due to its resistance, softness and low weight [9, 10]. In automotive industry, it has been used to produce sunshade for trucks [11].

Currently, the separation and purification process of bioproducts is a very important segment for industries, as it can represent from 80% to 90% of the production cost. Therefore, the development of an efficient and low cost process is highly relevant [12].

The liquid-liquid extraction has been arousing interest as an intermediate separation step that either replaces more expensive methods of separation or reduces the number of separation steps required by the process. This separation process is based on the distribution of the solute between the phases and partial miscibility of the liquids [13].

The liquid-liquid extraction process consists of transferring a substance from a liquid mixture to another immiscible (or partially miscible) liquid phase by putting them in contact. This process is widely used in chemical and pharmaceutical industries, such as in the recovery of antibiotics or organic acids from fermentation broths.

Nevertheless, the application in the purification of proteins is still limited mainly due to the possibility of protein denaturation if in contact with organic solvents, yielding a useless product [14-17]. The ATPS (aqueous two-phase systems) are created by the addition of aqueous solutions of two hydrophilic polymers such as PEG (polyethylene glycol) and dextran or a polymer and a salt, such as PEG and potassium phosphate.

These substances provide the appropriate and convenient method for extracting substances of biological origin, as the formation of phases between 70% and 90% of water provides a bland environment to work with biologically active compounds, preserving their molecular stability and thus, allowing their processing on this medium [18].

The pH in the medium, besides influencing in the maintenance of enzymatic activity, also affects the charge distribution on the surface of the protein. Thus, adjusting the pH of the medium to values close to the IP (isoelectric point) of the protein (pH value where the molecule presents electric charge near zero), the effects that act over the partition in ATPS are reduced [19].

Ferreira [20] analyzed the purification of the bromelain enzyme extracted from the stem of the pineapple (*Ananascomosus*) in ATPS (aqueous two-phase system) PEG/potassium phosphate and got better results using polyethylene glycol 4000, rather than polymer with lower molecular weight (PEG 1500).

Thus, this work had as objective obtaining PF (purification factors) of the bromelain enzyme derived from white variety of Curauá (*Ananaserectifolius LB Smith*) through the ATPS PEG 4000/potassium phosphate.

2. Materials and Methods

PEG with molecular weight of 4000 was obtained from Sigma (Switzerland). Milli-Q-quality distilled water was used. Potassium hydrogen phosphate, comassie brilliant blue G, di-sodium hydrogen phosphate, sodium hydroxide were obtained from Synth (São Paulo, Brazil).

The following equipments were used: Mars electronic scale AL 200; an Arno multiprocessor; pH meter Analyser pH 300; thermostatic bath FANEM; automatic micropipettes and spectro-photometer UV/VIS Spectronic 21D.

The concentration values of PEG and phosphate for each tie line were reproduced according to Ref. [20].

Curauá's leaves were collected from field at São Manoel Experimental Farm in Botucatu, São Paulo. Upon arriving on lab, they were washed with distilled

water, dried with paper towel and stored in plastic bags, refrigerated until use.

2.1 Samples Preparation

Buffer and Curauá's leaves were weighted in 1:1 proportion; then, they were grinded using a high efficiency multiprocessor and the extract was filtered using nylon filter removing fibers and other present particles.

2.2 Preparation of Reactive Biuret

It was dissolved in 500 mL of distilled water, 1.5 g of copper pentahydrate and 6.0 g of tartarate of sodium and potassium sulphate, and it was added 300 mL sodium hydroxide solution 10% under constant agitation, and finally added distilled water for a 1 L solution.

2.3 Determination of Bromelain Activity

In order to determine the activity of bromelain, we used the Biuret reagent and a solution to 5 g/L BSA (bovine serum albumin), this method is based on the reaction of the reactive Biuret, consisting of a mixture of copper and sodium hydroxide with a complexing that stabilizes copper in solution. Readings were taken in a spectrophotometer at 540 nm, and finally calculated the enzymatic activity, according to Eq. (1).

$$AE = \frac{Vreactor(l)\times 10^6(\mu\frac{mol}{l})}{MM_{BSA}\times V_{enzyme}(ml)\times time_{reaction}(\text{min})} \quad (1)$$

where, $V_{reactor}$ is the reactor volume; MM_{BSA} is the molar mass of PEG and V_{enzyme} is the enzyme volume used for the analysis.

Total protein in samples of bottom and top phases were determined by the Bradford method [21].

2.4 Preparation of Buffers

Buffer solutions were prepared in pH 7.0, 8.0 and 9.0, from a solution of mono potassium phosphate dibasic to 15% (w/w).

For this, it was prepared standard solutions of monobasic potassium phosphate (solution A) and bibasic potassium phosphate (solution B) mixing them into a beaker containing silver chloride electrode for measuring the pH, until the desired pH.

2.5 Determination of the Purification Factor

To calculate the *PF* it was used the Eq. (2).

$$PF = \frac{EA}{EA_{crude}} \quad (2)$$

where, EA_{crude} is crude enzymatic activity (U) and *EA* is enzymatic activity of top and bottom phase.

3. Results and Discussions

Tables 1-3 demonstrate the influence of the pH and the concentration of the PEG 4000/potassium phosphate system regarding the purification of the bromelainenzyme derived from white variety of Curauá.

The ATPS that presented better result in the purification of the bromelain enzyme derived from white Curauá was the PEG 4000/potassium phosphate system in pH 7.0 ("tie line" 2 and 3); the PEG 4000/potassium phosphate system in pH 9.0 ("tie line" 1, 2 and 3) also presented considerable values.

These results are based on the values of enzymatic activity and purification factor.

Analyzing the behavior of the three "tie lines" of the ATPS PEG 4000/potassium phosphate in pH 7.0,

Table 1 Partition of the bromelain enzyme derived from leaves of white Curauá using the ATPS PEG 4000/potassium phosphate in pH 7.0.

Tie line		Proteins (μg/mL)	*EA* (U)	*PF*
1	Top phase	18.73	0.004	2.81
	Bottom phase	32.57	0.004	2.82
2	Top phase	22.02	0.006	3.70
	Bottom phase	35.75	0.006	3.80
3	Top phase	30.62	0.007	4.53
	Bottom phase	54.72	0.007	4.29

Table 2 Partition of the bromelain enzyme derived from leaves of white Curauá using the ATPS PEG 4000/potassium phosphate in pH 8.0.

Tie line		Proteins (μg/mL)	*EA* (U)	*PF*
1	Top phase	21.64	0.004	1.36
	Bottom phase	47.88	0.004	1.30
2	Top phase	22.23	0.008	2.23
	Bottom phase	37.74	0.006	1.84
3	Top phase	32.32	0.005	1.41
	Bottom phase	87.74	0.004	1.28

Table 3 Partition of the bromelain enzyme derived from leaves of white Curauá using the ATPS PEG 4000/potassium phosphate in pH 9.0.

Tie line		Proteins (μg/mL)	*EA* (U)	*PF*
1	Top phase	35.39	0.008	2.39
	Bottom phase	113.04	0.007	2.23
2	Top phase	28.97	0.008	2.47
	Bottom phase	74.14	0.008	2.42
3	Top phase	30.65	0.007	2.22
	Bottom phase	68.16	0.008	2.31

it is possible to notice the increasing trend of the purification factors as the length of the mooring lines increases; however, the ATPS PEG 4000/potassium phosphate in pH 8.0presented the inverse behavior; higher values for the purification factors were obtained in lower concentrations of the components of the system.

Sbruzzi [22] showed in her study about the costs of this process (ATPS), using the fiber of curauá, purple and white variations, and the estimated sale price, showing its economic viability, whether it is for use as a pre-process in traditional chromatographic systems or direct commercialization, as an alternative for the bromelain of pineapple.

4. Conclusions

The values of the purification factor of the bromelain enzyme derived from white Curauá were affected by concentrations of the polymeric and saline phases, as well as by the pH value in the medium.

The best result was obtained working with the lowest pH studied in this work but with highest polymeric concentration (“tie line” 2 and 3) of the ATPS PEG 4000/potassium phosphate.

The technique of the aqueous two-phase PEG 4000/potassium phosphate systems proved being promising in the purification of the bromelain enzyme derived from the white variety of the Curauá.

It can be used to extract this proteolytic enzyme during the extraction of the white Curauá from automotive industry, for instance, maximizing profit, reducing environmental impact and the waste.

Acknowledgments

The authors gratefully acknowledge the scholarship received from CNPq, FAPESP and the financial support from CAPES/PROEX (Brazil).

References

[1] Said, P. R. *Enzymes for Industrial and Biotechnological Interest.* Publisher Events, 2002.

[2] Forgaty, W. M.; Kelly, C. T. *Topics in Enzyme and Fermentation, Biotechnology;* J. Wiley&Sons: Chichester, 1979.

[3] Wiseman, A. *Handbook of Enzyme Biotechnology;* John Wiley Sons: New York, 1987.

[4] Santos, S. A. Effect of Time on the Physico-Chemical, Chemical Composition and Stem Bromelain in Pineapple *Ananascomosus* (L) Merr Activity. CV. Pearl Stored under Conditions with and without Cooling, Mines. *Food Science, Lavras: ESAL* **1995,** *47*.

[5] Freiman, L. O. The Advancements in the Use of Bromelain in the Area of Food and Health. *Food and*

Nutrition Magazine **2001,** *12,* 215-226.

[6] Mattos, P. E. O. Clinical Validation of Supplementation for Athletes Bromelain. UNIFESP 2005.

[7] Cesar, A. C. W. Economic Feasibility Analysis of a Case of Extraction and Purification of Bromelain Pineapple. Unicamp, School of Chemical Engineering, 2005.

[8] Meinig, G. E. *Bromelain Phytomedicine* **1999,** *2,* 1-2.

[9] Leão, A. L.; Tan, I. H.; Craschi, J. C. In *Curaua Fiber-A Tropical Natural Fibers from Amazon-Potential and Application in Composites,* Proceedings of International Conference on Advanced Composites, Hurghada, Egito, 1998.

[10] Frollini, E.; Leão, A. L.; Mattoso, L. H. S. Natural Polymers and Agrofibers Composites. Botucatu, Brazil, U. S. Patent 2000.

[11] Mothé, C. G. Use of Computer Program Coupled with Thermal Analysis Techniques for Determination of Kinetic Parameters of Composites Curauá PU/Fiber. *Analytica Magazine* **2003,** *4,* 12.

[12] Belter, P. A.; Cussler, E. L.; Hu, W. S. *Bioseparations: Downstream Processing for Biotechnology;* John Wiley&Sons: Minneapolis, 1988.

[13] Rabelo, A. P. B.; Tambourgi, E. B.; Pessoa, J. A. Bromelainpartioning in Two Phase Aqueous Systems Containing PEO-PPO-PEO Block Copolymer. *J. Chrom. B*. **2004,** *807,* 61-68.

[14] Aires-Barros, M. R.; Taipa, M. A.; Cabral, J. M. S. Isolation and Purification of Lipases. In *Lipases: Their Structure, Biochemistry and Application;* Wooley, P., Petersen, S. B., Eds.; Cambridge University Pres.: Great Britain, 1994; pp 234-270.

[15] Albertsson, P. A. *Partition of Cell Particles and Macromolecules;* John Willey: New York,1996.

[16] Matiasson, B.; Kaul, R. Use of Aqueous Two-Phase Systems (ATPs) for Recovery and Purification in Biotechnology. In *Separation, Recovery, Purification and Biotechnology;* American Chemical Society, 1986; pp 79-92.

[17] Zaslasvsky, B. Y. *Aqueous Two-Phase Partitioning-Physical Chemistry and Bioanalytical Applications;* Inc. New York: Mercel Dekker, 1995.

[18] Coimbra, J. S. R. *Performance of a Puller Type Grasser in Separating the Whey Proteins Using Aqueous Two-Phase Systems;* Unicamp: School of Food Engineering, 1995.

[19] Forciniti, D.; Hall, C. K.; Kula, M. R. Protein Partition at the Isoeletric Point: Influence of Polymer Molecular Weight and Concentration and Protein Size. *Biotechnology and Bioengineering* **1991,** *38,* 986-994.

[20] Ferreira, J. F. *Characterization and Purification of the Enzyme Bromelain in Aqueous Two-Phase PEG/Phosphate System;* Unicamp: School of Chemical Engineering, 2007.

[21] Bradford, M. M. A Rapid and Sensitive Method for the Quantization of Microgram Quantities of Protein Utilizing the Principle of Protein-Dye Binding. *Anal. Biochem*. **1976,** *72,* 248-254.

[22] Sbruzzi, D. *Economic Viability of Bromelain Purification from Curaua Using an Aqueous Two Phase System PEG/Phosphate;* Unicamp: School of Chemical Engineering, 2010.

J. Chem. Chem. Eng. 8 (2014) 400-407

Microbiological Treatment of Effluent for Zinc Hydrometallurgical Plant

Ashish Kumar*, Krishna Deo Sharma and Sunil Duggal
Central R&D Laboratory, Hindustan Zinc Limited, Udaipur 313024, India

Received: December 20, 2013 / Accepted: January 07, 2014 / Published: April 25, 2014.

Abstract: Sulfate reducing bacteria were isolated from the soil sample of Roaster-Acid unit of Debari Zinc Smelter of Hindustan Zinc Ltd., India and were adapted for effluent water of Zinc hydrometallurgy plant to sustain zinc concentration of about 500 ppm and iron concentration of about 160 ppm with high acidity (pH < 1.0). Nutrient broth, whey, ethanol and sucrose were tested as carbon source for SRB (sulfate reducing bacteria) out of which whey was found as the best electron donor to expedite the rate of biological treatment with SRB. A two stage anaerobic bioreactor was developed with a treatment capacity of 30 L effluent water in 4 days. The concentration of heavy metals in the treated water was within the permissible limits. The suggested methodology generates no solid waste, is environment friendly and may be commercially implemented for treatment of zinc plant effluent.

Key words: Sulfate reducing bacteria, anaerobic treatment, isolation, hydrometallurgy effluent.

1. Introduction

Industrial wastewaters especially originating from acid mine drainage and hydrometallurgical industries contain high concentration of heavy metals as sulfates with free acidity. The improper treatment and/or discharge of this acidic water can have serious environmental impacts and can unbalance sulfur cycle [1]. Conventionally, the effluent water is being neutralized with lime followed by alum flocculation. The method is expensive and results in high total dissolved solids in treated water along with generation of residual sludge, which is dumped in SLF (secured land fill) sites and needs a large capital expenditure resulting in permanent loss of fertility of costly land. Membrane separation is also being used as an alternative route in effluent treatment to reduce solid waste load. However, relatively high cost of frequent membrane replacement and energy consumption restricts commercial use of this technique [2]. Recently, biotechnology has shown new opportunities and challenges in many sectors especially in environmental remediation of industrial wastes (solid/liquid) to achieve better environment management and pollution control.

Present research is conducted with an aim of in-situ precipitation of heavy metals as metal sulfides from effluent of zinc hydrometallurgical plant. The advantage of sulfide precipitation include: better water quality due to lower solubility of metal sulfides compared with their corresponding hydroxides; selective precipitation of high grade metal sulfide concentrates that can be reprocessed to earn revenue; reduction in sludge volume; and toxicity and opportunities in reagent saving. A better overall environment solution can be attained due to metal recycle and effective solid-liquid separation. Under anaerobic conditions, SRB (sulfate-reducing bacteria) oxidize simple organic compounds completely to CO_2 by utilizing sulfates as electron acceptor and generate sulfides and alkalinity [3]. SRB utilize a number of volatile fatty acids and hydrogen as electron donors to expedite its activity [4]. These sulfides subsequently precipitate metals as metal sulfides in in-situ

*Corresponding author: Ashish Kumar, Manager (Technology Development), research field: non-ferrous metallurgy. Email: ashish.be@gmail.com.

conditions with saving of costly reagents like lime and sodium sulfide. Metal sulfides can also be precipitated using biogenic H_2S in ex-situ conditions [5, 6]. Hybrid H_2S bioreactor concept has also been introduced by controlling methanogenic reactions of typical anaerobic sludge reactor [7]. In case of anaerobic bacteria, sulfates are the main source of H_2S production and its concentration results in major impact on SRB growth [8]. SRB consumes approximately one to two moles of protons per mole of sulfate that is reduced and produces approximately two equivalents of alkalinity per mole of reduced sulfate [9]. The electron accounting can be made by assuming complete oxidation of organic compounds [5]. SRB are notable for their end product, hydrogen sulfide, which is far more noticeable substance than sulfates due to its chemical properties and physiological effects [10]. SRB could be carbon limited in organic medium containing cow manure and saw dust since these materials are largely polymers of cellulose and hemicellulose, which are insoluble organic matters [11, 12].

This paper includes isolation, screening and adaptation of SRB from hydrometallurgical smelter of Hindustan Zinc Limited at Udaipur in India. Evaluation of culture performance on bioreactor of 30 L effluent treatment capacity has also been analyzed and discussed.

2. Experimental Materials and Methods

2.1 Effluent Water

Effluent water from DZS (Debari Zinc Smelter) was collected in sealed poly vinyl containers and the heavy metals were analyzed by Atomic Absorption Spectrophotometer (Varian 220), while acidity and sulfates were analyzed by conventional titrimetry and gravimetric methods. The analysis of untreated (collected from DZS) and treated effluent (anaerobic bioreactor) is shown in Table 1.

2.2 Isolation and Selection of SRB

To isolate SRB, soil samples were collected from different locations of DZS of Hindustan Zinc Ltd. The locations were: roaster, acid plant, effluent plant, oxidation pond, cow dung sample and concentrate storage yard. The samples were serially diluted for 10^{-10} dilutions with proper mixing and poured in Petridishes filled with Postgate media [13] using agar as solidifying medium. The sterile conditions were maintained throughout the activities. Petridishes were incubated under anaerobic conditions at 30 ^{o}C for 48 h. The anaerobic conditions in the chamber were maintained by creating vacuum and filling it with N_2 gas. The sterility inside incubation chamber was maintained by cleaning the chamber with ethanol and further N_2 gas was passed through air filter.

Table 1 Chemical analysis of untreated and treated effluent.

Elements	Untreated effluent (collected from DZS)	Treated effluent (using anaerobic bioreactor)
	Concentration	Concentration
Zn	440 ppm	4.8 ppm
Cu	1 ppm	< 0.5 ppm
Fe	160 ppm	1.8 ppm
As	1 ppm	< 0.5 ppm
Sb	< 1 ppm	< 0.5 ppm
Mn	20 ppm	< 0.5 ppm
Cd	30 ppm	< 0.5 ppm
Ni	1 ppm	< 0.5 ppm
Pb	5 ppm	< 0.5 ppm
SO_4^{2-}	8.76 gpl	0.26 gpl
Acidity	4.40 gpl	pH = 6.8

Developed bacterial colonies were streak plated and incubated under anaerobic conditions for 48 h. The streak plating was repeated five times to screen the anaerobic SRB. All experiments were conducted in triplicates (45 sets for each step) to isolate the purer SRB culture. The screened colonies were inoculated separately in sealed flasks containing Postgate media and incubated under anaerobic conditions. The maximum grown cultures were taken out (minimum one from each collection site) and TSI (triple sugar iron) test was conducted to confirm the activity of isolates. Selection of SRB was done by ascertaining its efficiency towards sulfate reduction in ten times diluted effluent water of Debari Zinc Smelter. 400 mL of this diluted effluent was taken in 500 mL conical flasks and inoculated with respective strains (10% v/v). The flasks were incubated for twenty days and sulfates were analyzed on alternate days. This was done to supplement the conclusion drawn from TSI test for selection of SRB. The batches were named as Ctrl, St 1, St 2, St 3, St 4, St 5 and St 6 for control (inoculated with methanol in place of bacterial strain), roaster, acid plant, ETP (effluent treatment plant), cow dung, oxidation pond ETP and concentrate storage locations.

2.3 Adaptation of SRB

Selected SRB was developed in Postgate media and was used as inoculum for acclimatization with DZS effluent. DZS effluent was diluted for ten times in a way so that the effluent and nutrient broth (Postgate media) ratio can be maintained as 8:2 (v/v). 400 mL of diluted effluent was taken in to 500 mL conical flasks and was inoculated (10% v/v) with isolated SRB culture separately. Sterile N_2 gas was purged into each conical flask to expel the dissolved oxygen out. The flasks were sealed and incubated for 20 days. This treated effluent was further used as inoculum for diluted DZS effluent and similar procedure was followed for the raw effluent. Flasks were harvested on alternate days and were analyzed for zinc, Iron & pH. The treatment of effluent without dilution was repeated two times to acclimatize bacteria and after which samples were analyzed daily.

2.4 Microorganism

Best-acclimatized culture was named as SRB-CRDL and was maintained in Postgate media under anaerobic conditions. The strain was subcultured at every 20 days.

2.5 Selection of Carbon Source as Electron Donor

It was essential to observe the effect of electron donor as well as selection of its cheaper source since; SRB could mediate sulfate reduction to a greater degree when simple carbon and energy sources were available to catalyze the reactions [9]. Nutrient broth (2:8), whey (1:9), ethanol (1:9) and sucrose (1:9) were used as carbon source in effluent water. SRB-CRDL was inoculated separately in 500 mL sealed conical flasks and flasks were incubated in the similar fashion after purging sterile N_2 as discussed earlier. The flasks were harvested for every alternate day and were analyzed for zinc, iron, manganese, lead, cadmium and pH value. The data collected was used not only for selection of electron donor but also for optimization of days for maximum heavy metals removal and to later design the size of the bioreactors.

2.6 Semi Batch Type Anaerobic Bioreactors

Two-stage semi batch type bioreactors were installed to increase the treatment capacity of the system. In first stage, two bioreactors of 10 L capacity were run for 4 days and 5 L from each was then transferred to another anaerobic bioreactor of equal capacity for second stage treatment, while first stage bioreactors were again leveled up with fresh effluent. The liquid streams were transferred through peristaltic pumps under anaerobic and sterile conditions. The experimental set up was continued for more than 30 days. In steady state conditions total, 30 L effluent was treated in 4 days.

3. Results and Discussion

3.1 Isolation and Selection of SRB

The results of TSI test for isolated bacterial strains are given in Fig. 1 and Table 2 which shows that the SRB strain isolated from Acid Plant of Debari Zinc Smelter is the best out of the strains isolated from other places. Fig. 2 shows sulfate reduction in ten times diluted effluent water using different isolated cultures. After 20 days of microbiological treatment, experiment confirms that the strain isolated from Acid Plant is the best out of other strains. This supports the result concluded by TSI test. The bacterial strain collected from the Roaster-Acid soil was more adaptable for sulphate ions and hence, it provided the best results in terms of sulphates reduction from the effluent.



Fig. 1 TSI test.

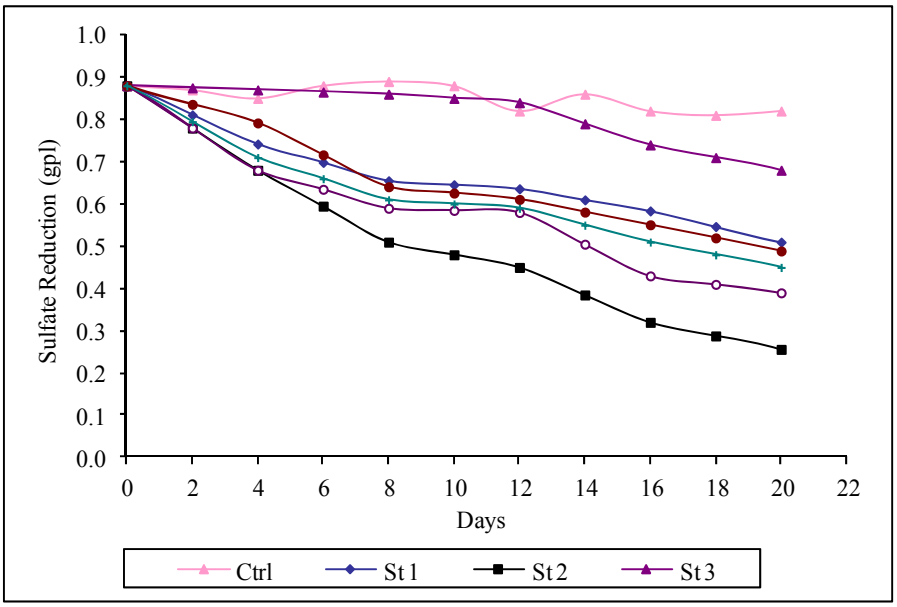


Fig. 2 Reduction in sulfate concentration in ten times diluted DZS effluent w.r.t. different strains.

Table 2 Analysis of TSI test.

Strain isolate No.	Ctr l	St 1	St 2	St 3	St 4	St 5	St 6	Remarks
Strain collection place	Control	Roaster	Acid Plant	ETP (effluent treatment plant)	Cow dung	Oxidation pond ETP	Concentrate storage	
Glucose fermentation	X	√√	√√	√	√√	√	√	Red color turns yellow in butt
Lactose/sucrose fermentation	X	X	√	√	X	√	X	Red color turns yellow on slant
H_2S gas production	X	√	√√	X	√√	√	√	Blackish color in butt after yellow
Gas production (H_2/CO_2)	X	X	√	X	X	X	X	Creaks or shifting of slant

3.2 Adaptation of SRB

Fig. 3 represents the adaptation graph of the selected SRB. The adaptation was started with 10 times dilution for 20 days while second peak in the graph is for 5 times dilution batch and was run for another 20 days, which is followed by adaptation of SRB without any dilution of effluent water. The similar experiment is repeated for two more times. After 92 days of adaptation experiments, the bacteria were adapted to reduce heavy metals concentration in acidic effluent water to permissible limits as per environment norms. The adapted bacteria are capable of reducing heavy metals with major constituent of zinc 500 ppm concentration to less than 5 ppm and pH of less than 1.0 to almost neural pH within 12 days of biological treatment. Only Zn and Fe were considered in establishing the parameters since these are the major constituents of the effluent water.

3.3 Selection of Carbon Source as Electron Donor

It was required to expedite the heavy metal removal to handle larger effluent volume. SRB could mediate sulfate reduction to a greater degree when simple carbon and energy sources were available to catalyze the reactions [9]. Table 3 represents reduction in heavy metals concentration (zinc, iron, cadmium,

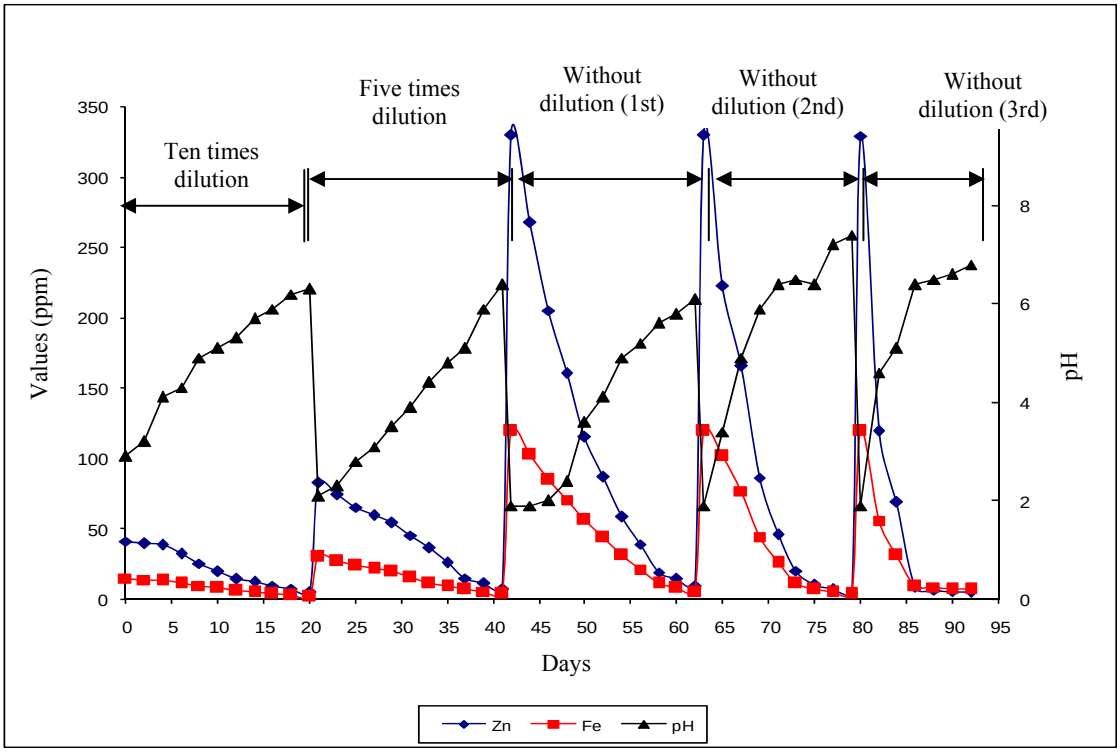


Fig. 3 Adaptation of SRB isolate.

Table 3 Effect of electron donors on percentage reduction of heavy metals and sulfate concentration.

Days	Zinc				Iron			
	Nutrient broth (2:8)	Whey (1:9)	Ethanol (1:9)	Sucrose (1:9)	Nutrient broth (2:8)	Whey (1:9)	Ethanol (1:9)	Sucrose (1:9)
0	0	0	0	0	0	0	0	0
2	43.06	49.16	10.44	15.20	36.57	50.87	26.29	29.89
4	66.79	74.19	28.35	27.88	65.64	68.53	41.06	40.16
6	79.14	88.07	51.65	57.33	83.74	86.27	64.64	66.49
8	91.89	97.40	62.66	76.11	90.24	95.60	73.71	81.53
10	97.15	98.77	71.65	86.28	94.08	97.20	86.09	88.52
12	98.54	99.30	87.23	93.44	94.25	97.53	87.48	92.68

Days	Cadmium				Manganese			
	Nutrient broth (2:8)	Whey (1:9)	Ethanol (1:9)	Sucrose (1:9)	Nutrient broth (2:8)	Whey (1:9)	Ethanol (1:9)	Sucrose (1:9)
0	0	0	0	0	0	0	0	0
2	33.19	35.89	30.30	32.43	38.81	43.90	34.20	40.99
4	79.14	84.18	72.43	81.13	87.11	91.90	84.09	91.32
6	98.54	99.88	97.99	99.98	98.75	99.87	98.32	99.19
8	100.0	100.0	100.0	100.0	100.0	100.0	100.0	100.0
10	100.0	100.0	100.0	100.0	100.0	100.0	100.0	100.0
12	100.0	100.0	100.0	100.0	100.0	100.0	100.0	100.0

Days	Sulfate			
	Nutrient broth (2:8)	Whey (1:9)	Ethanol (1:9)	Sucrose (1:9)
0	0	0	0	0
2	17.78	21.20	15.09	18.78
4	31.32	39.98	30.39	37.18
6	46.63	58.71	46.90	51.18
8	61.29	78.88	58.09	68.81
10	70.37	89.13	70.87	79.72
12	90.56	97.12	90.18	93.87

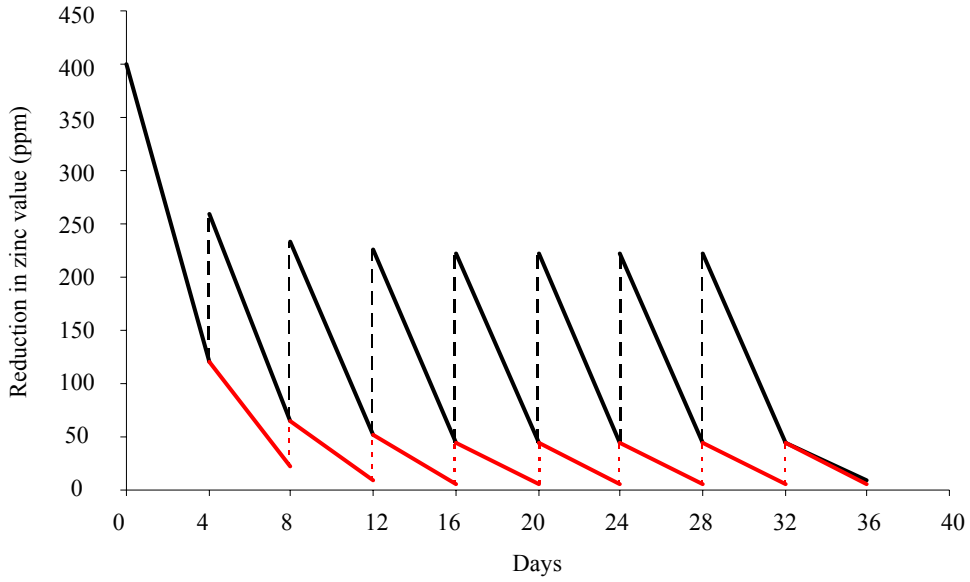


Fig. 4 Reduction in zinc concentration in two-stage anaerobic bioreactor using whey (1:9).

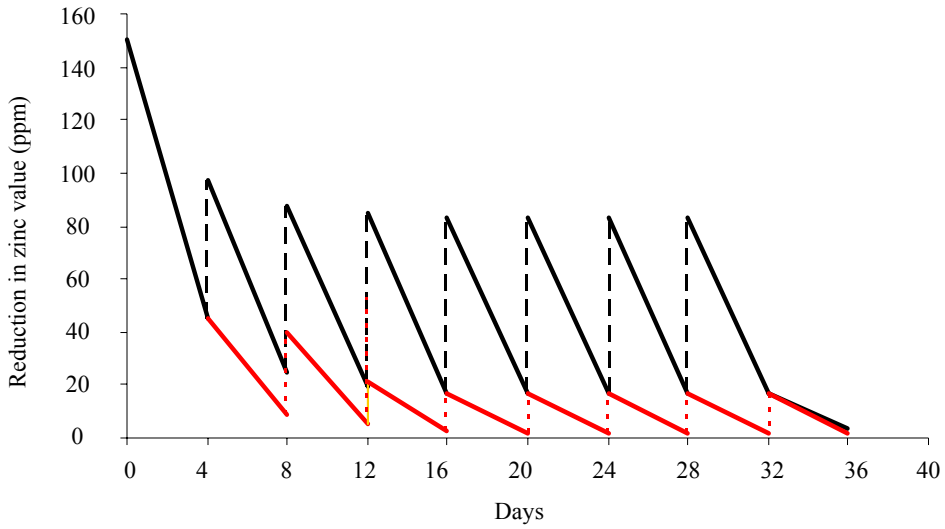


Fig. 5 Reduction in iron concentration in two-stage anaerobic bioreactor using whey (1:9).

and manganese) and sulfates in presence of nutrient broth (2:8), whey (1:9), ethanol (1:9) and sucrose (1:9) respectively. After 12 days of biological treatment, 99.30% and 97.53% reduction in zinc and iron, respectively was observed using whey as electron donor while for nutrient broth, ethanol and sucrose zinc reduction is 98.54%, 87.23% and 93.44%, respectively and for iron it is 94.25%, 87.48% and 92.68%, respectively. Sulfate reduction in all the electron donor sources is almost 90% other than whey (97.12%). After 6 days, treatment in all the cases, cadmium and manganese have reached to a level in traces. Whey was selected as best source for electron donor considering the reduction in heavy metal concentration and its cost.

3.4 Two-Stage Anaerobic Bioreactors

Figs. 4 and 5 show the treatment pattern of two stage anaerobic bioreactors for zinc and iron reduction. Upper solid lines represent first stage reactor and lower solid lines are for second stage reactor treatment. In both first stage anaerobic reactors, after 4 days of treatment period the zinc and iron concentration reduced up to 124.4 ppm and 45.0 ppm, respectively. 5 L from total 10 L was transferred to second stage treatment process, where Zn&Fe reduced to 23.6 ppm and 8.5 ppm, respectively, while the first stage reactor which has been leveled up with fresh effluent reduced has reduced these metals to 67.4 ppm and 24.4 ppm, respectively. This is again transferred to second stage reactor and reduced to 9.3 ppm and 5.6 ppm. The similar process is being continued for 36 days and under steady state conditions the zinc and iron concentration in treated effluent was 4.9 ppm and 1.8 ppm with treatment capacity of 30 L effluent in 4 days. The steady state condition was achieved after 20 days of treatment period.

4. Conclusions and Recommendations

Sulfate reducing bacteria isolated from Acid Plant of Debari Zinc Smelter, Hindustan Zinc Ltd., Udaipur, India was found the best isolate.

It was acclimatized for high heavy metals concentration (zinc $\approx$ 500 ppm, iron $\approx$ 160 ppm) under highly acidic solution (pH < 1.0).

Whey was found as the best electron donor in the effluent treatment.

Two-stage anaerobic bioreactor with treatment capacity of 30 L effluent has successfully reduced heavy metals as metal sulfides and attained almost neutral pH within short duration of 4 days. The pilot runs on the process confirm that it may be commercialized for treatment of effluents of zinc plants.

Acknowledgements

Authors would like to thank management of Hindustan Zinc Ltd. for granting permission to publish this paper. Technical guidance from Mr. Kamath and Mr. Mohanty is also acknowledged.

References

[1] Lens, P. N. L.; Visser, A.; Jansen, A. J. H.; Hulshoff, P. L. W.; Lettinga, G. *Crit. Rev. Environ. Sci. Technol.* **1998,** *28,* 41-88.

[2] Silva, A. J.; Varesche, M. B.; Foresti, E.; Zaiat, M. *Process Biochemistry* **2001,** *37,* 927-935.

[3] Jong, T.; Parry, D. L. *Water Research* **2003,** *37,* 3379-3389.

[4] Christensen, B., Laake M., Lien T. *Water Research* **1996,** *30,* 1617-1624.

[5] Tsukamoto, T. K.; Killion, H. A.; Miller, G. C. *Water Research* **2004,** *38,* 1405-1418.

[6] Vegt, A. L. D.; Dijkman, H.; Busiman, C. J. N. TMS Annual Meeting, San Antonio, Texas, 1998.

[7] Lowrie, D.; Hobson, J.; Stuckey, D. C. *Water Science and Technology* **2002,** *45,* 287-292.

[8] Barton, L. L.; Tomei, F. *Sulfate Reducing Bacteria;* Plenum Press: New York, 1995.

[9] Drury, J. W. *Water Environment Research* **1999,** *71,* 1244-1250.

[10] Widdel, F. *Biology of Anaerobic Microorganisms;* Zehnder, A. J. B., Ed.; Wiley: New York, 1988.

[11] Dinwoodie, J. M. *Wood: Nature's Cellular. Polymeric Fibre-Composite;* The Institute of Metals, London, 1989.

[12] Stafford, D. A.; Hawkes, D. L.; Horton, R. *Methane Production from Waste Organic Matter;* CRC Press: Boca Raton, F.L., 1980.

[13] Postgate, J. R. *The Sulfate Reducing Bacteria;* Cambridge University Press: Cambridge, 1984.

J. Chem. Chem. Eng. 8 (2014) 408-416

Influence of Pressure and Temperature on the Velocity of a Turbulent Jet Flow 3D

Flávia Aparecida Reitz Cardoso[1*], Regiani Aparecida de Almeida[2], Ricardo Vicente de Paula Rezende[3], Lúcio Cardozo-Filho[2], Dirceu Noriler[4], Henry França Meier[4] and Vladimir Ferreira Cabral[2]

1. Department of Mathematics, Federal Technological University of Paraná, Campo Mourao 87301-005, Brazil

2. Department of Chemical Engineering, State University of Maringa, Maringa 87020-900, Brazil

3. Department of Chemical Engineering, Federal University of Santa Catarina, Florianopolis 88040-970, Brazil

4. Department of Chemical Engineering, Regional University of Blumenau, Blumenau 89030-000, Brazil

Received: March 17, 2014 / Accepted: April 06, 2014 / Published: April 25, 2014.

Abstract: To investigate the influence of pressure and temperature on the jet velocity of a three-dimensional flow was the main goal of this study. Using a precipitation chamber with approximate capacity of 600 mL, it was studied the thermodynamic behavior of supercritical carbon dioxide mixture, dichloromethane and grape seed extract via SAS (supercritical antisolvent process). For the numerical solution, the Navier-Stokes equations were used along with the model of turbulence *k-ε* and Peng-Robinson equation of state with quadratic mixing rules of Van der Waals. The method of Chung was employed to determine the viscosity, thermal conductivity and mass diffusivity of the flow numerically solved through commercial code based on CFD (computational fluid dynamics). Simulations for pressures between 80 bar and 160 bar and temperatures between 308.15 K and 318.15 K showed large variations in the jet velocity, an important property in the dynamic mixing process that involves the size, size distribution and particle morphology.

Key words: Supercritical fluid, CFD, mathematical modeling.

Nomenclature

k	Turbulent kinetic energy ($m^2 \cdot s^{-2}$)
p	Pressure (bar)
R	Universal gas constant ($J \cdot mol^{-1} \cdot K^{-1}$)
R	Radial direction (m)
T	Temperature (K)
t	Time (s)
v	Velocity ($m \cdot s^{-1}$)
x	Axial direction (m)
ρ	Density ($kg \cdot m^{-3}$)
σ	Prandtl number (-)
ω	Fugacity (-)
λ	Thermal conductivity ($W \cdot m^{-1} \cdot K^{-1}$)
τ	Tensor stress (pa)
ε	Rate of turbulent kinetic energy dissipation ($m^2 \cdot s^{-3}$)
v	Molar volume ($m^3 \cdot mol^{-1}$)

[*]**Corresponding author:** Flávia Aparecida Reitz Cardoso, Ph.D. Student, research fields: computational fluid dynamics and supercritical technology. E-mail: flaviareitz@gmail.com.

1. Introduction

Among the existing methods of preparing nanoparticles, SAS (supercritical antisolvent precipitation) is becoming increasingly important due to the large amount of chemicals that can be processed with this technology [1-3]. Above the critical point of the mixture, there condition of complete miscibility, typically in the range of 8-16 MPa, where CO_2 is completely miscible with many organic solvents and supercritical turbulent mixing is the most important issue. The SAS process involves mixing CO_2 and organic solution (solute dissolved in an organic solvent) from two outputs of a coaxial nozzle system, to obtain the desired conditions to produce thermodynamic supersaturation and particle formation, and the resulting PSD (particle size distribution) is affected by blending [4]. While blending effects are well known

to those based on precipitation in liquids [5], such effects are not very often reported in supercritical systems.

Despite a number of studies that support this evidence under the experimental point of view, little research is available in the context of numerical modeling. A mathematical model for mass transfer between a droplet of organic solvent and a compressed antisolvent was developed by Werling and Debenedetti [6], while Chavez et al. [7] have proposed a methodology to calculate the time scales involved. A more elaborate model, solved by CFD (computational fluid dynamics) was proposed by Martin and Cocero [3], in which a turbulence model was solved in conjunction with mass balances and took into account the effect of mass transfer in the system. The authors employed a locking to solve the PBE (population balance equations) [8]. The results were strongly affected by the value of solid-liquid surface tension. Forecasts obtained from models are valuable for understanding the process behavior at a large-scale industrial level. Henczka et al. [9] studied numerically supercritical antisolvent precipitation of paracetamol with carbon dioxide as antisolvent and took into account the heat of mixing in the studied system. The PSD was calculated using the standard method of moments, and the interaction between mixing and precipitation was taken into account with the β-PDF approach along with the turbulent model of Baldyga mixer [10]. This first attempt showed the importance of including mixing effects in the model, and highlighted some limitations of the approaches available. Since the micromixing models available [1-8], needed to explain the interactions between turbulence and particle formation are valid only for standard fluids, and its extension to supercritical fluids is not simple [11]. It is known that the fluid properties change drastically near and above the critical point, then the dynamic behavior of the fluid also changes and this directly influences the mixing at all scales.

A large number of publications on the micronization of different materials with the SAS process appears concerned with the experimental analysis of the effects of operating conditions on the size distribution and morphology of the particles, and how this type of analysis is often difficult, because the interactions between these parameters. This study aims to provide a mathematical formulation capable of describing the influence of pressure and temperature on the jet velocity of a three-dimensional flow phenomena that influence the turbulent mixing observed in the SAS process. Once validated, the effects of thermodynamic properties can be used for modeling, scale-up and optimization of systems, with acceptable precision for engineering calculations.

2. Governing Equations

2.1 Thermodynamics

The density of the mixture is described by Peng-Robinson equation of state with the quadratic mixing rules of Van der Waals:

$$p = \frac{RT}{v-b_m} = \frac{a_m T}{v(v+b_m)+b_m(v-b_m)} \quad (1)$$

where, p the pressure, v molar volume, T temperature, a_m and b_m the constants of the equation for the case of mixtures. These constants are obtained by mixing rule is given by $a_m = a(T) = \sum_i \sum_j x_i x_j a_{ij}$ and $b_m = b(T) = \sum_i \sum_j x_i x_j a_{ij}$, where, x_i is the molar concentration of the component, i is combination rulesfraction: $a_{ij} = \sqrt{a_i a_j}(1 - k_{ij})$ and $b_{ij} = \frac{b_i + b_j}{2}(1 - l_{ij})$.

This formulation allows to study the importance of solving the resulting system of equations in non-isothermal regime.

2.2 Hydrodynamics

The conservation equations are expressed here to a differential control volume fixed in three dimensional space of the flow of a mixture in the supercritical state and considering the turbulent flow, a variable can be

considered as the sum of an average value plus a fluctuation $\phi = \tilde{\phi} + \phi^{创} = \bar{\phi} + \phi'$. The equation of continuity in Cartesian coordinates for a system with variable density in steady state is given by:

$$\partial i\left(\bar{\rho}\,\tilde{u}_i\right) = 0 \tag{2}$$

where, $\tilde{u}_i$, with $i \in \{1, 2, 3\}$, represents the velocity vector mean component $\tilde{u}$ to the position vector components respectively.

The equation of motion that takes into account the density and viscosity are variable.

$$\partial i\left(\bar{\rho}\,\tilde{u}_i\,\tilde{u}_j\right) = \partial j\bar{P} + \partial j\left(\tilde{\tau}_{ij} - \bar{\rho}u_i'u_j'\right) \tag{3}$$

where, $-\bar{\rho}u_i'u_j'$ is the Reynolds tensor, resolved by the turbulence model and the two equations

$$\tilde{\tau}_{ij} = \mu\left\{2\left(\frac{\partial \tilde{u}_i}{\partial x_j} + \frac{\partial \tilde{u}_j}{\partial x_i}\right) - \frac{2}{3}\delta_{ij}\frac{\partial \tilde{u}_k}{\partial x_k}\right\} \tag{4}$$

Considering the viscous dissipation of energy Eq. (4) and species conservation Eq. (5) are given by:

$$\frac{\partial}{\partial x_i}\left(\bar{\rho}\tilde{u}\tilde{h}\right) = \frac{\partial}{\partial x_i}\left(\frac{k_M + k_T}{C_p} + \bar{\rho}u_j'\tilde{h}\right) + \tilde{\tau}_{ij}\frac{\partial}{\partial x_j}\tilde{u}_i \tag{5}$$

and

$$\frac{\partial}{\partial x_j}\left(\bar{\rho}\,\tilde{u}_j\,\tilde{y}_i + \bar{\rho}u_j^{创}y_i'\right) = \frac{\partial}{\partial x_j}\left(\bar{\rho}D_m\frac{\partial y_i}{\partial x_j}'\right) \tag{6}$$

where, $\tilde{h}$ is the enthalpy, the mass fraction y_i of component i and D_m the molecular diffusion coefficient.

2.3 Model of Turbulence

The model of turbulence k-ε for two equations was used in this study, and consists of two semiempirical Eqs. (7) and (8) for the turbulent kinetic energy k and for dissipation rate of turbulent kinetic energy ε:

$$\underbrace{\frac{\partial}{\partial x_j}\left(\rho k\,\tilde{u}_j\right)}_{I} = \underbrace{\frac{\partial}{\partial x_j}\left[\left(\mu + \frac{\mu_T}{\sigma_k}\right)\frac{\partial}{\partial x_j}k\right]}_{II} + \underbrace{P_k}_{III} - \underbrace{\rho\varepsilon}_{IV} \tag{7}$$

$$\underbrace{\frac{\partial}{\partial x_j}\left(\rho\varepsilon\tilde{u}_j\right)}_{I} = \underbrace{\frac{\partial}{\partial x_j}\left[\left(\mu + \frac{\mu_T}{\sigma_k}\right)\frac{\partial}{\partial x_j}\varepsilon\right]}_{II} + \underbrace{C_{\varepsilon 1}\frac{\varepsilon}{k}P_k}_{III} - \underbrace{C_{\varepsilon 2}\frac{\rho\varepsilon^2}{k}}_{IV}, \tag{8}$$

where, ε is the dissipation per unit mass. In Eqs. (7) and (8), the term *I* is the convective transport of k or ε; the term *II* corresponds to diffusive transport; the term *III* is the production rate; and the term *IV* is the destruction rate. P_k is a term of turbulence production due to viscous forces.

$$P_k = \mu_t\nabla\tilde{\mathbf{u}}:\left(\nabla\tilde{\mathbf{u}} + \nabla\tilde{\mathbf{u}}^T\right) - \frac{2}{3}\nabla\tilde{\mathbf{u}}\left(3\mu_T.\tilde{\mathbf{u}} + \rho k\right) \tag{9}$$

where, ũ is the mean velocity vector. The empirical constants of the model are $C_\eta = 0.09$; $C_{\varepsilon 1} = 1.44$, $C_{\varepsilon 2} = 1.92$, $\sigma_\kappa = 1$, $\sigma_\varepsilon = 1.3$. The turbulent viscosity can be calculated with the equation $\mu_t = \frac{C_\eta \rho k^2}{\varepsilon}$.

This model of two equations has been used in the description of turbulent jet under supercritical conditions [12].

3. Methodology

The objective of this study is to investigate the effects of temperature and pressure in jet velocity of a three-dimensional flow in SAS process and the work of Franceschi [13] was chosen as a reference to validate the model. The experimental apparatus consists of a tubular precipitator of approximately 600 mL volume. The device design is shown in Figs. 1 and 2. Table 1 summarizes the experimental conditions investigated. Under these conditions, there is complete miscibility between CO_2 and dichloromethane (single phase region).

The simulations were made from mixed mesh with tetrahedral elements and hexahedral elements and a total number of 1.028×10^6 cells. The mesh and geometry details associated with it are shown in Figs. 1 and 2. The details of the inner cell distribution and refining regions at the exit of the capillary and close to

the exit of the mixing tube can be seen in Fig. 2 which shows a cutting plane at the center of the chamber.

The chamber has an internal diameter of 80 mm and inside length of 120 mm, capillary length coaxial injection of 98 mm and the diameter of the inlet of CO_2 is 0.97 mm and the solution inlet diameter is 0.1 mm, and the capillary tube starts at 10 mm inside the chamber. Contains output by the lid, this being a tube

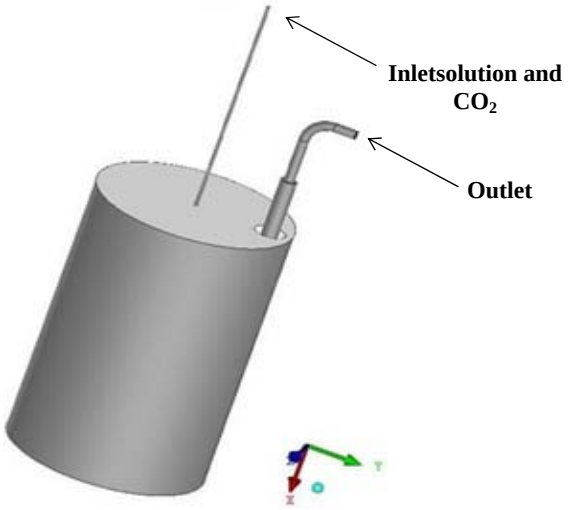


Fig. 1 Mesh with detail geometry with coaxial input and CO_2 solution.

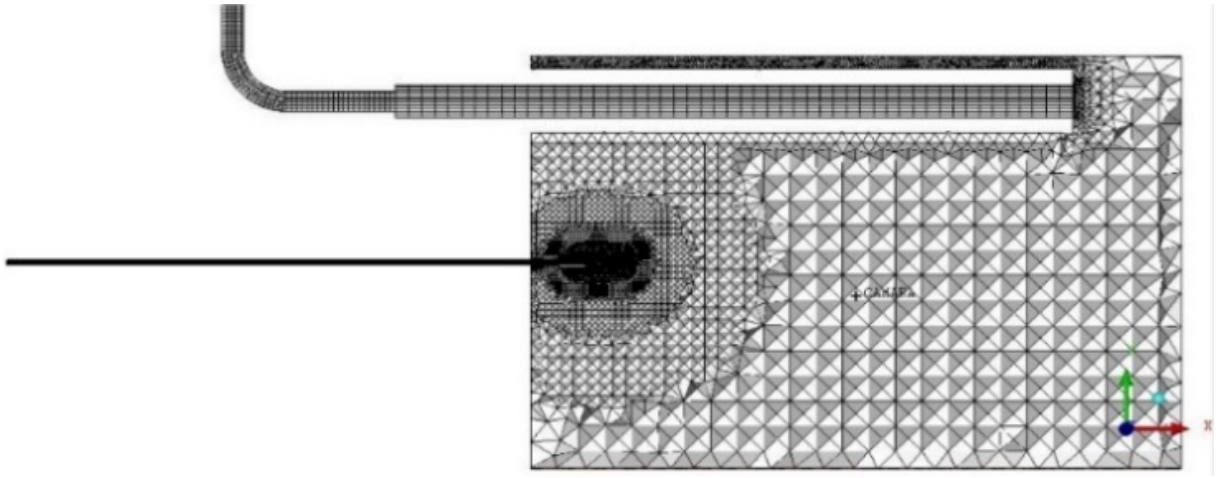


Fig. 2 Aspects of the internal elements of the mesh.

Table 1 Operating conditions.

Simulation	Temperature (K)	Pressure (bar)
1	308.15	80
2	313.15	80
3	318.15	80
4	308.15	120
5	313.15	120
6	318.15	120
7	308.15	160
8	313.15	160
9	318.15	160

of length 164 mm and internal diameter 6.34 mm starting at 35 mm from the bottom of the chamber and the end of the outlet tube diameter is 3.87 mm.

To solve the system of Eqs. (1)-(8), we used the ANSYS FLUENT 14.5 software, which makes use of the finite volume method. The segregated solver was employed through the SIMPLEC algorithm, whose goal is to solve the linear systems in each equation one by one, updating its coefficients due to nonlinearities and the coupling between variables.

As convergence criteria was considered the residual sum below 10^{-5} for all variables and imposed the closure of mass balance $\left|m_{CO_2} + m_{sol} - m_{out}\right| < 10^{-11}$.

4. Results and Discussion

The results obtained from simulations performed by the software for carbon dioxide mixture, dichloromethane and the grape seed extract, since the presence of the grape seed extract in the system does not change the phase behavior of the binary solvent system plus antisolvent [13] so that still considered the system in a single phase.

4.1 Effect of Pressure

Experimental studies have shown that the pressure directly affects the size, size distribution and morphology of the particle, mostly related to temperature, antisolvent flow rate and the concentration of the solute [13].

Analyzing Figs. 3-5, there is the influence on the magnitude of the velocity obtained by the centerline of the precipitation chamber. As the pressure decreases, the jet velocity increases, which results in homogeneous and nearly spherical particles, as demonstrated experimentally by Petit-gas et al. [14] for various mixtures in the SAS process.

Under these operating conditions and according to the results, the most advantageous option would be the use of lower pressure, as experimentally obtained for Franceschi [13] in a precipitation chamber.

4.2 Effect of Temperature

With respect to the influence of temperature on the velocity of the jet can be seen in Figs. 6-8 that their maximum values promoted increase of jet velocity and thus increase the yield of precipitated particles, as described by Bashipour and Ghoreishi [15] when extract β-carotene from the aloe vera plant.

In addition to these operating conditions, other factors may also influence the velocity of the jet and hence the particle size. Cases such as the size of the precipitation chamber, flows and concentrations of the components of the mixing chamber must also be analyzed.

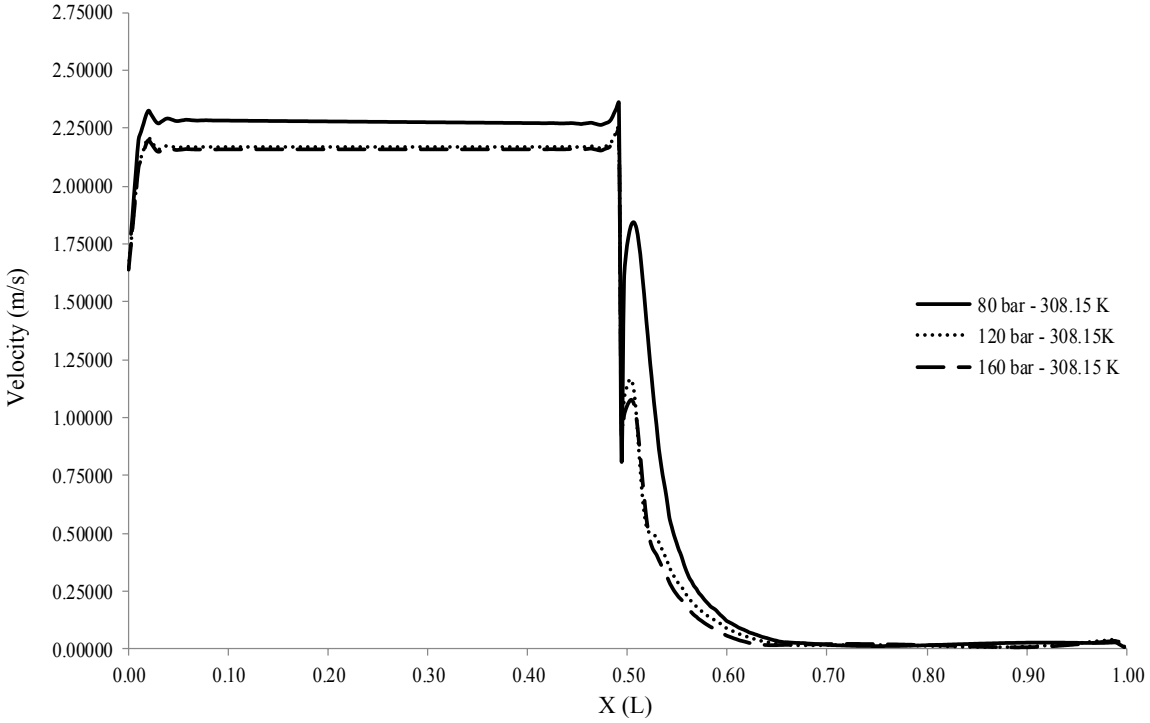


Fig. 3 Values of the magnitude of the velocity along the axis of the chamber with a temperature of 308.15 K.

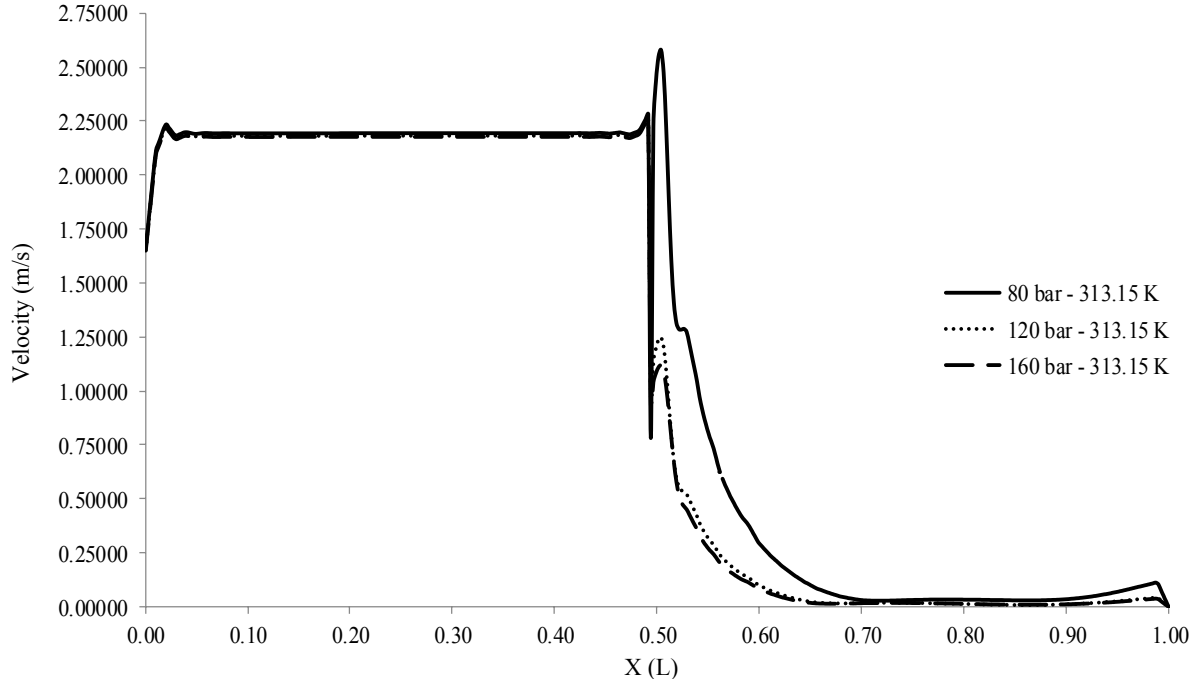


Fig. 4 Values of the magnitude of the velocity along the axis of the chamber with a temperature of 313.15 K.

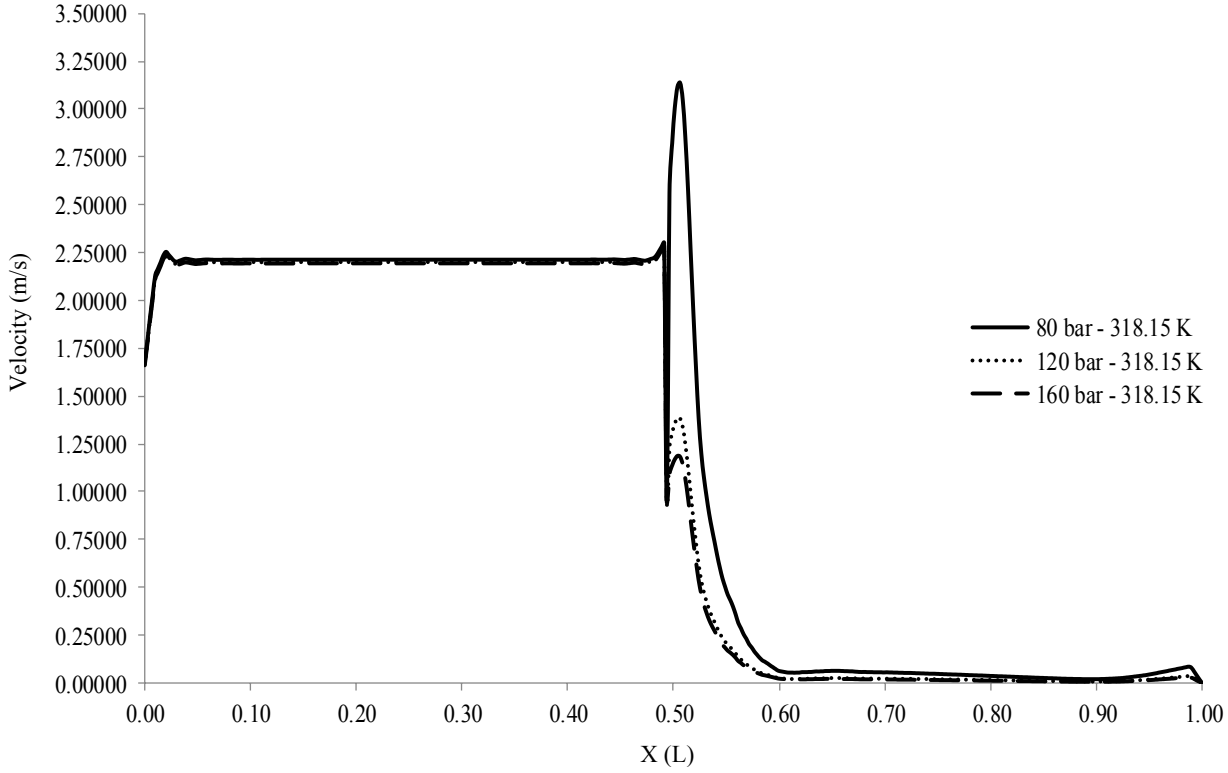


Fig. 5 Values of the magnitude of the velocity along the axis of the chamber with a temperature of 318.15 K.

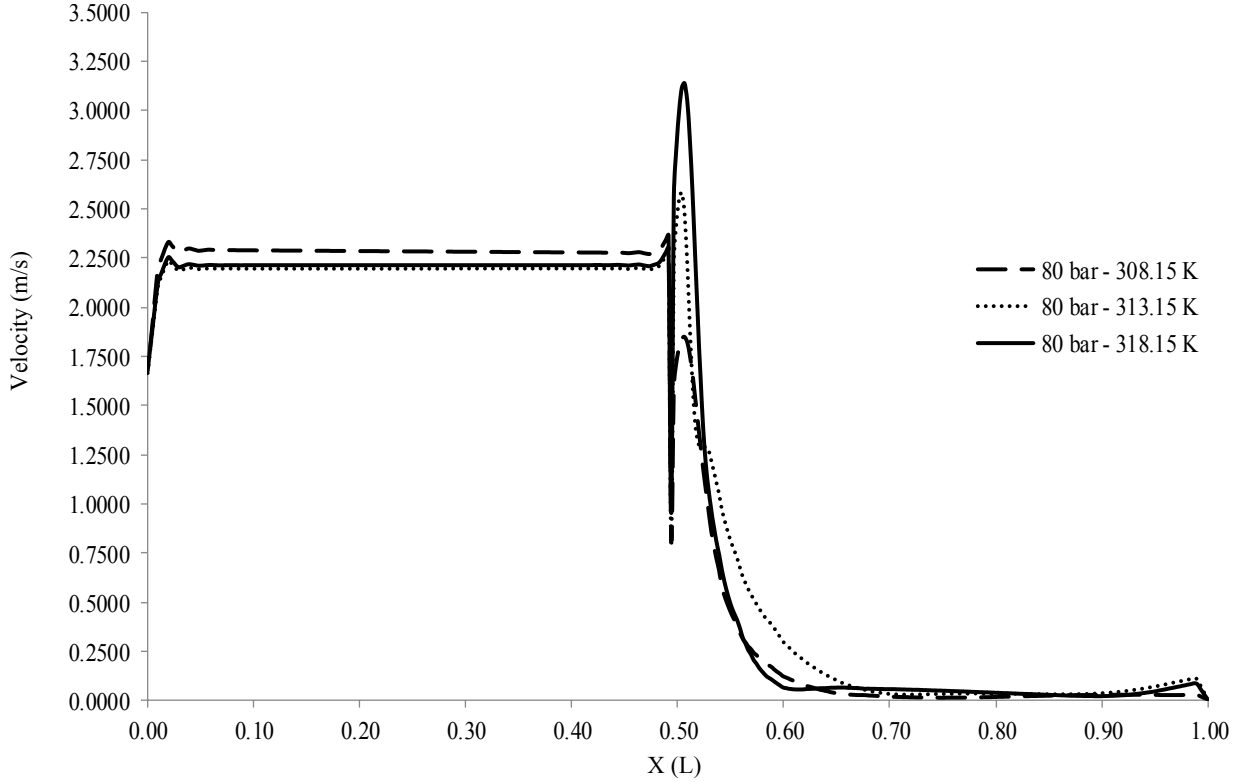


Fig. 6 Values of the magnitude of the velocity along the axis of the chamber with a pressure of 80 bar.

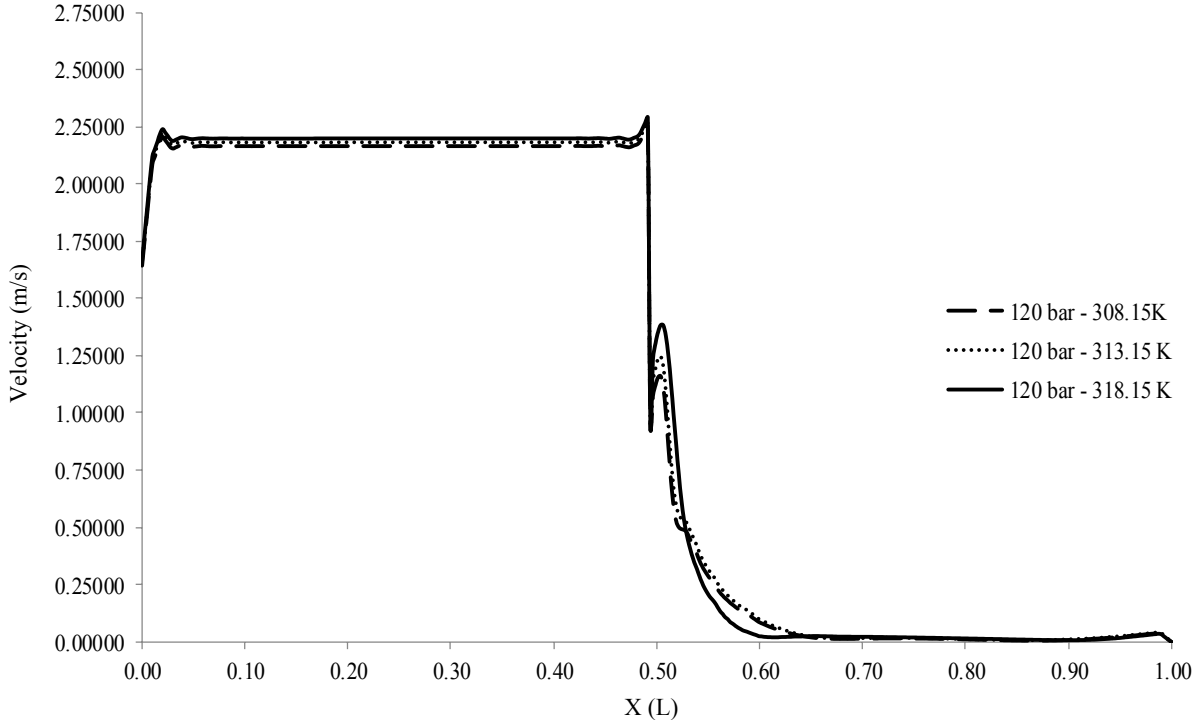


Fig. 7 Values of the magnitude of the velocity along the axis of the chamber with a pressure of 120 bar.

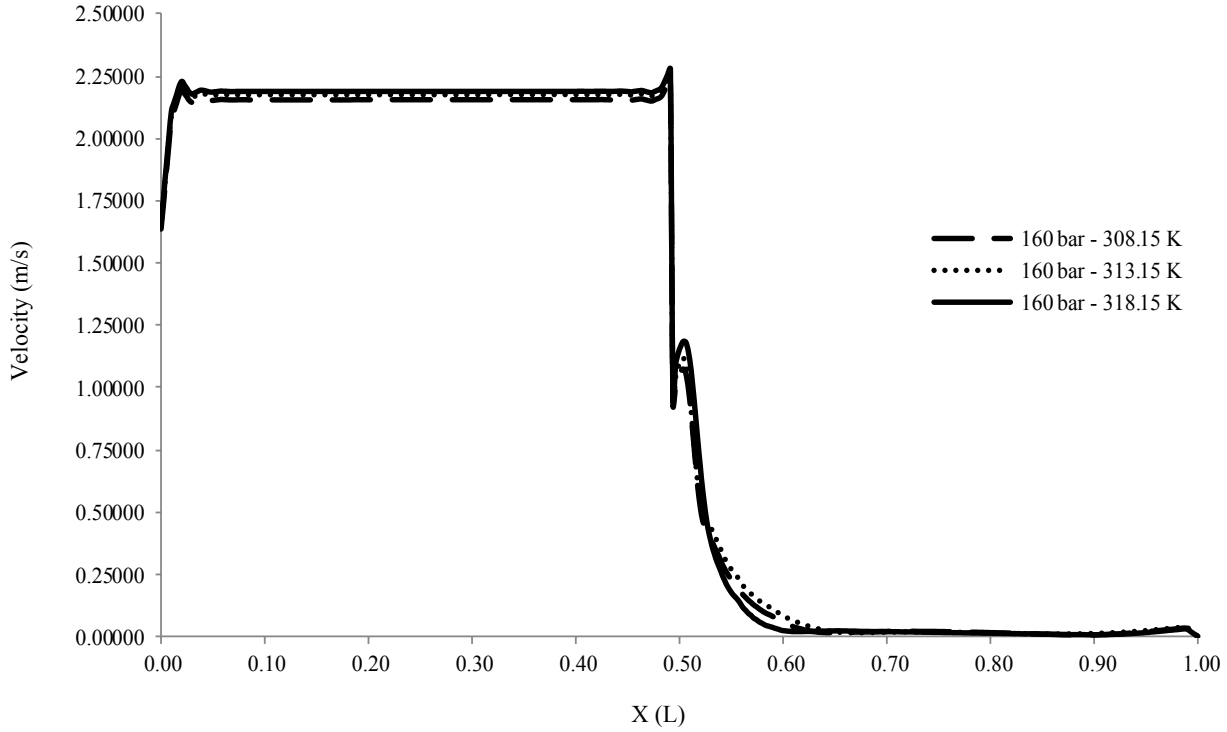


Fig. 8 Values of the magnitude of the velocity along the axis of the chamber with a pressure of 160 bar.

5. Conclusions

A model used to describe the velocity of the jet in the precipitation of the grape seed extract employing the SAS process was developed. The model includes the density of the mixture via Peng and Robinson [16] equation of state with quadratic mixing rules of Van der Waals for the analysis of the mixture behavior. For the investigated variables, pressure and temperature, results showed they influence the velocity of the jet solution which experimentally impacts the size and morphology of the particles with a stronger effect at lower pressure and higher temperature operation.

The predictions matched well with the experimental data in all cases studied, and although they have not yet combined with a population balance that determines the size and size distribution of particles, the model is able to explain the experimental trend in the jet velocity of a three-dimensional flow and offers a valuable insight into the process. The next steps of this work will be toward another validation of the model in a wide range of operating conditions. In particular, the cases in which the mixture affects precipitation will be investigated. A follow up study will also examine the range of Reynolds numbers for which the effects of turbulence can be optimized, resulting in a final product of good quality.

References

[1] Jung, J.; Perrut, M. Particle Design Using Supercritical Fluids. *Journal of Supercritical Fluids* **2001,** *20,* 179-197.

[2] Reverchon, E.; Adami, R.; Caputo, G.; Marco, I. Spherical Microparticles Production by Supercritical Antisolvent Precipitation. *Journal of Supercritical Fluids* **2008,** *47,* 70-84.

[3] Martin, A.; Cocero, M. J. Numerical Modeling of Jet Hydrodynamics, Mass Transfer and Crystallization Kinetics in the Supercritical Antisolvent (SAS) Process. *Journal of Supercritical Fluids* **2004,** *32,* 203-219.

[4] Shekunov, B. Y.; Baldyga, J.; York, P. Particle Formation by Mixing with Supercritical Antisolvent at High Reynolds Numbers. *Chemical Engineering Science* **2001,** *56,* 2421-2433.

[5] Baldyga, J.; Makowski, L.; Orciuch, W. Interaction between Mixing, Chemical Reactions and Precipitation. *Industrial & Engineering Chemistry Research* **2005,** *44,* 5342-5352.

[6] Werling, J. O.; Debenedetti, P. G. Numerical Modelling of Mass Transfer in the Supercritical Antisolvent Process: Miscible Condition. *Journal of Supercritical Fluids* **2000,**

18, 11-21.

[7] Chavez, F.; Debenedetti, P.; Luo, J.; Dave, R.; Pfeffer, R. Estimation of the Characteristic Time Scales in the Supercritical Antisolvent Process. *Industrial & Engineering Chemistry Research* **2003,** *42,* 3156-3162.

[8] Pratsinis, S. E. Simultaneous Nucleation, Condensation and Coagulation in Aerosol Reactors. *Journal Colloid and Interface Science* **1988,** *124,* 416-429.

[9] Henczka, M.; Baldyga, J.; Shekunov, B. Y. Particle Formation by Turbulent Mixing with Supercritical Antisolvent. *Chemical Engineering Science* **2005,** *60,* 2193-2201.

[10] Baldyga, J. Turbulent Mixer Model with Application to Homogeneous, Instantaneous Chemical Reactions. *Chemical Engineering Science* **1989,** *44,* 1175-1182.

[11] Oschwald, M.; Smith, J. J.; Branam, R.; Hussong, J.; Schik, A.; Chehroudi, B.; et al. Injection of Fluids into Supercritical Environments. *Combustion Science Technology* **2006,** *178,* 49-100.

[12] Sierra-pallares, J.; Marchisio, D. L.; Parra-santos, M.; Garcia-serna, J.; Castro, F.; Cocero, M. A Computational Fluid Dynamics Study os Supercritical Antisolvent Precipitation: Mixing Effects on Particle Size. *AIch. E. Journal* **2012,** *58,* 385-398.

[13] Franceschi, E. Precipitation and Encapsulation of β-carotene in PHBV Using Supercritical Technology. Ph.D. Thesis, Federal University of Santa Catarina, 2009.

[14] Petit-gas, T.; Boutin, O.; Raspo, I.; Badens, E. Role of Hydrodynamics in Supercritical Antisolvent Processes. *Journal of Supercritical Fluids* **2009,** *51,* 248-244.

[15] Bashipour, F.; Ghoreishi, S. M. Experimental Optimization of Supercritical Extraction of β-carotene from Aloe Bar Badensis Miller via Genetic Algorithm. *Journal of Supercritical Fluids* **2012,** *72,* 312-319.

[16] Peng, D. Y.; Robinson, D. B. A New Two-Constant Equation of State. *Industrial Engineering Chemistry Fundamentals* **1976,** *15,* 59-72.

J. Chem. Chem. Eng. 8 (2014) 417-420

Polymer-Based Micro Flow Sensor with Alternative Electronic Signal Interfaces for Low and High Flow Rates

Thomas Schönstein*

Head Application Development, Innovative Sensor Technology IST USA Division, Las Vegas 89147, USA

Received: July 30, 2013 / Accepted: August 21, 2013 / Published: April 25, 2014

Abstract: The qualitative and quantitative assessment of gas flow has become increasingly relevant in the use of everyday systems. The micro flow sensor, developed by Innovative Sensor Technology AG (Switzerland), is by principle a calorimetric flow sensor produced as a micro system on a glass substrate by means of photolithography and glass etching technology. These structures are arranged as a platinum micro heater and sensor in a Wheatstone bridge. The subsequent etching process produces an exposed area of polyimide membrane that is only a few microns thick and includes the resistive sensor structure as the active area. In addition, the RTD (resistance temperature detector) technology included on the sensor allows for the implementation of a variety of electronic biasing and signal processing modes. Since the sensor can be powered and the bridge can be measured in both CTA (constant temperature anemometer) and calorimetric mode, new possibilities are presented for both low and high flow rates with regard to temperature compensation, self-calibration and self-monitoring.

Key words: Calorimetric flow sensor, pick & place assembly, CTA-mode, low and high flow rates.

1. Introduction

The sensors are characterized by a very small time response and low power consumption, achieved through the principle of MEMs (Micro-Electro-Mechanical Systems) hot film anemometry. Despite an extremely thin membrane, the glass carrier produces a robust sensor and provides easy handling. The heater/sensor structure, in combination with the full bridge circuitry "on chip", ensures simple signal evaluation and offers the ability to detect the flow direction. The thin film sputtering and etching processes of IST AG (Innovative Sensor Technology AG) allow for low initial development costs for application-specific, custom sensor designs and support cost effective volume production. A wide range of sensor dimensions, resistance values, structural formations and mounting configurations are possible. As a result, cost effective solutions including a sensor on PCB (printed circuit board) with electronic signal processing and flow channel can be easily developed in a timely manner.

2. Sensor Advantages

Compared with its silicon-based counterparts, the micro flow sensor (Fig. 6) from IST AG offers major advantages relating to dynamic measuring range and assembly of the sensing element into customer systems for design-in processes (Fig. 1). Due to the sensor's ability to operate in a combination of CTA (constant temperature anemometer) and calorimetric mode, the flow signal saturation can be shifted from 1 m/s (only calorimetric mode) to 50 m/s (both modes combined). These flow velocities translate to a volumetric flow range from 0.001 L/min full scale to 10 L/min full scale (depending on the flow channel cross-sectional area) with a possible resolution of 1%

*Corresponding author: Thomas Schönstein, Dipl. Eng.. E-mail: thomas.schoenstein@ist-ag.com.

of the full scale value.

The response time of 10 ms and warm up time of 100 ms allows for time-based low power heater management. With the platinum technology of all resistive structures, a heater temperature regulation loop can be realized in order to maintain a constant temperature and to protect the sensor against damage from overheating. Especially during power down cycles, the resistive structures can be used to measure the gas temperature. As a result, it is possible to maintain active temperature compensation by tracking the heating power of the sensor's micro heater.

3. Sensor Assembly

The sensors can be produced economically and are well-suited for pick & place assembly. It can be handled similar to an IC-die or SMD (surface mount device) component, assembled by standard pick & place machines or by hand. Electronic connections to a PCB can be achieved through wire bonding or flip chip technology. The sensor can be assembled over a milled PCB channel or directly embedded into a PCB cavity (Fig. 1). The goal of IST's sensor/electronic interface development is to provide customers with an easy-to-use measurement concept for realizing their own proprietary solutions down to the component level of flow measurement technique.

4. Calorimeter Mode

The most common used measuring mode for micro machined flow sensors is the calorimetric mode. Here the temperature distribution along a sensor-heater-sensor-structure depending on gas flow is used to provide an electrical differential signal by thermal imbalance of upstream and downstream sensor elements (e.g. thermopiles) (Fig. 2).

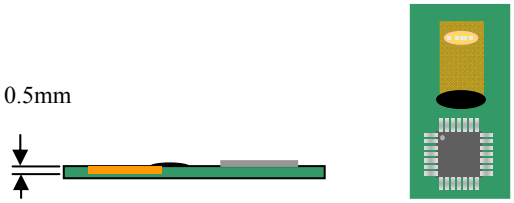


Fig. 1 Assembly example of micro flow sensor.

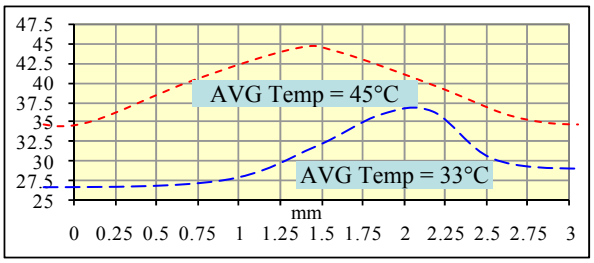


Fig. 2 Example of symmetrical and imbalanced temperature distribution on a 3 mm sensor area.

In case of a flow rate near by 200 mL/min, a temperature difference of some degree centigrade (°C) between up- and down-stream sensor appears and causes a bridge signal of about 40-50 mV. Here, the user is faced with premature saturation effects, preventing high flow applications. This can be eliminated by using both flow measuring modes at one sensor structure (calorimetric and anemometric mode). The anemometric mode, especially the CTA-mode, is responsible for compensating the loss of heating power caused by gas flow. So an extended measuring range of calorimetric mode can be achieved. And additionally the output of the CTA can be used up to flow rates of 10 L/min (Fig. 3).

5. CTA-Mode

The most popular anemometer is the CTA. It is function is well described by the King's Law:

$$P_H = I_H^2 \cdot R_H = \left(A + B \cdot \vec{v}^{\,n}\right) \cdot \Delta T$$
$$n = 0.3 \cdots 0.5 \qquad (1)$$

By converting and simplifying this equation we obtain this formula:

$$U = U_0 \cdot \sqrt{1 + k \cdot \vec{v}^{\,n}} \qquad (2)$$

where, U: CTA-output; U_0: free convection offset; k: fluidic depend constant; $\vec{v}$: fluid velocity.

Thus, the output is determined by an offset (U_0), an offset dependent slope of the curve, and the fluidic dependent gain value (k).

Here, U_0 represents the value of constant temperature difference (ΔT) between the heater and fluid. Strictly speaking, the controller of a CTA keeps the resistive structure at a constant temperature. So,

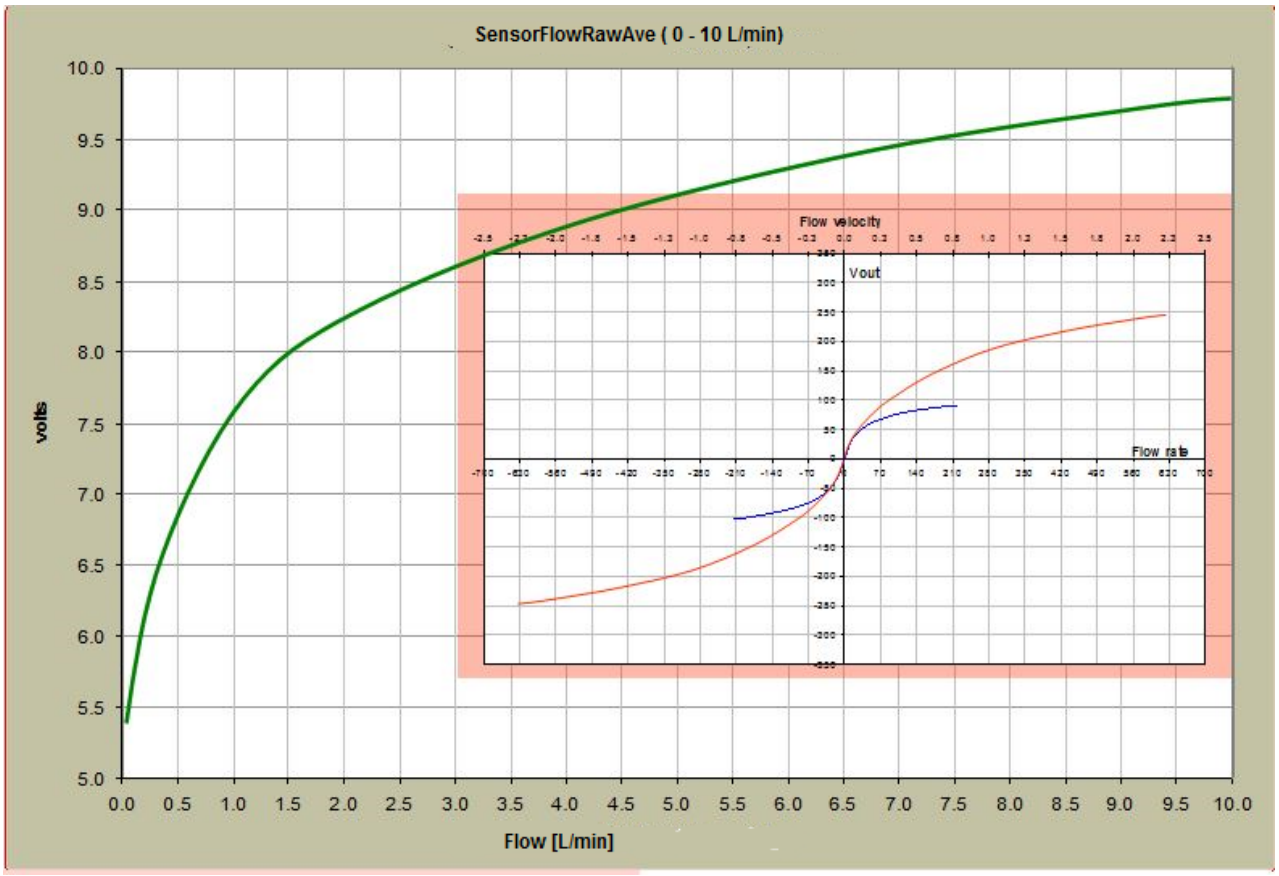


Fig. 3 Example of extended flow range by using CTA-output.

different passivation thicknesses and flow element surfaces impact the CTA characteristics, even a deviation in the heat transfer coefficient (α). The characteristics depend not only on sensor alignment/orientation and fluid type, but also on fluid temperature and sensor contamination (such as dust).

So the equation for a still fluid is:

$$\alpha_0 \cdot A \cdot \Delta T \sim U_0^2 \left(1 + k \cdot \vec{v}^{\,n}\right) \quad (3)$$

$$\alpha_0 \cdot A \cdot \Delta T \sim U_0^2 \quad (4)$$

That means each deviation of CTA-characteristic, caused by free convective parameters like α_0 can be compensated by a U_0-adjustment at $\vec{v} = 0$. In order to calibrate the *k*-value (fluidic-caused errors) more than one point is necessary. But, fluidic-caused errors mostly depend on mechanical alignment deviations of the sensor mounting. If mounting errors can be determined by module construction, a one point calibration provides good results for many applications.

5. Chip Design and Circuit

To get a high flow rate sensor circuit a microflow sensor has to be implemented into a CTA-bridge.

The complete 4-resistor sensor bridge acts as the heater of the CTA (Rs1, ···, Rs4). The outputs "Flow Dir" provide once the calorimetric mode and also the signal for flow direction.

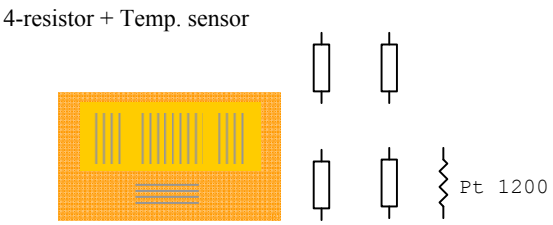


Fig. 4 Four resistors layout with temperature compensation.

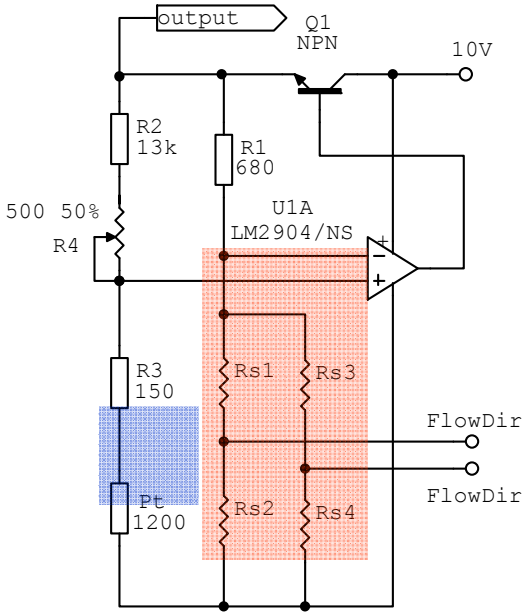


Fig. 5 Sensor layout and CTA circuit.

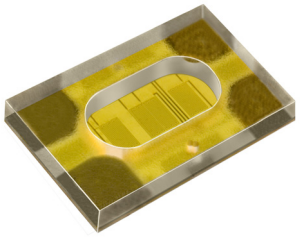


Fig. 6 Microflow sensor element 3 mm × 5 mm × 0.5 mm.

References

[1] Brokmann, U.: Contribute to the Micro Structure of Photo-Imagable Glass by UV Radiation. Ilmenau: TU, 2005.

[2] Mrotzek, S.; Hülsenberg, D.; Hesse, A. Crystallization of a Glass in the Photo-Structured System Li_2O-Al_2O_3-SiO_2. Ilmenau: TU.

[3] Technical Glass Works Ilmenau: Photo Structurable Glass for Micro-Engineering Applications. fuko_flyer.pdf, Ilmenau.

J. Chem. Chem. Eng. 8 (2014) 421-427

The Sensitivity of TE Filed Propagating in LHM-Antiferromagnetic Sensor

Zeyad I. Al-Sahhar[1], Hala J. El-Khozondar[2*] and Mohamad M. Shabat[3]

1. Physics Department, Al-Aqsa University, Gaza P. O. Box 4051, Palestine

2. Electrical Engineering Department, Islamic University, Gaza P. O. Box 108, Palestine

3. Physics Department, Islamic University, Gaza P. O. Box 108, Palestine

Received: February 20, 2014 / Accepted: March 08, 2014 / Published: April 25, 2014.

Abstract: A three-layer waveguide structure sensor consists of LHMs (left-handed materials) film surrounded by dielectric cladding and antiferromagnetic substrate is proposed. LHMs known as MTMs (metamaterials) have simultaneous negative permeability and permittivity. The dispersion relation for the structure is derived for TE guided modes. Two ranges of frequencies are chosen such that Voigt permeability, μ_v, either negative or positive. The sensitivity is proven to be affected by different parameters including the film thickness, LHM parameters, and Voigt frequency.

Key words: MTMs, LHMs, antiferomagntic, optical waveguide sensors, sensitivity.

1. Introduction

A sensor in general recognizes and senses the presence of an analyte (the specie to be detected). The ideal sensor not only has to respond to low concentrations of analytes, but also must have the ability to discriminate among species. Sensors have a broad range of applications in medical, pharmaceutical, environmental, defense, bioprocessing or food technology.

The need for fast, easy to use, compact and cheap sensors is the motivation of this study. In this paper, the proposed structure is a three-layer system consists of new man-made materials named metamaterials as film sandwiched between an antiferromagnetic substrate and dielectric cladding. Antiferromagnetic metal is studied extensively because its negative dielectric constant influences the dispersion relation in a qualitative manner.

Ritchie [1] first study led to the fast growing field of plasmonics owing to their potential application in areas as diverse as biosensing [2]. Several studies is conducted to understand both surface magnetic polaritron (plasmons) and guided waves in magnetic (anti/ferromagnetic) layered waveguides [3-10] where magnetic layered intercalated with dielectric layers or MTMs (metamaterials) layers.

LHM (left-handed materials) or MTMs are materials, which have been fabricated in the laboratory. Veselago [11] theoretically predicated the existence of LHM with both negative permeability ($\mu < 0$) and negative permittivity ($\varepsilon < 0$) and verified experimentally by Pendry et al. [12, 13] and Shelby et al. [14]. These materials have unique electromagnetic properties made them attractive to several applications including antenna design, superlenses, higher resolution magnetic resonance imaging [15, 16], sensors [17-19] and isolators [20, 21].

The dispersion relation for the proposed structured is derived for TE (transverse electric fields) propagating modes only. The homogenous sensitivity, *S*, is defined as the change in the effective refractive

*Corresponding author: Hala J. El-Khozondar, Professor, research field: electrooptics. E-mail: hkhozondar@iugaza.edu.ps.

index with cladding index [22], is then calculated to measure the ability of the proposed structure to detect and sense small changes at the cladding. Next section is devoted to cover the background. Numerical calculations and result discussions are given in Section 3. The paper is concluded in the Section 4.

2. Theoretical Background

Fig. 1 displays the three-layered waveguide sensor. The guiding layer consists of LHM sandwiched between a semi-infinite linear dielectric cladding and a semi-infinite AFM (antiferromagnetic) substrate layer. While the LHM film has both negative permittivity ε_3 and negative permeability μ_3, the linear dielectric cladding has positive permittivity ε_1 and positive permeability μ_1. The AFM substrate has positive permittivity ε_2 and tensor permeability μ_2 defined by Eq. (1).

$$\mu_2(\omega) = \mu_{02}\begin{pmatrix} \mu_{11} & j\mu_{12} & 0 \\ -j\mu_{12} & \mu_{11} & 0 \\ 0 & 0 & \mu_z \end{pmatrix} \tag{1}$$

where,

$$\mu_{11} = 1 + \frac{2\omega_a\omega_m\left(\omega_1^2 - \omega_{02}^2 - \omega^2\right)}{\Delta} \tag{2}$$

$$\mu_{12} = \frac{4\omega_a\omega_m\omega_{02}\omega}{\Delta} \tag{3}$$

$$\Delta = \left[\omega_1^2 - \left(\omega + \omega_{02}\right)^2\right]\left[\omega_1^2 - \left(\omega - \omega_{02}\right)^2\right] \tag{4}$$

$$\omega_1 = \gamma_2\sqrt{H_a\left(H_a + 2H_e\right)} \tag{5}$$

$\omega_{02} = \gamma_2 H_0$, $\omega_a = \gamma_2 M_a$, $\omega_m = 4\pi\gamma_2 M_{s2}$, ω is the circular frequency, H_0 is the external magnetic field that is applied in the z direction and perpendicular to the direction of propagation of the waves, M_{s2} is the unscreened saturation magnetization in the direction of H_0, γ_2 is the absolute value of the gyromagnetic factor in the antiferromagnet, H_a is the internal anisotropy field confined in the x direction, and H_e is the exchange field.

The bulk polaritons for antiferromagnet in an external magnetic have two frequency gaps [23, 24]. The two gaps correspond to the regions of negative value of the Voigt permeability:

$$\mu_v = (\mu_{11}^2 - \mu_{12}^2)/\mu_{11} \tag{6}$$

where, μ_v has two poles at ω^1 and ω^3 and two zeros at ω^2 and ω^4 given by:

$$\omega^{(1,3)2} = \omega_1^2 + \omega_{02}^2 + \omega_m\omega_a \mp \left(4\omega_{02}^2\omega_1^2 + 4\omega_m\omega_a\omega_{02}^2 + \left(\omega_m\omega_a\right)^2\right)^{1/2} \tag{7}$$

$$\omega^{(2,4)} = \mp\omega_{02} + \left(\omega_1^2 + 2\omega_m\omega_a\right)^{1/2} \tag{8}$$

The surface polaritons for the semi-infinite antiferromagnet in the Voigt configuration have two branches for each direction of propagation. The transverse fields TE are assumed to have the oscillation form as follows:

$$\vec{E} = \begin{pmatrix} 0 & 0 & E_z \end{pmatrix} e^{j(\omega t - ky)} \tag{9}$$

$$\vec{H} = \begin{pmatrix} H_x & H_y & 0 \end{pmatrix} e^{j(\omega t - ky)} \tag{10}$$

where, $k = N\omega / c$ is the propagation constant, N is the effective refractive index, and c is the speed of light. Applying Eqs. (9) and (10) to Maxwell's equations and applying boundary conditions at $x = -a/2$ and $x = a/2$, we obtain the dispersion equation as follows:

$$iF_3\left(F_2 - F_1\right)\cot\left(\beta a\right) - \left(F_1F_2 - F_3^2\right) = 0 \tag{11}$$

where, $F_1 = -j\lambda_1$, $F_2 = -j\mu_{02}\,[\mu_{12} - \lambda_2\mu_{11}]$, $F_3 = j\lambda_3$, $\lambda_1 = N/\alpha_1$, $\alpha_1 = (N^2 - n_1^2)^{1/2}$, $n_1 = (\varepsilon_1)^{1/2}$, $\lambda_2 = [N\mu_{11} - \alpha_2\mu_{12}]/[N\mu_{12} - \alpha_2\mu_{11}]$, $\alpha_2 = (N^2 - \varepsilon_2\mu_v)^{1/2}$, $\mu_v = (\mu_{11}^2 - \mu_{12}^2)/\mu_{11}$, $\lambda_3 = N\mu_3/\alpha_3$, $\alpha_3 = (N^2 - \varepsilon_3\mu_3)^{1/2}$, and $\beta = j\alpha_3$.

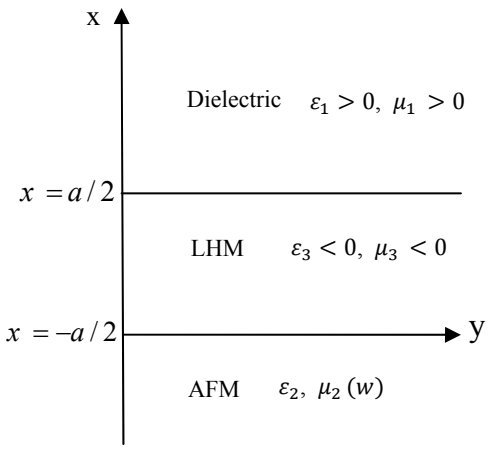


Fig. 1 The proposed three layered waveguide. The film is LHM with $\varepsilon_3 < 0$, $\mu_3 < 0$ surrounded by AFM substrate and dielectric cladding.

The homogenous sensitivity due to guided waves, S, is calculated from the dispersion Eq. (11) by differentiating the effective refractive index N with respect to the cladding refractive $n_1 = \varepsilon_1^{1/2}$. So, S, can be expressed as Eq. (12).

$$S(\omega) = \frac{\partial N}{\partial n_1} \tag{12}$$

The calculation of S is tedious; hence, it is not reproduced here. The values of the refractive index N for surface waves are first numerically calculated form Eq. (11) and accordingly the sensitivities S is calculated numerically from Eq. (12). The behavior of our system will depend on the values of ω^1, ω^3, ω^2, and ω^4. Moreover, it will be affected by the values of MTM's parameters and the thickness of the film.

3. Results and Discussion

In this work, we studied the sensitivity of the sensor. Moreover, we test the effect on the sensitivity for $\mu_v < 0$ and $\mu_v > 0$. In the numerical calculation, we defined the reduced frequencies, $\Omega = \omega/\omega_m$, $\Omega_0 = \omega_{02}/\omega_1$, $\Omega_a = \omega_a/\omega_1$, $\Omega_m = \omega_m/\omega_1$ and wave number, $Q = kc/\omega_m = N\Omega$.

The sensitivity is calculated for both cases when $\mu_v < 0$ and $\mu_v > 0$.

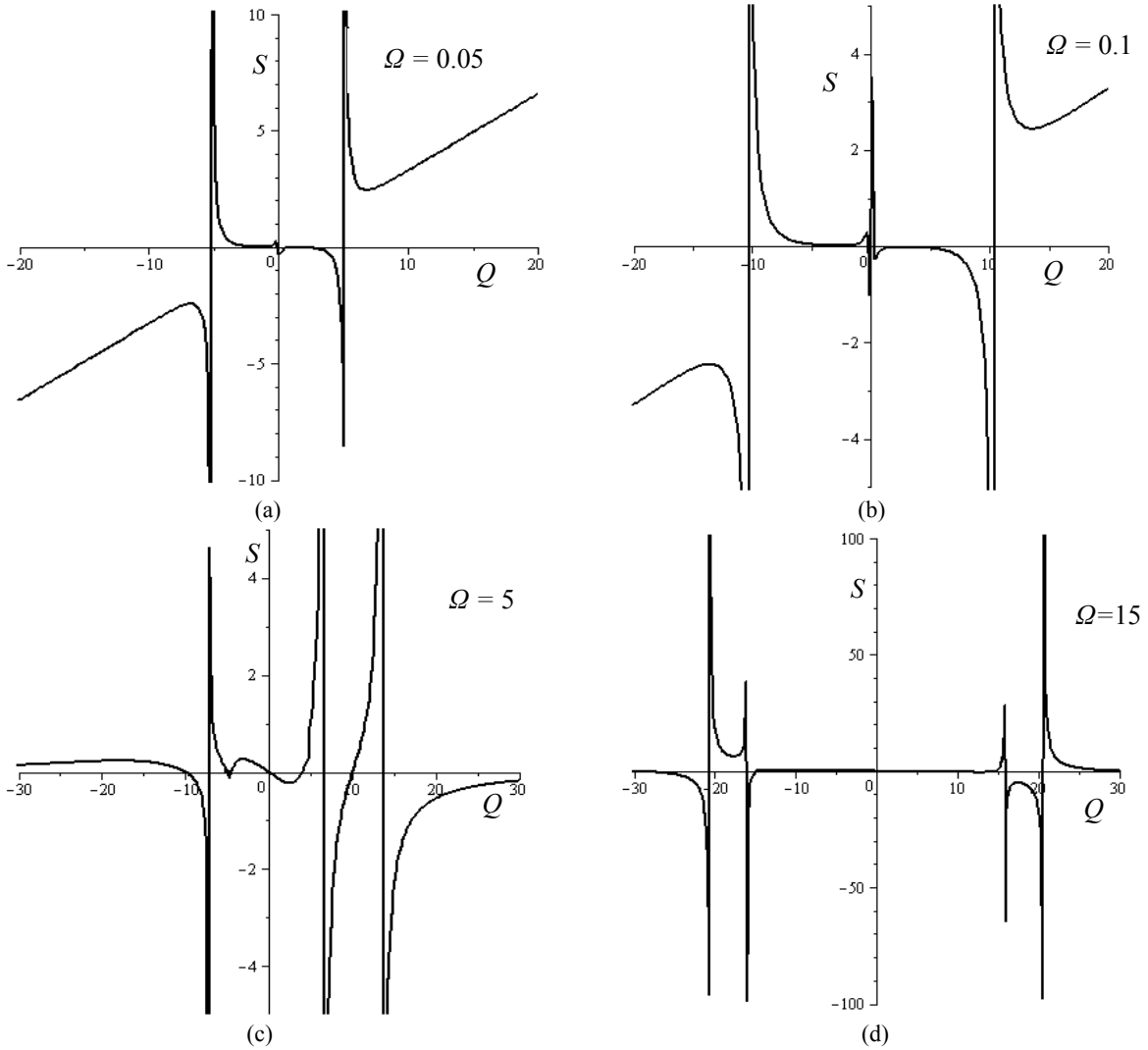


Fig. 2 The sensitivity due to guided waves S is calculated as function of the wave number Q for $\mu_v > 0$ at different values of reduced frequency $\Omega = 0.05$, 0.1, 5 and 15. The film thickness $a = 0.05$ cm.

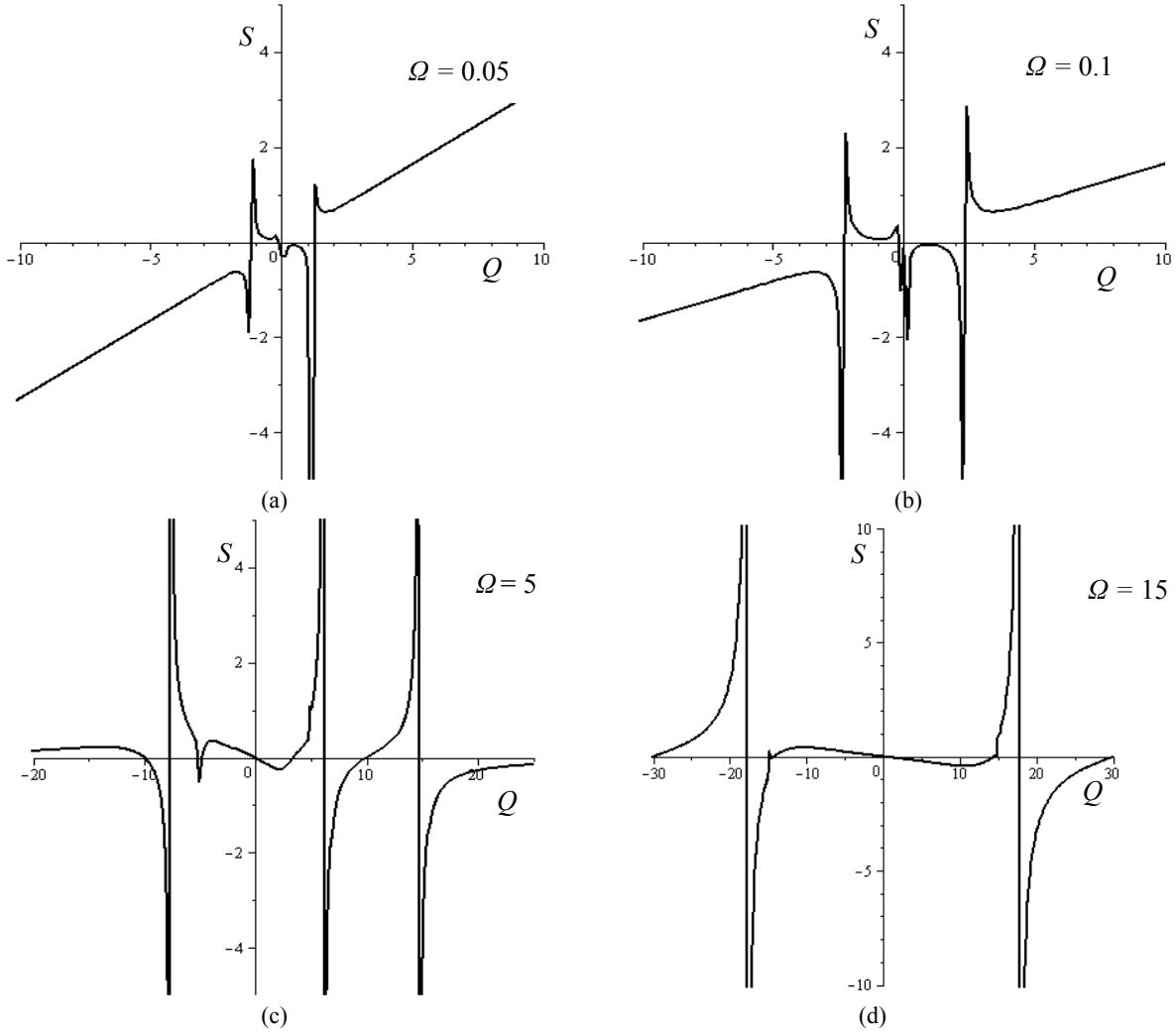


Fig. 3 The sensitivity due to guided waves S is calculated as function of the wave number Q for $\mu_v > 0$ at different values of reduced frequency Ω = 0.05, 0.1, 5 and 15. The film thickness, a = 0.15 cm.

3.1 Results for $\mu_v > 0$

In this case, the reduced frequency is tuned such that $\mu_v > 0$. The sensitivity S is plotted in Fig. 1 as function of wave number Q at the chosen set of values of reduced frequencies Ω = 0.05, 0.1, 5 and 15. The calculation has performed using the following values: a = 0.05 cm, Ω_m = 5, $\Omega_m \cdot \Omega_a$ = 0.1, n_1 = 1, ε_2 = 1.0, ε_3 = -1, μ_3 = -4, Ω_0 = 0.3, μ_{02} = 2.

From Fig. 2, we can see that S varies as the wave number changes. The sensitivity goes to zero at the zeros of wave number Q which corresponds to the zeros of ω and infinities at the poles of ω as stated in Eqs. (7) and (8). The position of the zeros and infinities changes as Ω changes. Fig. 2 gives us a promising sensor for the stated values. The system is very sensitive with changes occurs at the cladding layer. In this case, the maximum value, $S = \pm 7$, occurs at Ω = 0.05 and at $Q = \pm 20$.

To study the effect of the film thickness, the same calculation is repeated keeping all parameters unchanged except the film thickness value is changed to a = 0.15 cm. The sensitivity, S, is plotted in Fig. 3 versus the wave number, Q, at Ω = 0.05, 0.1, 5 and 15.

We notice that the maximum sensitivity, $S = \pm 3$, occurs at Ω = 0.05 at $Q = \pm 3$. The figure exhibits the zeros and poles which is associated with ω. We see the effect of film thickness appears at the limits of the propagation constant, Q, which decreases dramatically

with increasing a. Also, the maximum value of S decreases with respect to the previous calculations.

The effect of changing MTM's parameters are done by repeating the previous calculations keeping all parameters unchanged and swamping the values of ε_3 and μ_3; i.e., ε_3 = -4, μ_3 = -1. Fig. 4 exhibits the sensitivity, S, versus the wave number, Q, at a = 0.05 cm and Ω = 0.05, 0.1, 5 and 15.

The maximum sensitivity S = ±100 occurs at Ω = 0.05 and Q = ±10. From previous calculation, we can control the sensitivity of the sensor by changing the value of the film thickness and the MTM's parameters.

3.2 Results for $\mu_v < 0$

The reduced frequency is tuned such that $\mu_v < 0$. The sensitivity S is displayed in Fig. 5 as function of wave number Q at chosen set values of reduced frequencies Ω = 3.765, 3.7625, 6.8 and 6.95 that satisfied the condition $\mu_v < 0$. The calculation has performed using the following values: a = 0.05 cm, Ω_m = 5, $\Omega_m \cdot \Omega_a$ = 0.1, n_1 = 1, ε_2 = 1.0, ε_3 = -1.0, μ_3 = -4, Ω_0 = 0.3, μ_{02} = 2.

The sensitivity, as presented in Fig. 5, has its maximum value, S = 7, at Ω = 6.7625 and Q = 10.

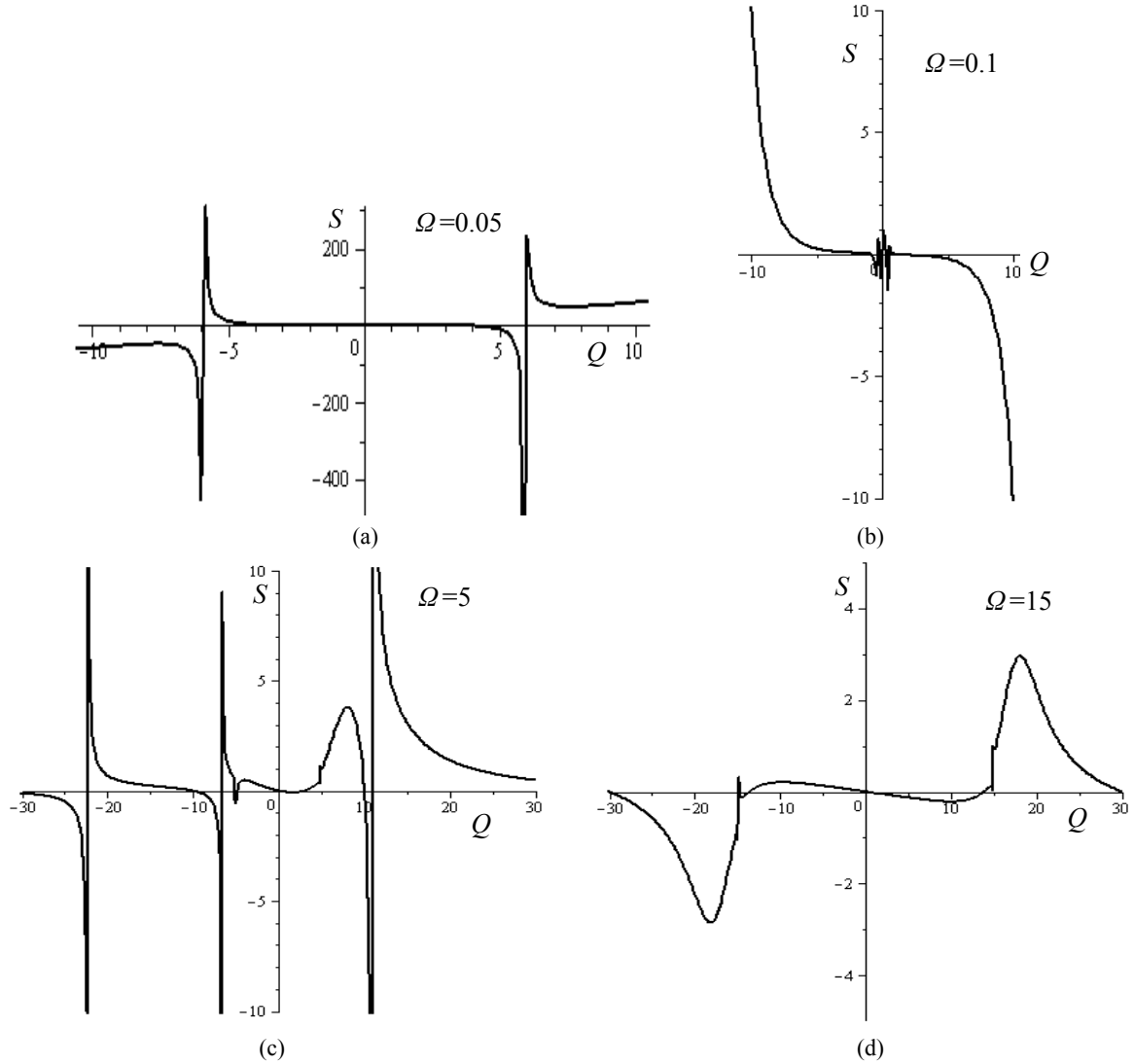


Fig. 4 The sensitivity S is calculated as function of the wave number Q for $\mu_v > 0$ at different values of reduced frequency Ω = 0.05, 0.1, 5 and 15. The film thickness, a = 0.05 cm and ε_3 = -4.0, μ_3 = -1.

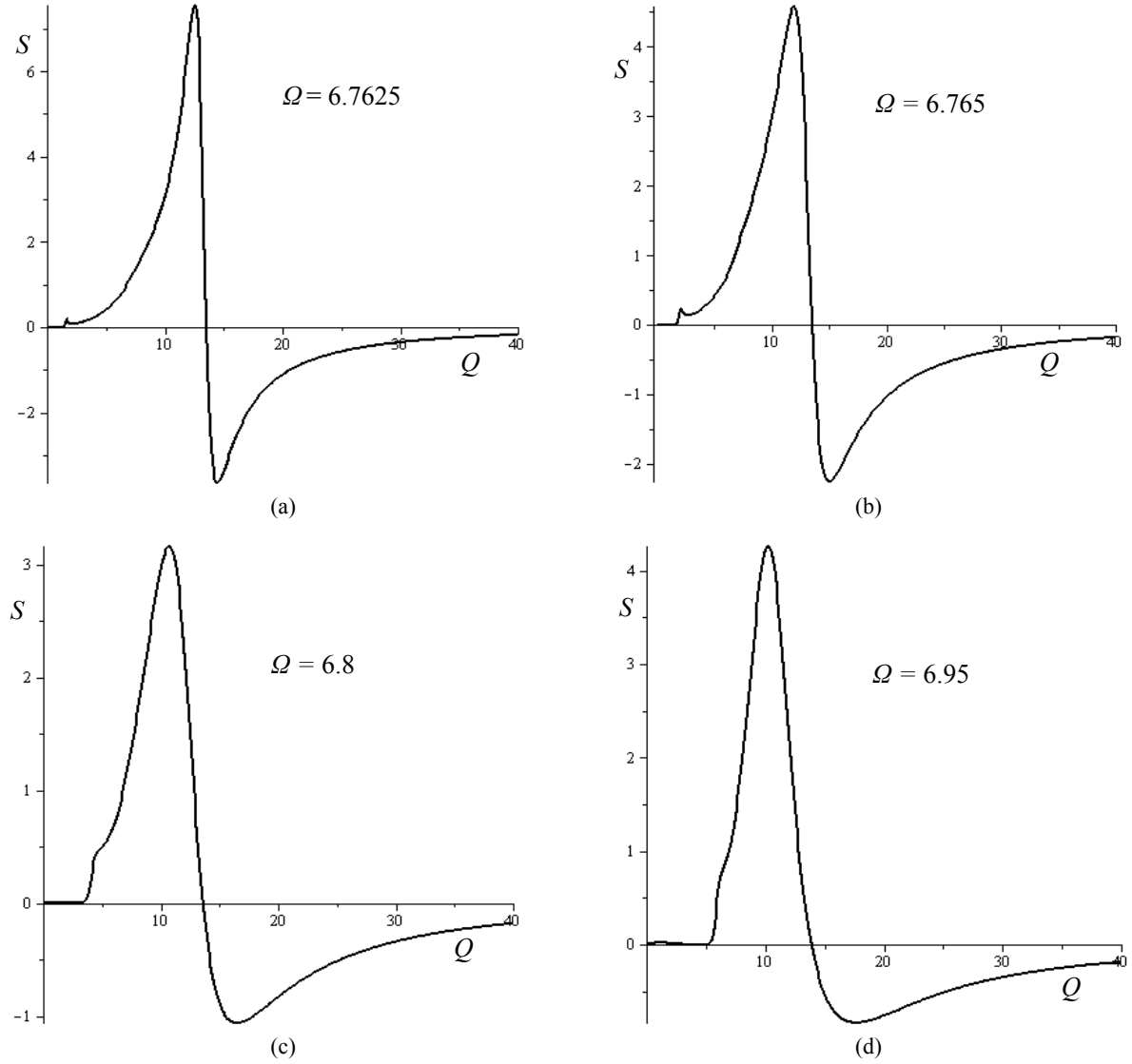


Fig. 5 The sensitivity S is calculated as function of the wave number Q for $\mu_v < 0$ at different values of reduced frequency Ω = 6.7625, 6.765, 6.8 and 6.95.

4. Conclusions

The homogenous sensitivity of the proposed sensor is studied. The sensor is a three-layer waveguide consists of a LHM film surrounded by AF substrate and dielectric cladding. The sensitivity is calculated for range of frequencies at which the Voigt frequency is negative and positive. Moreover, we studied the effect of the film thickness and the LHM parameters. Results show that the sensitivity of the proposed sensor can be tuned by changing the value of the film thickness and the LHM's parameters. The results might be of interest to the sensors fabricators.

References

[1] Ritchie, R. H. Plasma Losses by Fast Electrons in Thin Films. *Phys. Rev*. **1957,** *106,* 874-881.

[2] Schuster, S. C.; Swanson, R. V.; Alex, L. A.; Bourret, R. B.; Simon, M. I. Assembly And Function of a Quaternary Signal Transduction Complex Monitored by Surface Plasmon Resonance. *Nature (London)* **1993,** *365,* 343-347.

[3] Gong, J.; Chu, Q. In *A Novel SCLH Transmission Line Structure and Its Application to UWB Filter Design*, Proceedings of International Workshop on Metamaterials, South China Univ. of Technol., 2008.

[4] He, Y.; He, P.; Harris, V. G.; Vittoria, C. Role of Ferrites in Negative Index Metamaterials. *IEEE Trans. Magnetized* **2006,** *42,* 2852-2854.

[5] Wu, R. X. Effective Negative Refraction Index in Periodic Metal-Ferrite-Metal Film Composite**.** *Journal of Applied Phys.* **2005,** *97,* 076105-076108.

[6] Rachford, F. J.; Armstead, D. N.; Harris, V. G.; Vittoria, C. Simulations of Ferrite-Dielectric-Wire Composite Negative Index Materials. *Phys. Rev. Lett*. **2007,** *99,* 057202-057206.

[7] Thibaudeau, C.; Caillé, A. Interface and Guided Magnetic Polariton Modes in Magnetic Structure. *Phys. Rev. B* **1985,** *32,* 5907-5917.

[8] El-Khozondar, H. J.; Al-Sahhar, Z. I.; Shabat, M. M. Electromagnetic Surface Waves of a Ferrite Slab Bounded by Metamaterials. *International Journal of Electronics and Communications (AEU)* **2010,** *64,* 1063-1067.

[9] Al-Sahhar, Z. I.; Shabat, M. M.; El-Khozondar, H. J. Magnetostatic Surface Waves Propagation at Dissipative Ferrite-MTMs-Metal Structure. *Journal of Superconductivity and Novel Magnetism* **2013,** *2,* 584-594.

[10] El-Khozondar, R.; El-Khozondar, H.; Shabat, M. Surface Wave Propagation in Ferroelectric/MTMS Interface. *Integr. Ferroelectr.* **2011,** *130,* 50-57.

[11] Veselago, V. G. The Electrodynamics of Substances with Simultaneously Negative Values of Permittivity and Permeability. *Soviet Phys. Uspekhi*. **1968,** *10,* 509-514.

[12] Pendry, J. B.; Holden, A. J.; Robbins, D. J.; Stewart, W. J. Magnetism from Conductors and Enhanced Nonlinear Phenomena. *IEEE Trans. Microwave Theory Tech*. **1999,** *47,* 2057-2084.

[13] Pendry, J. B.; Holden, A. J.; Stewart, W. J.; Youngs, I. Extremely Low Frequency Plasmons in Metallic Mesostructures. *Physical Review Letter* **1996,** *76,* 4773-4776.

[14] Shelby, R. A.; Smith, D. R.; Schultz, S. Experimental Verification of Negative Index of Refraction. *Science* **2001,** *292,* 77-79.

[15] Pendry, J. B. Negative Refraction Makes a Perfect Lens. *Physical Review Letter* **2000,** *85,* 3966-3969.

[16] Fang, N.; Lee, H.; Sun, C.; Zhang, X. Sub-Diffraction-Limited Optical Imaging with a Silver Superlens. *Science* **2005,** *308,* 534-537.

[17] Taya, S. A.; El-Khozondar, H. J.; Shabat, M. M.; Mehjez, E. M. TM Nonlinear Waveguide Slab Optical Sensor Utilizing Left-Handed Materials. *Journal of Functional Materials* **2011,** *18,* 1-5.

[18] El-Khozondar, H. J.; Taya, S. A.; Shabat, M. M.; Mehjez, E. M. Lossy Double Negative Guiding Layer Optical Sensors. *Opto-Electronics Review* **2011,** *19,* 277-281.

[19] El-Khozondar, H.; Müller, M.; El-Khozondar, R.; Shabat, M.; Koch, A. In *Temperature Sensitivity of TE Double-Negative Metamaterial Optical Sensor*, Proceedings of Poc. of SPIE 7390, 2009.

[20] El-Khozondar, R. J.; El-Khozondar, H. J.; Shabat, M. M. Double-Negative Metamaterial Optical Waveguide Behavior Subjected to Stress. *Islamic University Journal* **2008,** *16,* 9-20.

[21] El-Khozondar, H. J.; El-Khozondar, R. J.; Shabat, M. M.; Koch, A. W. In *Metallic Nonlinear Magnetooptical Nonreciprocal Isolator,* Proceedings of SPIE Europe-Optical Metrology 2009 International Symposium, Germany, June 15-18, 2009.

[22] Brioude V.; Parriaux, O. Normalised Analysis for the Design of Evanescent-Wave Sensors and Its Use for Tolerance Evaluation. *Optical and Quantum Electronics* **2000,** *32,* 899-908.

[23] Tiefenthaler, K.; Lukosz, W. Sensitivity of Grating Couplers as Integrated-Optical Chemical Sensors. *J. Opt. Soc. Amer. B*. **1989,** *6,* 209-220.

[24] Hartstein, A.; Burstein, E.; Marasusin, A. A.; Brewer, B.; Wallis, R. F. Surface Polaritons on Semi-infinite Gyromagnetic Media. *J. Phys. C*. **1973,** *6,* 1266-1276.

J. Chem. Chem. Eng. 8 (2014) 428-432

Search for New Three-, Four-Component Petasis, Passerini, Hantzsch, Kabachnic-Fields, Ugi Reactions with Organic Compounds of Phosphorus, Arsenic, Antimony and Bismuth

Aibassov Erkin Zhakenovich*, Yemelyanova Valentina Stepanovna, Shakieva Tatyana Vladimirovna, Tussupbaev Nessipbay Kuandykovich and Blagikh Evgeniy Vladimirovich

Research Institute of New Chemical Technologies and Materials, Kazakh National University Al-Farabi, Almaty 005012, Kazakhstan

Received: November 29, 2013 / Accepted: December 18, 2013 / Published: April 25, 2014.

Abstract: It is discovered a new three-, four-component Petasis, Passerini, Hantzsch, Kabachnic-Fields, Ugi reactions with of arsine, stibine and bismuthine in organometallic chemistry. Modifications were replaced to a nitrogen atom of classical reactions of atoms of phosphorus, arsenic, antimony and bismuth. It has been proposed a new mechanism for possible reactions.

Key words: Petasis, Passerini, Hantzsch, Kabachnic-Fields, Ugi reactions, phosphorus, arsenic, antimony, bismuth.

1. Introduction

In recent years, it has been actively investigated nucleophilic reaction organilgalogenidami phosphine and with electrophilic geterilalkenami allowing to obtain primary, secondary and tertiary phosphines, selectively and with high yield. Most of these reactions are realized under mild conditions at a pressure atmlosfernom phosphine.

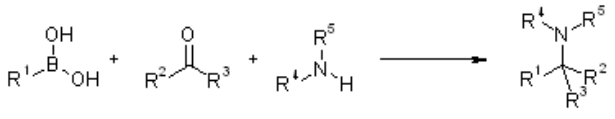
Although the chemistry of organophosphorus compounds devoted a considerable number of monographs, but the reaction of organic compounds of arsenic, antimony and bismuth are very limited. The aim of this work searches for new three-, four-component reactions Petasis, Passerini, Hantzsch, Kabachnic-Fields, Ugi reactions with organic compounds of phosphorus, arsenic, antimony and bismuth.

The purpose of this work, search for new three-, four-component reactions Petasis, Passerini, Hantzsch, Kabachnic-Fields, Ugi reactions with organic compounds of phosphorus, arsenic, antimony and bismuth.

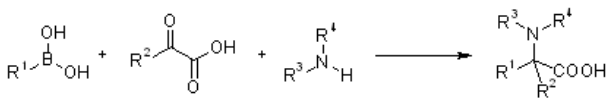
*Corresponding author: Aibassov Erkin Zhakenovich, Professor, research fields: metallorganic chemistry of arsenic, antimony and bismuth. E-mail: erkin53@mail.ru.

2. Theory

It is known that the Petasis reaction is a MCR (multi component reaction) that enables the preparation of amines and their derivatives such as α-amino acids.



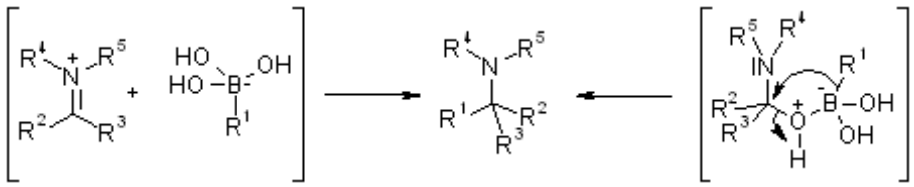
(1)



(2)

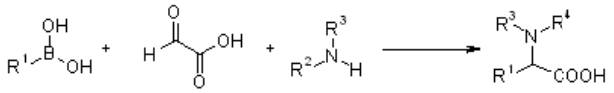
The reaction is also referred to as the Boronic Acid Mannich reaction, since it proceeds via an imine with the organic ligand of the boronic acid acting as the nucleophile, similar to the role of the enolizable

ketone component in the original Mannich reaction. One proposal is that the transfer is actually intramolecular, and takes place via the adduct pictured below:



(3)

The direct reaction with glyoxylic acid merits particular mention, since it leads to interesting, unnatural α-amino acids in a single step, while avoiding the appearance of toxic byproducts such as seen with the Strecker Synthesis.

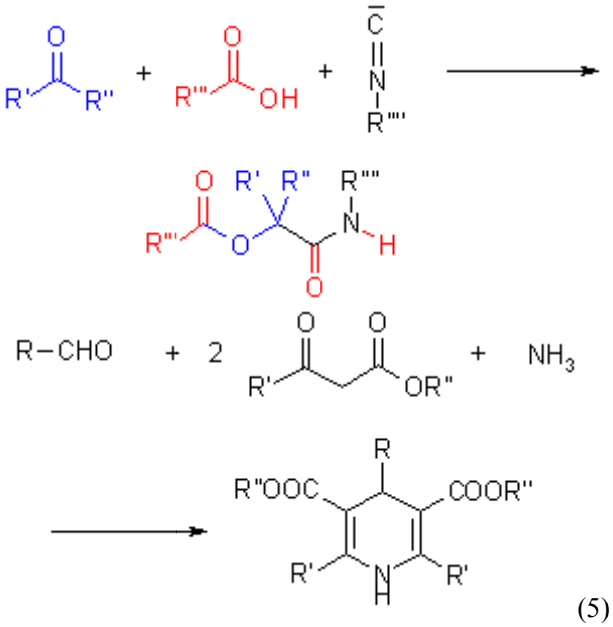


(4)

This reaction can be carried out with secondary amines, sterically hindered primary amines, hydrazines or anilines in dichloromethane at room temperature. The range of potential nucleophilic partners includes alkenylboronic acids, and electroneutral as well as electron-rich (hetero-)arylboronic acids. The conversion of electron-poor boronic acids can be effected at elevated temperatures MW (microwave) in suitable solvents.

It is known that Passerini reaction three-component between a carboxylic acid, a carbonyl compound such as a ketone or aldehyde, and an isocyanide, offers direct access to α-hydroxy carboxamides. The Passerini reaction proceeds rapidly if the reaction is performed in aprotic solvents at room temperature. High yields are obtained with high concentrations of the starting materials in the reaction mixture. From these findings, it is assumed that the Passerini reaction does not follow an ionic pathway. Hydrogen bonding is believed to play a crucial role in the formation of the presumed cyclic transition state for this reaction.

It is known that Hantzsch Dihydropyridine (Pyridine) Synthesis allows the preparation of dihydropyridine derivatives by condensation of an aldehyde with two equivalents of a β-ketoester in the presence of ammonia. Subsequent oxidation (or dehydrogenation) gives pyridine-3,5-dicarboxylates, which may also be decarboxylated to yield the corresponding pyridines.

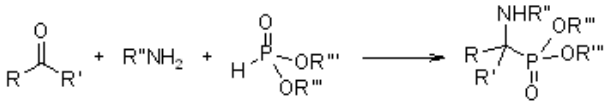


(5)

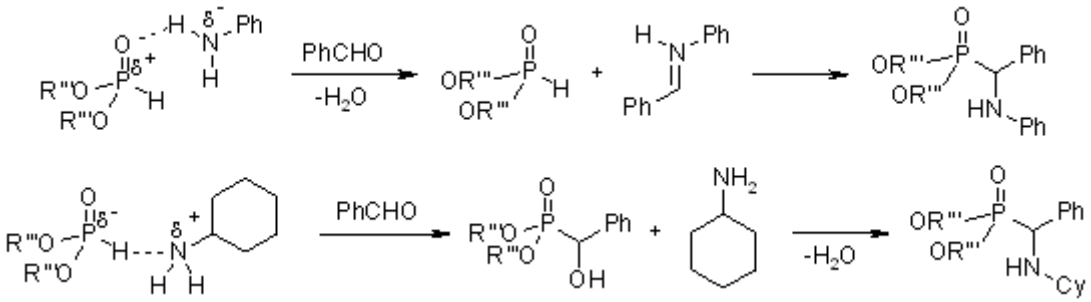
This reaction allows the preparation of dihydropyridine derivatives by condensation of an aldehyde with two equivalents of a β-ketoester in the presence of ammonia. Subsequent oxidation (or dehydrogenation) gives pyridine-3,5-dicarboxylates, which may also be decarboxylated to yield the corresponding pyridines.

It is known that Kabachnik-Fields reaction three-component coupling of a carbonyl, an amine and a hydrophosphoryl compound leads to α-aminophosphonates. The Kabachnik-Fields reaction is very important in drug discovery research for generating peptidomimetic compounds.

The pathway of the Kabachnik-Fields reaction depends on the nature of the substrates. The amine and hydrophosphoryl compound form a complex in which either one of the partners may react with the carbonyl compound. Often, the basicity of the amine determines the reaction pathway. Weakly basic amines such as anilines, which can act as proton donors, favour the formation of an imine, whereas alkylamines such as cyclohexylamines do not form imines.

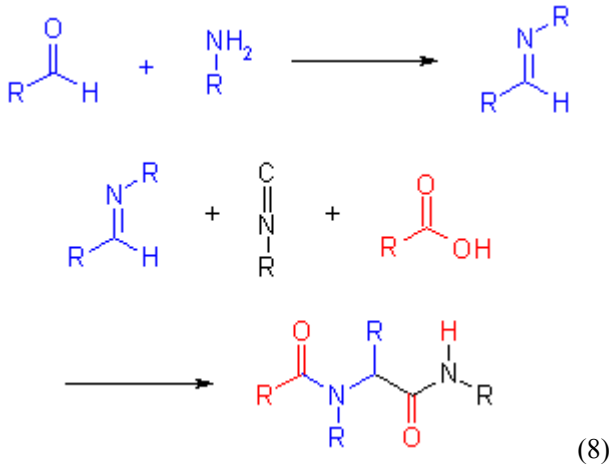


(6)



(7)

It is known that the U-4CC (Ugi four-component condensation) between an aldehyde, an amine, a carboxylic acid and an isocyanide allows the rapid preparation of α-aminoacyl amide derivatives. The Ugi reaction products can exemplify a wide variety of substitution patterns, and constitute peptidomimetics that have potential pharmaceutical applications. This reaction is thus very important for generating compound libraries for screening purposes.



(8)

The mechanism is believed to involve a prior formation of an imine by condensation of the amine with the aldehyde, followed by addition of the carboxylic acid oxygen and the imino carbon across the isocyanide carbon; the resulting acylated isoamide rearranges by acyl transfer to generate the final product.

A distinctive feature of the Ugi reaction is the possibility of introducing a condensation at the same time four or more components under very mild conditions, and ease of implementation and high yields of the reaction products.

A special activity izonitrils linked due to the presence of divalent carbon atom adjacent to the nitrogen lone pair of electrons carrying the imparting of nucleophilic carbene carbon character.

3. Results and Discussion

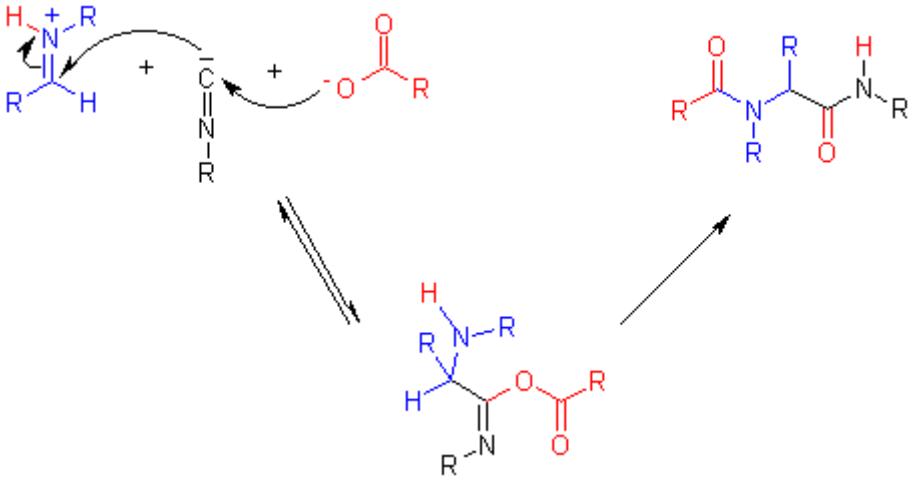
Comparison of the three-, four-component Petasis, Passerini, Hantzsch, Kabachnic-Fields, Ugi reactions with organic compounds of arsenic, antimony and bismuth showed that they all substitution reactions of amines with a variety of organic compounds which have a labile hydrogen atom.

We proposed a general view of the proposed new three-, four-component Petasis, Passerini, Hantzsch, Kabachnic-Fields, Ugi reactions by replacing nitrogen atoms arsenic, antimony and bismuth.

We propose to extend and modify Petasisa substitution reaction with amines on the nitrogen atom of phosphorus, arsenic, antimony and bismuth.

R^1-E$(OR)_2$ + R^2-C(=O)-R^3 + R^4EHR^5 → R1R^2R^3C -ER^4R^5

R^1-E$(OR)_2$ + R^2-C(=O)-COOH + R^3EHR^4 → R^1R^2C(COOH)-ER^3R^4



(9)

where, E = N, P, As, Sb, Bi; R^1, R^2, R^3, R^4, R^5 = H, CH_3, Ar.

We propose modified Hantzsch condensation reaction of aldehyde with two equivalents of a β-ketoester in the presence of ammonia, phosphine, arsine, stibine, and bismuthine. After oxidation (or dehydrogenation) gave pyridin-3,5-dicarboxylic acid, which can be decarboxylated to give the corresponding pyridine, phosphoridine, arsinidine, stibinidine and vismutinidine.

We propose to expand and change Kabachnik-Fields reactions in connection with the replacement of amines on the phosphines, arsines, stibines and vismutines.

R-CO-R^1 + $R^2E_1H_2$ + H-E_2(=O)$(OR^3)_2$ → RR^1C(EHR^3)-E(=O)$(OR^3)_2$

where, E_1, E_2 = N, P, As, Sb, Bi; R, R^1, R^2, R^3 = Alk, Ar.

We propose to expand the Ugi reaction and receive bimetallic organic compounds of arsenic, antimony and bismuth:

REH_2 + R^1R^2C=O + E^2HC=X + $HOCOR^4$ → R-C(=O)-E^2(R)-CH(R)-C(=O)-EHR.

where, X = O, S, Se; E = P, As, Sb, Bi; R^1, R^2, R^3, R^4 = Alk, Ar.

Thus, we first proposed to extend and modify the new three-, four-component Petasis, Passerini, Hantzsch, Kabachnic-Fields Ugi reactions with arsine, stibine and bismuthine in organometallic chemistry. We proposed a new mechanism for the possible reactions.

4. Conclusions

The data presented in this paper show that the organic compound of arsenic, antimony and bismuth are convenient starting materials for the formation of the C-As, C-Sb, C-Bi in obtaining various organometallic compounds which are more widely used as catalysts, pharmaceuticals preparations.

We have opened a new three-, four-component Petasis, Passerini, Hantzsch, Kabachnic-Fields, Ugi reactions with organic compounds of phosphorus, arsine, stibine and bismuthine in organometallic chemistry. We proposed a new mechanism for the possible reactions.

Acknowledgments

The authors would like to thank Ruben M. Savizky (Columbia University, New York) and Chistopher L. Cahill (George Washington University) for discussion of the results.

References

[1] Passerini, M. *Gazz. Chim. Ital.* **1921,** *51,* 126; C. A., **1922,**

16, 555-556.

[2] Baker, R. H.; Linn, L. E. *J. Am. Chem. Soc.* **1948,** *70,* 3721.

[3] Baker, R. H.; Stanonis, D. *J. Am. Chem. Soc.* **1951,** *73,* 699.

[4] Ugi, I.; Offermann, K. *Chem. Ber.* **1964,** *97,* 2276-2996.

[5] Hagedorn, I.; Eholzer, U. *Chem. Ber.* **1965,** *98,* 936.

[6] Ugi, I. *Angew. Chem.* **1962,** *70,* 9.

[7] Sjoberg, K. *Svensk. Kem. Tidskr.* **1963,** *75(10),* 493.

[8] Neidlein, R. *Angew. Chem.* **1964,** *76(11),* 500.

[9] Kabachnik, M. I. *Advances of Chemistry* **1974,** *43(9),* 1554-74.

[10] Nifantev, E. E. *Chemistry Hidrophosphorils Compounds;* Moscow, 1983; pp 55-59.



Journal of Chemistry and Chemical Engineering
Volume 8, Number 4, April 2014

David Publishing Company
240 Nagle Avenue #15C, New York, NY 10034, USA
Tel: 1-323-984-7526, 323-410-1082; Fax: 1-323-984-7374, 323-908-0457
http://www.davidpublishing.com, www.davidpublishing.org
chemistry@davidpublishing.com, chemistry@davidpublishing.org

ISSN 1934-7375